Computational Study on Red Blood Cells in Shear Flow : from Single Cellular Mechanics to Semi-dilute Suspension Properties

東北大学大学院医工学研究科

博士論文

博士(医工学)

Computational Study on Red Blood Cells in Shear Flow:
from Single Cellular Mechanics to Semi-dilute Suspension Properties

せん断流れ場における赤血球の計算力学的研究:
単一細胞力学から準希薄懸濁液特性まで

大森俊宏

2012 年 1 月 19 日

Computational study on red blood cells in shear flow: from single cellular mechanics to semi-dilute suspension properties

Toshihiro OMORI

Abstract

Blood is a specialized bodily fluid flowing through blood vessels. The main function of blood is to transport many materials in plasma, such as blood cells, oxygen, glucose, amino acids, etc., and to maintain the physiological homeostasis of our body. To understand the transport phenomena in blood flow, we must clarify detailed flow field as well as distribution of blood cells in the flow. Since, the main component of blood cells is a red blood cell (RBC), flow field is strongly dependent on the microscopic RBC behaviour, which are affected by the membrane tension of deformed RBCs and hydrodynamic interactions between RBCs.

In former studies, the hemodynamics has been investigated in macroscopic and microscopic regimes, separately. However, the vascular system is continuously ranged from micro- to centi-meter scale in the body, and the body system is maintained by the multi-scale cardiovascular system. For consecutive understanding of physiology and pathology of blood flow, it is now desirable for a mechanical model which can be applied to arbitrary scale physics of blood flow. To overcome the multi-scale problems of blood flow, we need to develop a macroscopic continuum model of an RBC suspension from the cellular mechanics of individual RBCs.

In a flowing suspension, RBCs hydrodynamically interact with other cells and the cell-cell interactions induce the mixing of RBCs in the suspension. Such a flow-induced mixing may be described by the self-diffusivity of RBCs. This phenomenon

was discussed experimentally in a few studies, but it has not been clarified quantitatively. Thus, the diffusivity of RBCs subjected to fluid flow must be clarified in order to develop a macroscopic continuum model of a suspension of RBCs. Not only the diffusion of RBCs but the stress system of a suspension, i.e. particle stress tensor, is also important to describe the momentum transport in the RBC suspension, because it determines the bulk flow field. Although the apparent viscosity or velocity field has been mainly discussed in former studies, the particle stress tensor of an RBC suspension has not been clarified yet. The particle stress tensor can be described by the stresslet of individual RBCs, which is determined by the membrane tension of RBCs. We, therefore, need to clarify the rigorous membrane tension of individual RBCs subjected to fluid flow to construct a detailed stress system of an RBC suspension.

The objective of this study is to investigate the cellular mechanics of an RBC in shear flow and to clarify a suspension properties of RBCs from dilute to semi-dilute regimes. In this thesis, we first discuss the mechanical modeling of the RBC membrane, because it is very important in analyzing the membrane tension. We look for an adequate mechanical membrane model to express a large deformation of an RBC in fluid flow by comparing with continuum hyper-elastic models and discrete spring network models. We then investigate single RBC motions in shear flow. The results are applied to discussions of the membrane tension and rheology of a dilute suspension of RBCs. Finally, we investigate the pairwise interaction of RBCs in shear flow. We track a trajectory of a single marked RBC, and the trajectory is used to determine the self-diffusivity of RBCs in the semi-dilute regime. We also investigate the membrane tension and rheological properties of a suspension of RBCs in the semi-dilute regime.

In chapter 1, we explain the research background and the purpose of this study.

In chapter 2, the governing equations of RBCs deforming under viscous flow are presented. An RBC has no nucleus, and characteristics of large deformation are determined by both the fluid mechanics of internal and external fluids and the solid mechanics of the membrane. In this study, an RBC is modeled as a capsule with a hyper-elastic membrane. Due to the small size of RBCs, we assume that the flow is Stokesian, which is described by boundary integral representations. For mathematical descriptions of the membrane mechanics, we use the shell theory of the large elastic deformation.

In chapter 3, we describe the numerical methods for the capsule dynamics in viscous flow. For the membrane mechanics of a capsule, a finite element method is used. To solve the boundary integral equation of the flow field, a boundary element method is employed. For validations of the numerical scheme of the finite element-boundary element (FE-BE) coupling method, we investigate the membrane load and capsule deformation under inflation and shear flow conditions. The results are compared with former analytical and numerical studies and we confirmed the accuracy. To accelerate computation speed, GPGPU is applied to the FE-BE coupling method using CUDA. We succeeded about 230 times acceleration of the computation speed comparing with a CPU computation.

In this study, we model the RBC membrane by a continuum hyper-elastic material. However, some of former studies use a spring network model to solve a large deformation of the RBC membrane. In chapter 4, we compare the mechanical properties of a membrane modeled with continuum constitutive laws and a discrete spring network to clarify the correlations between the mechanical properties of discrete spring network model and continuum constitutive laws and to discuss an adequate model for the RBC membrane. We compare uniaxial and isotropic deformations of a two-dimensional sheet, both analytically and numerically. The 2D sheet is discretized

with four kinds of mesh to analyze the effect of the spring network configuration. We derive the relationships between the spring constant and continuum properties, such as the Young modulus, Poisson ratio, area dilation modulus and shear modulus. It is found that the mechanical properties of spring networks are strongly dependent on the mesh configuration. Comparing the results between the different membrane models, we find that it is hard to express the area incompressibility observed in biological membranes using a simple spring network model. It is therefore desirable to use a continuum model of Skalak et al. (1972) for the RBC membrane to express the area incompressible property.

In chapter 5, we investigate the dynamics of a single RBC in creeping shear flow and the rheological properties in the dilute limit. When an RBC is subjected to an external flow, hydrodynamic forces on its membrane lead to motion and deformation. Although dynamics of a rigid non-spherical particle is well understood by Jeffery's theory (1922), that of an RBC remains unclear. In this chapter, we first investigate the kinematic motion of an RBC in creeping shear flow. The results show that the orientation of an RBC is variant under time-reversal, though that of a rigid particle is invariant. Surprisingly, the steady alignment of an RBC over long time duration shows transition depending on the shear rate. The transition cannot be explained by the minimum energy dissipation of the system but full fluid and solid mechanics are needed to understand of them.

Flow-induced deformation of RBCs affects the cell ability to release various molecules and regulate their concentration in blood. The resulting elastic tensions in the membrane play a key role in mechano-transduction and govern its rupture in case of hemolysis. We next analyze the elastic membrane tension of an RBC under shear flow condition. In high capillary number regime, distributions of the principal tensions change periodically and the maximum tensions appear on the side of the

deformed RBC, whereas the high isotropic tension only appears at the top/bottom of the deformed RBC. Due to the strain-hardening property of the membrane, the deformation is suppressed in high capillary number regime but the membrane tension increases monotonically with the capillary number. These findings on the membrane tension would be useful to clarify not only the membrane rupture but also the mechano-transduction of RBCs.

We finally discuss the rheological properties of a dilute suspension of RBCs in shear flow. When a suspension is so dilute that the motion of an RBC is independent of the other cells, the particle stress tensor can be determined by the stresslet of an RBC subjected to fluid flow. The effective shear viscosity shows shear-thinning properties. Surprisingly, in the dilute regime, it becomes smaller as the viscosity ratio of the internal to external liquids is increased. The diagonal components of the stresslet are no longer isotropic. The first normal stress difference becomes positive, whereas the second normal stress difference becomes negative. The ratio between the normal stress difference and shear stress of the suspension monotonically increases with capillary number, because the apparent viscosity of the suspension decreases with applied shear rate. These findings about the dilute suspension rheology form a fundamental basis for the knowledge of complicated suspension mechanics of capsules and biological cells.

In chapter 6, we investigate the hydrodynamic interaction between two RBCs in shear flow and the results are applied to discussion of the shear-induced self-diffusion of the RBCs, as well as the stresslet of the RBCs during the interaction. The pairwise interaction is an important phenomenon. The particle stress tensor can be expanded in terms of ϕ, where ϕ is the volume fraction and the pairwise interactions give ϕ^2 term. Thus, ϕ^3 term becomes one order of magnitude smaller when ϕ is about 10%. The pairwise interaction is also important for diffusion of RBCs, because cell-

cell interaction is the main mechanism for an RBC to deviate from the background streamline.

To investigate the shear-induced self-diffusivity of RBCs, we analyze the trajectories of a single marked RBC during the cell-cell interaction. Due to the deformability of the RBC membrane, the trajectories become asymmetric and the displacements are observed in the cross-flow direction. We observe that the trajectories are strongly affected by the viscosity ratio but slightly by the capillary number. Shear-induced self-diffusion coefficients of RBCs are then calculated by a combination of analytical and numerical integration of the cross-flow displacements. The self-diffusion of RBCs has a peak value when capillary number is about 1, and monotonically decreases with the viscosity ratio. These tendencies are similar to those of drops but the values are quantitatively different. The interface of drops has no elasticity, thus the elasticity of RBC membrane likely causes quantitative difference of shear-induced diffusivity between drops and RBCs.

Finally, we discuss the stresslet of the RBCs during the pairwise interaction and its impact on the particle stress tensor of the suspension. The additional shear viscosity comes from the cell-cell interaction is positive in all cases, thus the effective shear viscosity of the suspension increases quadratically. The first normal stress difference becomes negative in the case of the identical viscosity, whereas it is positive when the viscosity ratio is larger than 1. Thus the bulk first normal stress difference of the suspension is increased by the hydrodynamic interaction of RBCs when the viscosity ratio is large.

Consequently, we succeed to develop a macroscopic continuum model of an RBC suspension in both dilute and semi-dilute regimes. The findings presented in this thesis can be utilized for a fundamental basis for the breakthrough in the multi-scale problems of blood flow. In near future, our numerical methods will be applied to

concentrated regime to develop a continuum model of a dense suspension of RBCs.

Acknowledgements

本学位論文を作成するに当たり，沢山の方々のご協力を頂きました．ここに感謝の意を記したいと思います．

山口隆美先生には，山口研究室に配属した学部３年より，８年間に渡ってご指導頂きました．生体力学という分野に携わる機会を与えて頂き，８年間勉学に励むことができたのは先生の暖かいご指導によるものであると心より感謝しています．８年間大変お世話になりました．

山口有為子さんには，日頃より励ましのお言葉を頂きました．またご自宅での食事会を通じて，暖かいお食事まで頂きました．暖かいご支援，ありがとうございました．

石川拓司先生には，本研究の細部に渡ってご指導頂きました．研究指導のみならず，研究者としての心構えなど沢山のことを学ばせて頂きました．心より感謝しています．

今井陽介先生には，親身になって研究や生活面での相談に乗って頂きました．今井先生のご指導の下，計算力学について沢山学ぶことができました．ありがとうございました．

早瀬敏幸先生には，この度学位論文の審査をお引受けいただき，沢山のご助言を頂きました．ここに感謝の意を記します．

上野裕則先生，沼山恵子先生には学位論文の審査をお引受けいただき沢山のアドバイスを頂きました．特に生物に関する知識は，機械出身の自分には無いものが多数あり有益なものになりました．ここに感謝いたします．

I would like to express my sincere thanks to Prof. Barthès-Biesel and Dr. Salsac and all members in Compiegne for their kind support and advices.

大開さん，岡崎さん，佐藤洋子さん，佐藤千尋さん，藤原さん，米田さん，山口研秘書，21COE，GCOE 事務の方々にはいつも暖かく支えて頂きました．ありがとうござい

ます．

山口研同期の三木貴仁くんには，学部３年より今まで８年間公私に渡って支えてもらいました．配属が決まってから今日までこんなに長い付き合いになるとは思いませんでしたが，心置き無く話せる友人がいたから８年間やってこれたと思います．同期の岸本真迪くん，佐々木俊介くん共々これからもよろしく．

中村匡徳先生を始め，山口研在籍の間沢山の優秀な先輩方と頼もしい後輩たちに支えられ研究に勤しむことができました．全員の名前を記すことは出来ませんが，皆々様には大変感謝しています．

本研究は GCOE「新世紀世界の成長焦点に築くナノ医工学拠点」の推薦のもと，日本学術振興会特別研究員制度の支援により進められました．ここに謝意を記します．

最後に，仙台の地で勉強する機会を与えて頂きこれまで育ててくれた家族，長きに渡って支えてくれた佐藤美玲さんに厚く御礼申し上げます．

2012 年 1 月大森俊宏

Contents

Chapter 1

Introduction

1.1 Blood

Blood is a specialized bodily fluid flowing through blood vessels. The main function of blood is to transport many materials in plasma, such as blood cells, oxygen, glucose, etc. This function is very important to maintain the physiological homeostasis of our body.

Blood is not homogeneous fluid but a dense suspension of blood cells. The main component of blood cells is a red blood cell (RBC), whose volume fraction in whole blood normally reaches 40 to 45%. Macroscopic fluid properties of blood are then strongly dependent on the microscopic RBC behaviour in blood flow.

1.2 Red blood cell

The human RBC has a biconcave shape and a diameter of 8 μm in its healthy state. It repeatedly undergoes large elastic deformation during its passage through small capillaries. An RBC has no nucleus and the membrane plays important role to determine the characteristics of large deformation. The RBC membrane is not a simple homogeneous single-layer material but consisted of lipid bilayer and cytoskeletal structure of protein, such as a spectrin network on the membrane.

To qualitatively and quantitatively investigate the stress-strain relationship of the membrane, many mechanical membrane models have been developed. One of the most common model is a continuum hyper-elastic model [35, 78]. In this model, the complex membrane elements are modeled as a homogeneous continuum material.

Another famous membrane model is a spring network model [36, 64, 66, 84, 85, 90]. In this model, the complex membrane elements are also modeled as a simple spring network.

Recently, multi-scale complex membrane model was proposed [67]. In this complexed model, the whole cell membrane is modeled as two distinct layers of lipid bilayer and cytoskeleton. The cytoskeletal spectrin network is modeled by molecular-based thermally activated constitutive model and the lipid bilayer is modeled as a solid continuum viscoelastic model. The physical quantities obtained from the molecular based cytoskeleton and continuum based lipid bilayer are shared by the complex junction model.

Some researchers focused not only on the whole membrane mechanics but on the cytoskeletal mechanics of the membrane [51, 52, 60]. Suresh and his coworkers [51, 52], for instance, investigated the cytoskeletal mechanics by coarse-grained dissipative particle dynamics method. In their model, they assumed that the RBC spetctrin network always undergoes in remodeling in topological connectivity at a certain rate, because of the mechanical, thermal or chemical driving forces. Each spectrin tetramer was modeled by elastic spring and they are connected by a spherical bead which represents an actin protofilament. Their interaction was modeled by the Lennald-Jones potential, which is a function of the distance between the elements. The association of a spectrin and an actin was breakable, as well as reformable, and the network topology changed dynamically using a coarse grained molecular dynamics simulation.

Each membrane model has specific advantages and disadvantages, respectively. Thus, an adequate mechanical membrane model must be chosen to conduct the objective of each study. The main topic of this study is the macroscopic suspension properties of blood, where the mechanical membrane tension of the RBCs plays important role. To express rigorous membrane tension in a given deformation of the RBC, well-established continuum hyper-elastic model is employed for the membrane. In the continuum based membrane model, the mechanical properties are determined by the constitutive laws, of which the stress-strain relationships are exactly clarified [8]. In mechanical point of view, the most important membrane properties are the area-incompressibility and the response of large elastic deformation. Detailed discus-

sions of mechanical modeling of the membrane are described in chapter 4.

1.3 Rheology of blood

Transport phenomena of blood is very important to maintain our body. To understand of the flow filed of blood flow, rheology of blood has been investigated more than half a century. In classical studies, blood is assumed as a homogeneous fluid in macroscopic regime. Due to the microscopic RBC behaviours, blood showes non-Newtonian effects in macroscopic regime. To model the non-Newtonian properties of blood, some non-Newtonian fluid models were proposed, such as the Casson model and the power-law model, etc.

In microscopic regime, on the other hand, many researchers have investigated individual RBC behaviours or apparent viscosity of the suspension in micro-vessels analytically, experimentally and numerically [1, 4, 29, 30, 33, 72, 74, 95]. For example, Secomb & Skalak [74] analytically investigated capillary flow of an RBC with lubrication theory and they discussed the correlations between the pressure drop and RBC shape in the lumen. Pries et al. [72] experimentally estimated the apparent viscosity of RBC suspension in glass capillaries. They showed that the apparent viscosity becomes the minimum in a certain range of a diameter of the capillary tube due to the existence of cell-free layer near the wall.

To numerically investigate the motion and deformation of RBCs in fluid flow, the discontinuous jump of the fluid stress tensor across the thin membrane must be taken in to account. A boundary element method can treat such a discontinuous stress jump explicitly and it is known that one of the most accurate numerical method to simulate RBCs in fluid flow. Ramanujan & Pozrikidis [73] first conducted 3D simulation of an RBC in shear flow using a boundary element method. The membrane was modeled by a 2D continuum hyper-elastic material. In their model, the computations was unstable due to the compressive stress on the membrane and few results were discussed in the paper. To stabilize the computation, Pozrikidis [69, 70] introduced a continuum based membrane bending rigidity into the model and succeeded to simulate an RBC behaviour in a tube flow. In his bending model, however, the curvature of the membrane was estimated from only its mean value. The curvature of a 2D

membrane should be described by the tensor formulation and more discussions about the bending model should be needed. Recently, multiple RBCs flow in micro-vessels were conducted with a boundary element method [30, 95]. Zhao et al. [95] computed apparent viscosities of cellular flow in capillaries using a spectral boundary element method. They succeeded 27-RBCs flow in the capillary and the results were compared with the Pries's experimental results.

In former studies, rheology of blood has been investigated in macroscopic and microscopic regimes, separately. However, the vascular system is continuously ranged from micro- to centi-meter scale in the body. For consecutive understanding of physiology and several pathology of blood flow, it is now desirable for a mechanical model which can be applied to arbitrary scale physics of blood flow. To overcome the multi-scale problems of blood flow, we need to develop a macroscopic continuum model of the RBC suspension from the cellular mechanics of individual RBCs.

1.4 Objective

To develop a macroscopic continuum model, we must clarify detailed flow field as well as distribution of RBCs in the flow. The microscopic RBC behaviours are affected by hydrodynamic interactions between the RBCs. The hydrodynamic interaction of RBCs enhances the mixing of the RBCs in the suspension. Such a flow-induced mixing may be described by the self-diffusivity of RBCs.

Not only the diffusion of RBCs but the stress system of a suspension is also important to describe the momentum transport in the RBC suspension, because it determines the bulk flow field. To determine the relation between the macroscopic rheological properties of a suspension and small particle behaviour, Batchelor [10] analytically introduced the stress system of a suspension, which is called as a particle stress tensor. Although the apparent viscosity or velocity field has been mainly discussed in former studies, the particle stress tensor of an RBC suspension has not been clarified at all. The particle stress tensor can be described by the stresslet of individual RBCs, which is determined by the membrane tension of RBCs. We, therefore, need to clarify the rigorous membrane tension of individual RBCs subjected to fluid flow to construct a detailed stress system of an RBC suspension.

The objective of this study is to investigate the cellular mechanics of an RBC in shear flow and to clarify a suspension properties of RBCs from dilute to semi-dilute regimes. In this thesis, we first discuss the mechanical modeling of the RBC membrane, because it is most important in analyzing the membrane tension. We look for an adequate mechanical membrane model to express a large deformation of an RBC in fluid flow by comparing with continuum hyper-elastic models and discrete spring network models. We then investigate single RBC motions in shear flow. The results are applied to discussions of the membrane tension and rheology of a dilute suspension of RBCs. Finally, we investigate the pairwise interaction of RBCs in shear flow. We track a trajectory of a single marked RBC and the trajectory is used to determine the self-diffusivity of RBCs in semi-dilute regime. We also investigate the membrane tension and rheological properties of a suspension of RBCs in semi-dilute regime.

Chapter 2

Mechanics of RBCs in liquids

In this chapter, we present the governing equations of red blood cells (RBCs) deforming under viscous flow. An RBC is modeled as a capsule with a hyper-elastic membrane with surface shear elastic modulus G_s and area dilation modulus K_s. Flow of the internal and external liquids are described by the boundary integral equation of the Stokes flow. For mathematical descriptions of the membrane mechanics, we use the shell theory of the large elastic deformation. Throughout this chapter, summation is performed over repeated indies. Greek indices take values 1 or 2, and Latin indices take values 1, 2 or 3.

2.1 Membrane mechanics

RBCs are small liquid capsules enclosed by a biological membrane consists of a lipid bilayer and an underlying protein cytoskeleton [78]. As the membrane is very thin comparing with its size and typical radius of curvature, we can consider only the deformation of its median surface devoid of bending resistance. Furthermore, the stresses can be integrated across the thickness and be replaced by tensions, i.e., forces per unit length of the median deformed surface. From now on, the term 'membrane' refers to the median surface.

2.1.1 Curvilinear coordinates

Consider a material point of the surface of a two-dimensional membrane. We introduce local curvilinear coordinates (ξ^1, ξ^2, ξ^3), as depicted in figure 2.1. The first

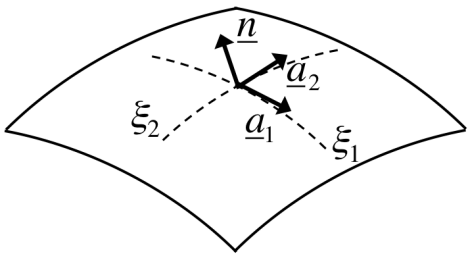

Fig. 2.1 Illustration of a local covariant base $(\underline{a}_1, \underline{a}_2, \underline{n})$ in deformed state of the membrane.

two coordinates ξ^α are tangential to the membrane and ξ^3 is normal to the membrane. In this case, the material point on the membrane is determined by two surface curvilinear coordinates ξ^α.

Let $\underline{x}(\xi^1, \xi^2)$ be a position of the material point in the deformed state. The local covariant bases are defined by

$$\underline{a}_\alpha = \frac{\partial \underline{x}}{\partial \xi^\alpha}, \quad \underline{a}_3 = \underline{n}. \tag{2.1}$$

The first two base vectors $\underline{a}_\alpha$ are tangential to lines of ξ^α. The third base vector $\underline{a}_3$ is the unit normal vectors pointing outward, which is calculated as:

$$\underline{n} = \frac{\underline{a}_1 \times \underline{a}_2}{\|\underline{a}_1 \times \underline{a}_2\|}. \tag{2.2}$$

The associated contravariant bases are defined as $\underline{a}^i \cdot \underline{a}_j = \delta^i_j$. The covariant and contravariant metric tensor are given by

$$a_{ij} = \underline{a}_i \cdot \underline{a}_j, \quad a^{ij} = \underline{a}^i \cdot \underline{a}^j. \tag{2.3}$$

Then, the local contravariant bases can be obtained from

$$a^{ij}\underline{a}_j = \left(\underline{a}^i \cdot \underline{a}^j\right) \cdot \underline{a}_j = \underline{a}^i \cdot \left(\underline{a}^j \cdot \underline{a}_j\right) = \underline{a}^i. \tag{2.4}$$

The local covariant bases can be also rewritten as

$$\underline{a}_i = a_{ij}\underline{a}^j. \tag{2.5}$$

Multiplying equations (2.4) and (2.5), we have

$$\underline{a}^i \cdot \underline{a}_j = a^{ik}\underline{a}_k \cdot a_{jl}\underline{a}^l = a^{ik}a_{jl}\delta^l_k = a^{ik}a_{jk} = \delta^i_j, \tag{2.6}$$

thus,

$$\begin{pmatrix} a^{11} & a^{12} & a^{13} \\ a^{21} & a^{22} & a^{23} \\ a^{31} & a^{32} & a^{33} \end{pmatrix} \begin{pmatrix} a_{11} & a_{12} & a_{13} \\ a_{21} & a_{22} & a_{23} \\ a_{31} & a_{32} & a_{33} \end{pmatrix} = \begin{pmatrix} 1 & 0 & 0 \\ 0 & 1 & 0 \\ 0 & 0 & 1 \end{pmatrix}. \tag{2.7}$$

Hence, the local contravariant metric tensor is given by

$$\begin{pmatrix} a^{11} & a^{12} & a^{13} \\ a^{21} & a^{22} & a^{23} \\ a^{31} & a^{32} & a^{33} \end{pmatrix} = \begin{pmatrix} a_{11} & a_{12} & a_{13} \\ a_{21} & a_{22} & a_{23} \\ a_{31} & a_{32} & a_{33} \end{pmatrix}^{-1}. \tag{2.8}$$

From equations (2.2) and (2.3), equation (2.8) is reduced to

$$\begin{pmatrix} a^{11} & a^{12} & 0 \\ a^{21} & a^{22} & 0 \\ 0 & 0 & 1 \end{pmatrix} = \begin{pmatrix} a_{11} & a_{12} & 0 \\ a_{21} & a_{22} & 0 \\ 0 & 0 & 1 \end{pmatrix}^{-1}, \tag{2.9}$$

and we have

$$a^{11} = \frac{a_{22}}{|a_{\alpha\beta}|}, \quad a^{22} = \frac{a_{11}}{|a_{\alpha\beta}|}, \quad a^{12} = a^{21} = -\frac{a_{12}}{|a_{\alpha\beta}|}, \tag{2.10}$$

where $|a_{\alpha\beta}| = a_{11}a_{22} - a_{12}^2$.

2.1.2 Membrane deformation

We now consider deformation of the 2D membrane. Assuming negligible bending stiffness, deformation occurs only in the plane of the membrane. Let $\underline{dX}$ and $\underline{dx}$ be the infinitesimal vector in the reference state and deformed state, respectively. Based on the Kirchhoff-Lave theory, a material vector normal to the surface remains normal to the surface after deformation. Then, surface deformation gradient tensor $\underline{\underline{F_s}}$ is defined by

$$\underline{dx} = \underline{\underline{F_s}} \cdot \underline{dX}, \tag{2.11}$$

and is given by

$$\underline{\underline{F_s}} = \underline{a}_\alpha \otimes \underline{A}^\alpha, \tag{2.12}$$

where $\underline{A}^{\alpha}$ are the local contravariant bases in the reference state. The local deformation of the surface can be measured by the right Cauchy-Green tensor

$$\begin{aligned}\underline{\underline{C}} &= \underline{\underline{F_s}}^T \cdot \underline{\underline{F_s}} \\ &= (\underline{A}^{\alpha} \otimes \underline{a}_{\alpha}) \cdot \left(\underline{a}_{\beta} \otimes \underline{A}^{\beta}\right) \\ &= a_{\alpha\beta}\, \underline{A}^{\alpha} \otimes \underline{A}^{\beta}, \end{aligned} \tag{2.13}$$

or by the Green-Lagrange strain tensor

$$\begin{aligned}\underline{\underline{E}} &= \frac{1}{2}\left(\underline{\underline{C}} - \underline{\underline{I_s}}\right) \\ &= \frac{1}{2}\left(a_{\alpha\beta} - A_{\alpha\beta}\right) \underline{A}^{\alpha} \otimes \underline{A}^{\beta}, \end{aligned} \tag{2.14}$$

where $\underline{\underline{I_s}}$ is the tangential projection operator, which can be written as

$$\begin{aligned}\underline{\underline{I_s}} &= a_{\alpha\beta}\, \underline{a}^{\alpha} \otimes \underline{a}^{\beta} \\ &= a^{\alpha\beta}\, \underline{a}_{\alpha} \otimes \underline{a}_{\beta} \\ &= \delta^{\alpha}_{\beta}\, \underline{a}_{\alpha} \otimes \underline{a}^{\beta} \\ &= \delta^{\beta}_{\alpha}\, \underline{a}^{\alpha} \otimes \underline{a}_{\beta}. \end{aligned} \tag{2.15}$$

In order to have an invariant of the strain tensor, which is zero when the areal strain is zero, regardless of the magnitudes of the principal extension ratios λ_1, λ_2, Skalak et al. [78] introduced the two invariants of the in-plane strain tensor

$$\begin{aligned}I_1 &= 2\ \mathrm{tr}\underline{\underline{E}} \\ &= \mathrm{tr}\{\left(a_{\alpha\beta} - A_{\alpha\beta}\right) \underline{A}^{\alpha} \otimes \underline{A}^{\beta}\} \\ &= \left(a_{\alpha\beta} - A_{\alpha\beta}\right) \underline{A}^{\alpha} \cdot \underline{A}^{\beta} \\ &= a_{\alpha\beta} A^{\alpha\beta} - A_{\alpha\beta} A^{\alpha\beta} \\ &= a_{\alpha\beta} A^{\alpha\beta} - 2 \\ &= \lambda_1^2 + \lambda_2^2 - 2, \end{aligned} \tag{2.16}$$

$$
\begin{aligned}
I_2 &= 4\mathrm{det}\underline{\underline{E}} + 2\mathrm{tr}\underline{\underline{E}} \\
&= \det(\underline{\underline{C}}) - 1 \\
&= \det\left(a_{\alpha\beta}\ \underline{A}^{\alpha} \otimes \underline{A}^{\beta}\right) - 1 \\
&= |a_{\alpha\beta}||A^{\alpha\beta}| - 1 \\
&= \lambda_1^2\lambda_2^2 - 1 \\
&= J_s^2 - 1. \qquad (2.17)
\end{aligned}
$$

The Jacobian $J_s = \det\left(\underline{\underline{F_s}}\right) = \lambda_1\lambda_2$, expresses the ratio of the deformed to the reference surface areas.

2.1.3 Membrane tension and constitutive laws

2.1.3.1 Membrane tension

Assuming that the membrane is a two-dimensional isotropic hyper-elastic material, the elastic stresses in an infinitely thin membrane are replaced by elastic tensions. In the case of a hyper-elastic material, the tension-strain relationship derives from a strain energy per unit area of the undeformed membrane W,

$$
\underline{\underline{P}}^{pk} = \frac{\partial W}{\partial \underline{\underline{F_s}}}, \quad \text{or} \quad \underline{\underline{S}}^{pk} = \frac{\partial W}{\partial \underline{\underline{E}}}, \qquad (2.18)
$$

where $\underline{\underline{P}}^{pk}$, $\underline{\underline{S}}^{pk}$ are the first and second Piola-Kirchhof tension, respectively and the Cauchy tension tensor $\underline{\underline{\tau}}$ is given by

$$
\begin{aligned}
\underline{\underline{\tau}} &= \frac{1}{\mathrm{det}\underline{\underline{F_s}}}\ \underline{\underline{F_s}} \cdot \underline{\underline{S}}^{pk} \cdot \underline{\underline{F_s}}^{T} \\
&= \frac{1}{J_s}\ \underline{\underline{F_s}} \cdot \frac{\partial W}{\partial \underline{\underline{E}}} \cdot \underline{\underline{F_s}}^{T}. \qquad (2.19)
\end{aligned}
$$

When the strain energy function W is a function of I_1, I_2, the Cauchy tension tensor can be rewritten as

$$\begin{aligned}\underline{\underline{\tau}} &= \frac{1}{J_s}\underline{\underline{F_s}} \cdot \frac{\partial W(I_1, I_2)}{\partial \underline{\underline{E}}} \cdot \underline{\underline{F_s}}^T \\ &= \frac{1}{J_s}\underline{\underline{F_s}} \cdot \left(\frac{\partial W}{\partial I_1}\frac{\partial I_1}{\partial \underline{\underline{E}}} + \frac{\partial W}{\partial I_2}\frac{\partial I_2}{\partial \underline{\underline{E}}}\right) \cdot \underline{\underline{F_s}}^T. \end{aligned} \tag{2.20}$$

The partial derivations of the invariants with respect to $\underline{\underline{E}}$ are given by

$$\begin{aligned}\frac{\partial I_1}{\partial \underline{\underline{E}}} &= 2\frac{\partial \mathrm{tr}(\underline{\underline{E}})}{\partial \underline{\underline{E}}} \\ &= 2\ \underline{\underline{I_s}}, \end{aligned} \tag{2.21}$$

$$\begin{aligned}\frac{\partial I_2}{\partial \underline{\underline{E}}} &= \frac{\partial(\det\underline{\underline{C}} - 1)}{\partial \underline{\underline{C}}} : \frac{\partial \underline{\underline{C}}}{\partial \underline{\underline{E}}} \\ &= 2\det(\underline{\underline{C}})\ \underline{\underline{C}}^{-T} \\ &= 2J_s^2\underline{\underline{C}}^{-T}. \end{aligned} \tag{2.22}$$

Substituting equations (2.21) and (2.22) into equation (2.20), we have the following expression for the contravariant representation of $\underline{\underline{\tau}}$

$$\begin{aligned}\underline{\underline{\tau}} &= \frac{1}{J_s}\underline{\underline{F_s}} \cdot \left(\frac{\partial W}{\partial I_1}\frac{\partial I_1}{\partial \underline{\underline{E}}} + \frac{\partial W}{\partial I_2}\frac{\partial I_2}{\partial \underline{\underline{E}}}\right) \cdot \underline{\underline{F_s}}^T \\ &= \frac{2}{J_s}\frac{\partial W}{\partial I_1}\underline{\underline{F_s}} \cdot \underline{\underline{I_s}} \cdot \underline{\underline{F_s}}^T + 2J_s\frac{\partial W}{\partial I_2}\underline{\underline{F_s}} \cdot \underline{\underline{C}}^{-T} \cdot \underline{\underline{F_s}}^T \\ &= \frac{2}{J_s}\frac{\partial W}{\partial I_1}\underline{\underline{F_s}} \cdot \underline{\underline{F_s}}^T + 2J_s\frac{\partial W}{\partial I_2}\underline{\underline{F_s}} \cdot \underline{\underline{F_s}}^{-1} \cdot \underline{\underline{F_s}}^{-T} \cdot \underline{\underline{F_s}}^T \\ &= \frac{2}{J_s}\frac{\partial W}{\partial I_1}(\underline{a}_\alpha \otimes \underline{A}^\alpha) \cdot (\underline{A}^\beta \otimes \underline{a}_\beta) + 2J_s\frac{\partial W}{\partial I_2}\underline{\underline{I_s}} \\ &= \left(\frac{2}{J_s}\frac{\partial W}{\partial I_1}A^{\alpha\beta} + 2J_s\frac{\partial W}{\partial I_2}a^{\alpha\beta}\right)\underline{a}_\alpha \otimes \underline{a}_\beta, \end{aligned} \tag{2.23}$$

or

$$\tau^{\alpha\beta} = \frac{2}{J_s}\frac{\partial W}{\partial I_1}A^{\alpha\beta} + 2J_s\frac{\partial W}{\partial I_2}a^{\alpha\beta}. \tag{2.24}$$

2.1.3.2 Constitutive laws

A number of laws are now available for modeling thin hyper-elastic membrane. Different laws allow us to describe quite different material behaviours for large deformation of the membrane, including the strain-softening behaviour of a gelled membrane or the strain-hardening behaviour of a polymerized membrane. In this study, two different constitutive laws are used for the capsule membrane.

The widely used neo-Hookean (NH) law [35] describes the behaviour of a very thin sheet of an isotropic volume-incompressible rubber-like material,

$$W^{NH} = \frac{G_s^{NH}}{2}\left(I_1 - 1 + \frac{1}{I_2 + 1}\right), \tag{2.25}$$

where G_s^{NH} is a surface shear elastic modulus of the NH law.

To model the large deformations of an RBC membrane, Skalak et al. [78] introduced the law (SK)

$$W^{SK} = \frac{G_s^{SK}}{4}\left(I_1^2 + 2I_1 - 2I_2 + CI_2^2\right), \tag{2.26}$$

where G_s^{SK} is a shear elastic modulus of the SK law. The area dilation modulus K_s^{SK} of the SK law can be described as $K_s^{SK} = G_s^{SK}(1 + 2C)$. The RBC membrane has a lipid bilayer structure and is thus almost area incompressible but easy to shear. To model the area-incompressible membrane of the RBC, C must be large enough. Walter et al. [88] investigated the effects of C on the deformation of an ellipsoid capsule in a simple shear flow. They showed that $C = 10$ is high enough to express the area-incompressibility of the membrane. Accordingly, all the results of the RBC presented in this study are obtained with $C = 10$.

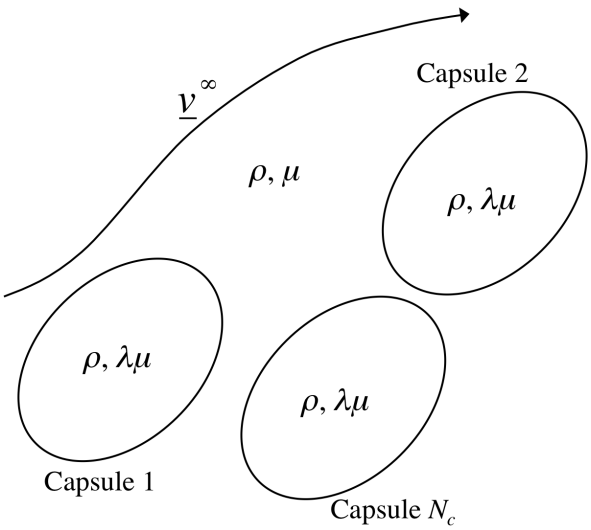

Fig. 2.2 Schematic illustration of a suspension of capsules.

Substituting equations (2.25) or (2.26) into equation (2.24), we can obtain the elastic tensions of the NH or SK laws. In chapter 4, we compare the tension-strain relationship of the two laws under large uniaxial and isotropic deformation.

2.2 Fluid mechanics

Consider N_c capsules are freely suspended in incompressible Newtonian liquid undergoing viscous flow with velocity $\underline{v}^{\infty}(\underline{x})$, as illustrated in figure 2.2. We assume all capsules are filled with an incompressible Newtonian liquid (subscript in) with viscosity $\lambda\mu$ and density ρ and enclosed by an infinitely thin membrane. The outer liquid (subscript out) is Newtonian with viscosity μ and density ρ. Gravitational effects are thus neglected as the capsule is assumed to be neutrally buoyant.

The capsule deformation is governed by fluid-structure interactions between the motion of the internal and external fluids and that of the capsule membrane. In particular, the discontinuity of the stress tensor across the thin membrane has to be taken into account. At the small scale of the capsule, the inertia forces of the internal and external flows are negligible compared to the viscous forces. The fluid velocity field is governed by the Stokes equations and can be evaluated in terms of surface integrals defined on the boundaries of the fluid domain, including the capsule

membrane. The governing equation of the fluid motion for a point $\underline{x}$ can be described as

$$\frac{1+\lambda}{2}\underline{v}(\underline{x}) = \underline{v}^{\infty}(\underline{x}) - \frac{1}{8\pi\mu}\sum_{i=1}^{N_c}\int_{S_i}\underline{\underline{J}}(\underline{x},\underline{y})\cdot\underline{q}(\underline{y})dS_i(\underline{y}) + \frac{1-\lambda}{8\pi}\sum_{i=1}^{N_c}\int_{S_i}^{PV}\underline{v}(\underline{y})\cdot\underline{\underline{\underline{K}}}(\underline{x},\underline{y})\cdot\underline{n}(\underline{y})dS_i(\underline{y}), \tag{2.27}$$

where λ is the viscosity ratio of the internal and external liquids, $\underline{n}$ is the outward unit normal vector to the membrane surface S_i, PV denotes the principal value, which is defined as the value of the improper double layer integral when the point $\underline{x}$ is right on S_i, and

$$\underline{q}(\underline{x}) = \left[\underline{\underline{\sigma^f_{out}}}(\underline{x}) - \underline{\underline{\sigma^f_{in}}}(\underline{x})\right]\cdot\underline{n}(\underline{x}) \tag{2.28}$$

is the viscous load on the membrane, which represents the discontinuous jump of the fluid viscous stress across the interface. Single and double layer potentials of the Green's function $\underline{\underline{J}}$ and $\underline{\underline{\underline{K}}}$ are defined as

$$J_{ij} = \frac{\delta_{ij}}{r} + \frac{r_i r_j}{r^3}, \quad K_{ijk} = 6\frac{r_i r_j r_k}{r^5}, \tag{2.29}$$

where $\underline{r} = \underline{x} - \underline{y}$ and $r = \|\underline{r}\|$.

Here, introduce an important parameter capillary number Ca, which represents the ratio of viscous and elastic forces

$$Ca = \frac{\mu\dot{\gamma}\ell}{G_s}, \tag{2.30}$$

where $\dot{\gamma}$ is the shear rate or elongational rate of undisturbed flow $\underline{v}^{\infty}$ and ℓ is the radius of a sphere that has the same volume as an ellipsoid or a biconcave capsule.

Chapter 3

Numerical methods

In this chapter, we describe numerical methods for the capsule dynamics in viscous flow. For the membrane mechanics of a capsule, including a red blood cell (RBC), a finite element method is used. To discretize the governing equations of the membrane using finite element procedures, the local equilibrium equation of the membrane is described as a weak form, which is based on the virtual work principle. To solve the boundary integral equation of the flow field, a boundary element method is employed. For validations of the numerical scheme of the finite element-boundary element (FE-BE) coupling method, we investigate the membrane load and capsule deformation under inflation and shear flow condition, and the results are compared with former analytical and numerical studies. To accelerate computation speed, general purpose computing on graphics processing units (GPGPU) is applied to the FE-BE coupling method using compute unified device architecture (CUDA) and we succeeded about 230 times acceleration of the computation speed comparing with central processing unit (CPU) computation.

3.1 Finite element method

3.1.1 Weak form of the equilibrium equation

For the finite element procedure, we first introduce the local equilibrium equation in a weak form using the virtual work principle. Consider a 3D material with the volume V and the surface ∂V, immersed in a liquid. Neglect inertia effects of the

material deformation, the static equilibrium equation is given by

$$\underline{\nabla} \cdot \underline{\underline{\sigma}} = \underline{0}, \tag{3.1}$$

where $\underline{\underline{\sigma}}$ is the internal Cauchy stress of the material and $\underline{\nabla}$ is the gradient operator. Based on the virtual work principle, we introduce a virtual displacement $\underline{\hat{u}}$ into the static equilibrium equation:

$$\int_V \underline{\hat{u}} \cdot \left(\underline{\nabla} \cdot \underline{\underline{\sigma}}\right) = 0. \tag{3.2}$$

Using chain rule and Gauss's divergence theorem, equation (3.2) can be rewritten as

$$\begin{aligned}\int_V \underline{\hat{u}} \cdot \left(\underline{\nabla} \cdot \underline{\underline{\sigma}}\right) dV &= \int_V \underline{\nabla} \cdot \left(\underline{\hat{u}} \cdot \underline{\underline{\sigma}}\right) dV - \int_V \underline{\underline{\nabla \hat{u}}} : \underline{\underline{\sigma}} dV \\ &= \int_{\partial V} \underline{\hat{u}} \cdot \underline{\underline{\sigma}} \cdot \underline{n}_{\partial V}\, d\partial V - \int_V \underline{\underline{\nabla \hat{u}}} : \underline{\underline{\sigma}} dV = 0,\end{aligned} \tag{3.3}$$

where $\underline{n}_{\partial V}$ is the unit outward normal vector to the surface ∂V. When the material is exerted by the fluid flow, the surface stress vector $\underline{t}$ is equivalent to the fluid stress vector on the surface

$$\underline{t} = \underline{\underline{\sigma}}^f \cdot \underline{n}_{\partial V} = \underline{\underline{\sigma}} \cdot \underline{n}_{\partial V}, \tag{3.4}$$

where $\underline{\underline{\sigma}}^f$ is the viscous stress of the flow and we have

$$\int_{\partial V} \underline{\hat{u}} \cdot \underline{\underline{\sigma}}^f \cdot \underline{n}_{\partial V}\, d\partial V = \int_V \underline{\underline{\hat{\varepsilon}}} : \underline{\underline{\sigma}} dV, \tag{3.5}$$

where

$$\underline{\underline{\hat{\varepsilon}}} = \frac{1}{2}\left(\underline{\underline{\nabla \hat{u}}} + \underline{\underline{\nabla \hat{u}}}^T\right) \tag{3.6}$$

is the virtual strain.

We now consider the equilibrium equation of a capsule membrane. Based on the Kirchhoff-Love theory for a very thin sheet, straight lines normal to the mid-plane remain straight and normal to the mid-plane after deformation. In this case, the out-of-plane components of the stress tensor $\sigma^{\alpha 3}$ are zero, because $A^{\alpha 3} = a^{\alpha 3} = 0$ in the mid-plane. The thickness of the membrane is very thin and the normal stress σ^{33} may not affect on the internal virtual work, i.e. right hand side of equation (3.5), the internal virtual work may be calculated by only the in-plane stress tensor $\underline{\underline{\sigma_s}}$:

$$\int_V \underline{\underline{\hat{\varepsilon}}} : \underline{\underline{\sigma}} dV \approx \int_V \underline{\underline{\hat{\varepsilon}_s}} : \underline{\underline{\sigma_s}} dV, \tag{3.7}$$

where

$$\underline{\underline{\hat{\varepsilon}_s}} = \frac{1}{2}\left(\underline{\underline{\nabla_s \hat{u}}} + \underline{\underline{\nabla_s \hat{u}^T}}\right) \tag{3.8}$$

and

$$\underline{\nabla_s} = \underline{\underline{I_s}} \cdot \underline{\nabla}, \tag{3.9}$$

is the surface gradient operator. We also assume that the stress tensor is constant in the thickness direction (denoted by ξ^3). The in-plane stress is replaced by the membrane tension $\underline{\underline{\tau}}$ in the mid-plane after integrated towards thickness direction:

$$\begin{aligned}\int_V \underline{\underline{\hat{\varepsilon}_s}} : \underline{\underline{\sigma_s}} dV &= \int_h \int_S \underline{\underline{\hat{\varepsilon}_s}} : \underline{\underline{\sigma_s}}\, dS d\xi^3 \\ &\approx \int_S \underline{\underline{\hat{\varepsilon}_s}} : \underline{\underline{\tau}}\, dS. \end{aligned} \tag{3.10}$$

When we neglect the area difference between the surface S_{in} and S_{out}, the external virtual work, i.e. left hand side of equation (3.5), may be calculated on the mid-plane:

$$\begin{aligned}\int_{\partial V} \underline{\hat{u}} \cdot \underline{\underline{\sigma}}^f \cdot \underline{n}_{\partial V}\, d\partial V &= \int_{S_{out}} \underline{\hat{u}} \cdot \underline{\underline{\sigma^f_{out}}} \cdot \underline{n}\, dS_{out} - \int_{S_{in}} \underline{\hat{u}} \cdot \underline{\underline{\sigma^f_{in}}} \cdot \underline{n}\, dS_{in} \\ &\approx \int_S \underline{\hat{u}} \cdot \left[\underline{\underline{\sigma^f_{out}}} - \underline{\underline{\sigma^f_{in}}}\right] \cdot \underline{n}\, dS \\ &= \int_S \underline{\hat{u}} \cdot \underline{q}\, dS, \end{aligned} \tag{3.11}$$

where $\underline{q}$ is the external viscous load and $\underline{n}$ is the outward unit normal vector to the mid-plane. Finally, we get the equilibrium equation of the membrane in the weak form:

$$\int_S \underline{\hat{u}} \cdot \underline{q}\, dS = \int_S \underline{\underline{\hat{\varepsilon}_s}} : \underline{\underline{\tau}}\, dS. \tag{3.12}$$

Equation (3.12) is solved with respect to $\underline{q}$ in given the instantaneous capsule shape.

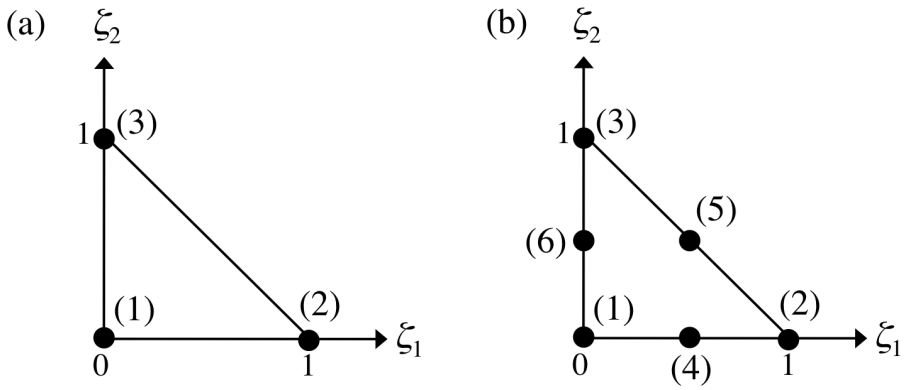

Fig. 3.1 Local curvilinear coordinates (ζ^1, ζ^2) and node numbering for (a) linear element and (b) quadratic element.

3.1.2 Isoparametric interpolation

The surface of a capsule is discretized into a triangular mesh. The local curvilinear coordinates (ζ^1, ζ^2) can be introduced for each element in the interval [0,1]. When calculating the metrics in a given element, the coordinate (ξ^1, ξ^2) are replaced by the intrinsic coordinates in an isoparametric triangular element, (ζ^1, ζ^2), depicted as figure 3.1. In this study, different two types of elements are used for the computation. One is a simple linear element with three nodes at each vertex of a triangle mesh (figure 3.1(a)). The other is a quadratic element with six nodes at each vertex and in the middle of each side (figure 3.1(b)).

Based on a Galerkin method, both physical quantities and virtual displacement are interpolated by the same function, which is called as shape function. For the linear element, the shape function N on the each three nodal point is defined as

$$\begin{aligned} N^{(1)}(\zeta^1, \zeta^2) &= 1 - \zeta^1 - \zeta^2, \\ N^{(2)}(\zeta^1, \zeta^2) &= \zeta^1, \\ N^{(3)}(\zeta^1, \zeta^2) &= \zeta^2, \end{aligned} \tag{3.13}$$

where $N^{(p)}$ is the shape function associated with node $p \in \{1, 2, ..., n_p\}$, and n_p is the number of nodes of the element. For the quadratic element, the shape function is

defined as

$$\begin{aligned} N^{(1)}(\zeta^1,\zeta^2) &= (1-\zeta^1-\zeta^2)(1-2\zeta^1-2\zeta^2), \\ N^{(2)}(\zeta^1,\zeta^2) &= \zeta^1(2\zeta^1-1), \\ N^{(3)}(\zeta^1,\zeta^2) &= \zeta^2(2\zeta^2-1), \\ N^{(4)}(\zeta^1,\zeta^2) &= 4\zeta^1(1-\zeta^1-\zeta^2), \\ N^{(5)}(\zeta^1,\zeta^2) &= 4\zeta^1\zeta^2, \\ N^{(6)}(\zeta^1,\zeta^2) &= 4\zeta^2(1-\zeta^1-\zeta^2). \end{aligned} \tag{3.14}$$

These formulas can be used to interpolate any quantify $\underline{f}$ in a given element:

$$f_I(\zeta^1,\zeta^2) \approx f_I^{(p)} N^{(p)}, \tag{3.15}$$

where subscript I represents Ith Cartesian component and $f_I^{(p)}$ is Ith Cartesian component of $\underline{f}$ at node p.

3.1.3 Finite element formulation

Using equation (3.15), a position vector of a material point in a given element is also interpolated as $\underline{x}(\zeta^1,\zeta^2) = N^{(p)}\underline{x}^{(p)}$. The covariant vector is then given by

$$\underline{a}_\alpha(\zeta^1,\zeta^2) \approx \frac{\partial N^{(p)}}{\partial \zeta^\alpha}\underline{x}^{(p)}. \tag{3.16}$$

The metric tensor can be obtained from this expression. A differential surface element dS can be expressed as

$$\begin{aligned} dS &= \|d\zeta^1\underline{a}_1 \times d\zeta^2\underline{a}_2\| = d\zeta^1 d\zeta^2 \|\underline{a}_1 \times \underline{a}_2\| \\ &= d\zeta^1 d\zeta^2 \sqrt{(\underline{a}_1 \times \underline{a}_2)\cdot(\underline{a}_1 \times \underline{a}_2)} \\ &= d\zeta^1 d\zeta^2 \sqrt{(\underline{a}_1 \cdot \underline{a}_1)\,(\underline{a}_2 \cdot \underline{a}_2) - (\underline{a}_1 \cdot \underline{a}_2)\,(\underline{a}_2 \cdot \underline{a}_1)} \\ &= d\zeta^1 d\zeta^2 \sqrt{|a_{\alpha\beta}|}. \end{aligned} \tag{3.17}$$

For the virtual displacement, we use the same interpolation as the physical quantities and the external virtual work is discretized to

$$\begin{aligned}
\int_S \underline{\hat{u}} \cdot \underline{q} dS &\approx \sum_{el} \int_{S_{el}} \underline{\hat{u}} \cdot \underline{q} dS_{el} \\
&\approx \sum_{el} \hat{u}_I^{(p)} \int_{S_{el}} N^{(p)} N^{(q)} dS_{el}\ q_I^{(q)} \\
&= \sum_{el} \hat{u}_I^{(p)} \int_0^1 \int_0^{1-\zeta^1} N^{(p)} N^{(q)} \sqrt{|a_{\alpha\beta}|} d\zeta^1 d\zeta^2\ q_I^{(q)} \\
&= \sum_{el} \{\hat{u}^{el}\}^T \{M^{el}\} \{q^{el}\} \\
&= \{\hat{u}\}^T \{M\} \{q\}, \qquad (3.18)
\end{aligned}$$

where the index el means elements on the membrane. The size of vector $\{\hat{u}\}, \{q\}$ and the coefficient matrix $\{M\}$ are depends on the type of shape function.

We now consider a covariant expression of the virtual strain. The derivation $\underline{\underline{\nabla_s \hat{u}}}$ in covariant form is given by

$$\begin{aligned}
\underline{\underline{\nabla_s \hat{u}}} &= \underline{\underline{I_s}} \cdot \underline{\underline{\nabla \hat{u}}} \\
&= \left(\delta_\alpha^\gamma\ \underline{a}^\alpha \otimes \underline{a}_\gamma\right) \cdot \frac{\partial \underline{\hat{u}}}{\partial \zeta^\beta} \otimes \underline{a}^\beta \\
&= \delta_\alpha^\gamma\ \underline{a}_\gamma \cdot \frac{\partial \underline{\hat{u}}}{\partial \zeta^\beta}\ \underline{a}^\alpha \otimes \underline{a}^\beta \\
&= \underline{a}_\alpha \cdot \frac{\partial \underline{\hat{u}}}{\partial \zeta^\beta}\ \underline{a}^\alpha \otimes \underline{a}^\beta. \qquad (3.19)
\end{aligned}$$

Substituting $\underline{\hat{u}} = u_i \, \underline{a}^i$ into equation (3.19), we have

$$\begin{aligned}
\underline{\underline{\nabla_s \hat{u}}} &= \left(\underline{a}_\alpha \cdot \frac{\partial \underline{\hat{u}}}{\partial \zeta^\beta} \right) \underline{a}^\alpha \otimes \underline{a}^\beta \\
&= \left(\frac{\partial \hat{u}_i}{\partial \zeta^\beta} \, \underline{a}_\alpha \cdot \underline{a}^i + \hat{u}_i \, \underline{a}_\alpha \cdot \frac{\partial \underline{a}^i}{\partial \zeta^\beta} \right) \underline{a}^\alpha \otimes \underline{a}^\beta \\
&= \left\{ \frac{\partial \hat{u}_i}{\partial \zeta^\beta} \, \delta_i^\alpha + \hat{u}_i \, \left(\frac{\partial \left(\underline{a}_\alpha \cdot \underline{a}^i \right)}{\partial \zeta^\beta} - \frac{\partial \underline{a}_\alpha}{\partial \zeta^\beta} \cdot \underline{a}^i \right) \right\} \underline{a}^\alpha \otimes \underline{a}^\beta \\
&= \left(\frac{\partial \hat{u}_\alpha}{\partial \zeta^\beta} - \hat{u}_i \frac{\partial \underline{a}_\alpha}{\partial \zeta^\beta} \cdot \underline{a}^i \right) \underline{a}^\alpha \otimes \underline{a}^\beta . \qquad (3.20)
\end{aligned}$$

Then, the virtual strain in covariant form is given by

$$\underline{\underline{\hat{\varepsilon}_s}} = \frac{1}{2} \left(\frac{\partial \hat{u}_\alpha}{\partial \zeta^\beta} + \frac{\partial \hat{u}_\beta}{\partial \zeta^\alpha} - 2 \Gamma^i_{\alpha\beta} \hat{u}_i \right) \underline{a}^\alpha \otimes \underline{a}^\beta , \qquad (3.21)$$

where $\Gamma^i_{\alpha\beta}$ is the Christoffel symbol, which is defined by $\Gamma^i_{\alpha\beta} = (\partial \underline{a}_\alpha / \partial \zeta^\beta) \cdot \underline{a}^i$. In the case of $\Gamma^3_{\alpha\beta}$, the Christoffel symbol is equivalent to the curvature tensor which is defined as $b_{\alpha\beta} = \underline{n} \cdot \left(\partial \underline{a}_\alpha / \partial \zeta^\beta \right)$. The covariant component of the virtual displacement must now be expressed in terms its Cartesian components:

$$\hat{u}_i = a_i^I \hat{u}_I \approx N^{(p)} a_i^I \hat{u}_I^{(p)} . \qquad (3.22)$$

Since,

$$\begin{aligned}
\underline{\hat{u}} = \hat{u}_i \underline{a}^i &= \hat{u}_I \underline{e}^I \\
\hat{u}_i \underline{a}^i \cdot \underline{a}_i &= \hat{u}_I \underline{e}^I \cdot \underline{a}_i \\
\delta_i^i \hat{u}_i &= \hat{u}_I a_i^I \underline{e}^I \cdot \underline{e}^I \\
\hat{u}_i &= \hat{u}_I a_i^I . \qquad (3.23)
\end{aligned}$$

Where $\underline{e}^I$ is the bases in the Cartesian system. The virtual strain tensor can therefore be written as

$$\hat{\varepsilon}_{s\alpha\beta} = \hat{u}_I^{(p)} \chi_{\alpha\beta}^{(p)I} , \qquad (3.24)$$

where

$$\chi_{\alpha\beta}^{(p)I} \approx \frac{1}{2}\frac{\partial N^{(p)}}{\partial \zeta^\beta}a_\alpha^I + \frac{1}{2}\frac{\partial N^{(p)}}{\partial \zeta^\alpha}a_\beta^I + N^{(p)}\frac{\partial a_\alpha^I}{\partial \zeta^\beta} - \Gamma_{\alpha\beta}^i N^{(p)} a_i^I. \tag{3.25}$$

The internal virtual work is then given by

$$\begin{aligned}
\int_S \hat{\underline{\underline{\varepsilon}}}_s : \underline{\underline{\tau}}\, dS &= \int_S \hat{\varepsilon}_{s\alpha\beta}\tau^{\alpha\beta} dS \\
&\approx \sum_{el} \hat{u}_I^{(p)} \int_0^1 \int_0^{1-\zeta^1} \chi_{\alpha\beta}^{(p)I}\tau^{\alpha\beta}\sqrt{|a_{\alpha\beta}|}d\zeta^1 d\zeta^2 \\
&= \sum_{el} \{\hat{u}^{el}\}^T \{\Pi^{el}\} \\
&= \{\hat{u}\}^T\{\Pi\}.
\end{aligned} \tag{3.26}$$

The contravariant representation $\tau^{\alpha\beta}$ is already introduced in equation (2.24). The matrix $\{M\}$ and vector $\{\Pi\}$ depend only on the metrics, it can be computed and assembled at each time step, because we track the material point through the computation and the metrics can be explicitly calculated by comparing with its reference shape. The discrete equilibrium equation is now written as

$$\{\hat{u}\}^T\{M\}\{q\} = \{\hat{u}\}^T\{\Pi\}. \tag{3.27}$$

The load $\{q\}$ satisfies equation (3.27) for any virtual displacement, thus we get

$$\{M\}\{q\} = \{\Pi\}. \tag{3.28}$$

In the numerical implementation, surface integration is performed to $\{M\}$ and $\{\Pi\}$ using six Gaussian integral points on each element. We numerically confirmed the results do not change so much when the number of Gaussian integral points larger than 6 (data not shown). Equation (3.28) is solved with respect to $\{q\}$ by a biconjugate gradient stabilized method.

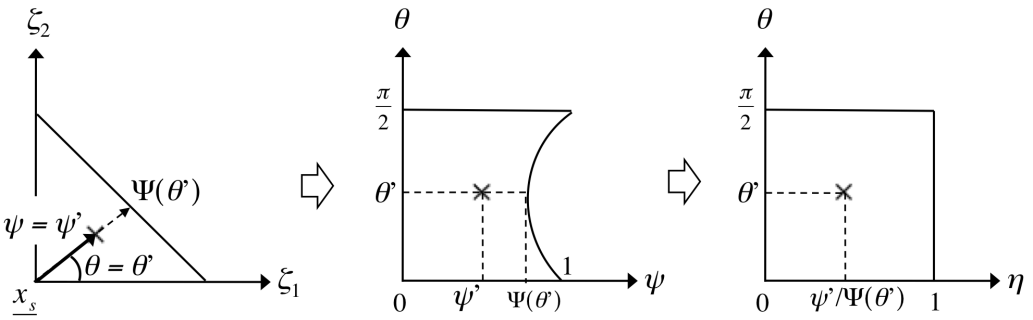

Fig. 3.2 Polar coordinates (ψ, θ) are introduced to calculate the r^{-1} integral at the node $\underline{x_s}$ over the neighboring elements. For simplicity of the numerical integration, the length ψ is normalized by the diagonal length $\Psi(\theta)$, which depends on the angle θ and the normalized system is described as (η, θ). A point (ψ', θ') in the figure represents the integrand point in a given element.

3.2 Boundary element method

3.2.1 Discretization of the boundary integral equation

Next, we describe a discrete boundary integral equation using boundary element method. The capsule surface is discretized by the triangular element and equation (2.27) is discretized to

$$\underline{v}(\underline{x}) \approx \frac{2}{1+\lambda}\underline{v}^{\infty}(\underline{x}) - \frac{1}{4\pi\mu(1+\lambda)}\sum_{cap}^{N_c}\left(\sum_{el}\int_0^1\int_0^{1-\zeta^1}\underline{\underline{J}}(\underline{x},\underline{y})\cdot\underline{q}(\underline{y})\sqrt{|a_{\alpha\beta}|}d\zeta^1 d\zeta^2\right)$$

$$+\frac{1-\lambda}{4\pi(1+\lambda)}\sum_{cap}^{N_c}\left(\sum_{el}\int_0^1\int_0^{1-\zeta^1}\underline{v}(\underline{y})\cdot\underline{\underline{\underline{K}}}(\underline{x},\underline{y})\cdot\underline{n}(\underline{y})\sqrt{|a_{\alpha\beta}|}d\zeta^1 d\zeta^2\right), \qquad (3.29)$$

where N_c is the number of capsules, the indices *cap* and *el* represent the capsules and elements, respectively. We use a Gauss's numerical integration scheme for the second and third terms of the right hand side of equation (3.29). As the same for the finite element procedures, we use six Gaussian integration points. Physical quantities in a given element are interpolated by equation (3.15).

3.2.2 Singular integral for the single-layer potential

The velocity field at a given node $\underline{x}$ is obtained by equation (3.29) where $\underline{\underline{J}}$ and $\underline{\underline{\underline{K}}}$ are nonsingular. Even where each node $\underline{x}$ is shared by neighboring elements, the integrand is calculated do not coincide with the nodes themselves, however the Euclidian distance r in equation (3.29) becomes small enough to generate large errors in the calculation of the improper integral. If the distance between i-th capsule and j-th capsule ($i \neq j$) becomes very small, the singular problems must be considered not only for the neighboring elements but for the capsule-capsule interaction. However, in the parametric range of the capsule interaction used in this study (cf. Chapter 6), the minimum distance between the capsules were always larger than the averaged grid spacing of the membrane. Then, we consider the singular problem only where the nodal point $\underline{x}$ is shared by neighboring elements.

To avoid the singular problem, polar coordinates (ψ, θ) centered at the singular node denoted $\underline{x_s}(\zeta_s^1, \zeta_s^2)$ are introduced for the integration of the single-layer potential $\underline{\underline{J}}$, as shown in figure 3.2, such that

$$\zeta^1 = \zeta_s^1 + \psi\cos\theta, \quad \zeta^2 = \zeta_s^2 + \psi\sin\theta. \tag{3.30}$$

The differential surface element dS can be expressed as $dS = \sqrt{|a_{\alpha\beta}|}\psi d\psi d\theta$. In order to simplify the integration of the single-layer potential, the distance ψ is normalized by the triangular diagonal length $\Psi(\theta)$, as shown in figure 3.2, and the new polar coordinate system is described as (η, θ). The Jacobian between ψ and η can be expressed as $\partial\psi/\partial\eta = \Psi(\theta)$, then the surface element dS is given by

$$dS = \eta\left(\Psi(\theta)\right)^2\sqrt{|a_{\alpha\beta}|}d\eta d\theta. \tag{3.31}$$

The Jacobian $\eta\left(\Psi(\theta)\right)^2$ tends to zero as fast as the Euclidian distance r^{-1} goes to infinity, thus eliminating the singularity in the evaluation of the single-layer integral. In the singular integrals of the single-layer potential, we use 9 Gaussian integral points for numerical accuracies.

3.2.3 Integral for the double-layer potential

Singularity of the r^{-1} integral of the single-layer potential can be eliminating by introducing polar coordinates (η, θ). However, the double-layer potential $\underline{\underline{\underline{K}}}$ is the order of r^{-2} and another method may be needed to handle the singularity of $\underline{\underline{\underline{K}}}$.

Consider the r^{-2} integral of the double-layer potential in i-th capsule. When we seek the velocity at a nodal point $\underline{x}$, the r^{-2} integral equation of the double-layer potential can be rewritten as

$$\int_S \underline{v}(\underline{y}) \cdot \underline{\underline{\underline{K}}}(\underline{x}, \underline{y}) \cdot \underline{n}(\underline{y}) dS(\underline{y}) = \int_S \big(\underline{v}(\underline{y}) - \underline{v}(\underline{x})\big) \cdot \underline{\underline{\underline{K}}}(\underline{x}, \underline{y}) \cdot \underline{n}(\underline{y}) dS(\underline{y}) + \underline{v}(\underline{x}) \cdot \int_S \underline{\underline{\underline{K}}}(\underline{x}, \underline{y}) \cdot \underline{n}(\underline{y}) dS(\underline{y}). \tag{3.32}$$

Integral in the second term of the right hand side of equation (3.32) is equivalent to the identity tensor:

$$\int_S \underline{\underline{\underline{K}}}(\underline{x}, \underline{y}) \cdot \underline{n}(\underline{y}) dS(\underline{y}) = -4\pi \underline{\underline{I}}. \tag{3.33}$$

Substituting equation (3.33) into equation (3.32), we get another expression of the r^{-2} integral:

$$\int_S \underline{v}(\underline{y}) \cdot \underline{\underline{\underline{K}}}(\underline{x}, \underline{y}) \cdot \underline{n}(\underline{y}) dS(\underline{y}) = \int_S \big(\underline{v}(\underline{y}) - \underline{v}(\underline{x})\big) \cdot \underline{\underline{\underline{K}}}(\underline{x}, \underline{y}) \cdot \underline{n}(\underline{y}) dS(\underline{y}) - 4\pi \underline{v}(\underline{x}). \tag{3.34}$$

When an integrand point $\underline{y}$ is close to $\underline{x}$, the velocity difference $\big(\underline{v}(\underline{y}) - \underline{v}(\underline{x})\big)$ tends to zero and the numerical error arising from the singular problem of the double-layer potential can be suppressed.

At each time step, the implicit problem of equation (3.29) is solved for $\underline{v}(\underline{x})$ by successive sub-interactions (denoted by the superscript n). In this study, we use a simple relaxation method

$$\underline{v}^{n+1}(\underline{x}) = \omega \underline{v_s}^{n+1}(\underline{x}) + (1 - \omega)\underline{v}^n(\underline{x}), \tag{3.35}$$

where $\underline{v_s}^{n+1}$ is the left hand side of equation (3.29) obtained by replacing $\underline{v}(\underline{x})$ by $\underline{v}^n(\underline{x})$ in the right hand side of the equation. ω is a relaxation factor. Foessel et

al. (2011) show the effective relaxation factor numerically, which is equivalent to $\omega = 1.8/(1+\lambda)$. In this study, we use the same relaxation factor as Foessel et al. (2011).

3.3 Reference shape and mesh generation

To discretize a capsule membrane, as well as an RBC membrane, we use a subdividing method as the same manner with [88]. The first mesh is constructed by an icosahedron with 20 regular triangles. A new computational node is placed at the middle of each edge, therefore, each triangle element is divided into 4 new elements. The new nodes are projected onto the sphere with the radius ℓ and the procedure is repeated until the desired number of element is reached.

In this study, we consider deformation of a spheroidal capsule and biconcave disk in shear flow . For a spheroidal capsule, the revolution axis is set along to x_2-direction at time $t = 0$ in the Cartesian system (x_1, x_2, x_3). The reference shape of the spheroidal capsule is then given by

$$\left(\frac{X_1}{b}\right)^2 + \left(\frac{X_2}{a}\right)^2 + \left(\frac{X_3}{b}\right)^2 = 1, \tag{3.36}$$

where a and b are the length of semi-axes along the revolution axis and the orthogonal axis, respectively and X_i is the position of computational node on the membrane. When $a/b < 1$, the spheroid is oblate and when $a/b > 1$, it is prolate. In the case of the spheroidal capsule, the length scale ℓ is defined to conserve the volume between the spherical and spheroidal capsule:

$$\ell = \sqrt[3]{ab^2}. \tag{3.37}$$

The biconcave disk shape, which is assumed as the reference shape of the RBC, is given in the same manner with [27, 73]. The computational node X_i is initially generated on a spherical surface with radius ℓ, then projected onto the derived biconcave shape X_i^{rbc} by using the following transformation functions.

$$X_1^{rbc} = \frac{R_0}{\ell} X_1,\ X_2^{rbc} = \frac{R_0}{2\ell}(1-r^2)^{1/2}(C_0 + C_2 r^2 + C_4 r^4),\ X_3^{rbc} = \frac{R_0}{\ell} X_3, \tag{3.38}$$

where $r^2 = X_1^2 + X_3^2$, and $2R_0$ is the long axis of the biconcave (c.f. figure 3.3). C_0, C_2, C_4 are the shape parameters to control the swelling ratio of the biconcave shape.

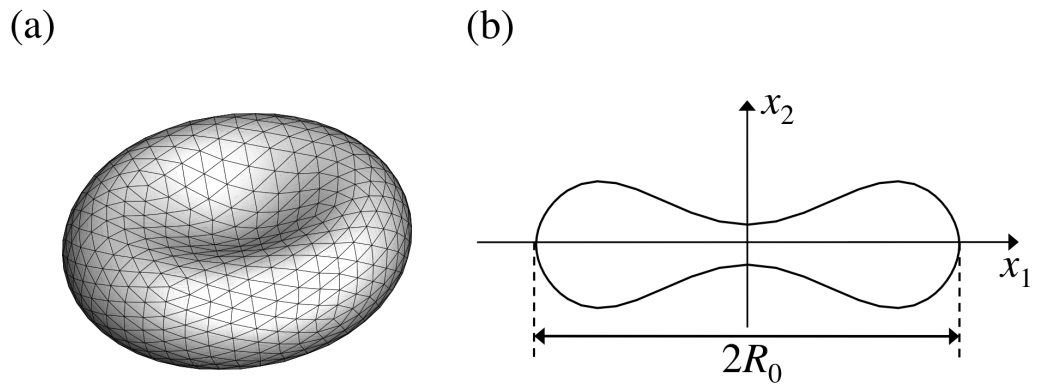

Fig. 3.3 Reference shape of a red blood cell: (a)Membrane of the RBC is discretized to triangular element using a subdividing method. (b) In order to preserve the volume between the spherical capsule with radius ℓ and biconcave capsule with the radius of the long axis R_0, the correlation between R_0 and ℓ is defined as $R_0 = 1.386\ell$.

In order to coincide with the shape as in the physiological condition, these parameters are set to $C_0 = 0.207$, $C_2 = 2.003$, and $C_4 = -1.123$, respectively [27]. R_0 and ℓ have the correlation $R_0 = 1.386\ell$ to preserve the volume of the capsule.

We track the Lagrangian position of the membrane material points over time; we can thus readily compute the local membrane deformation by comparing with the reference state. The in-plane elastic tensions $\underline{\underline{\tau}}$ are obtained from the membrane constitutive law. The viscous load $\underline{q}$ for a given membrane deformation is calculated from equation (3.28). Once the viscous load is given, the velocity field is calculated by the boundary element method. The membrane material point $\underline{x}$ is updated by means of the kinematic condition $\underline{v} = d\underline{x}/dt$, which guarantees continuity between the membrane velocity and the interfacial fluid velocity. The above kinematic equation is solved using an explicit second-order Runge-Kutta method and the whole process is repeated.

3.4 Validations

In this section, we investigate the numerical accuracy of the FE-BE coupling method. First, we investigate the membrane load $\underline{q}$ under inflation of a spherical capsule with the neo-Hookean and the Skalak membrane. Next, we investigate deformation of a spherical capsule and oblate spheroidal capsule in shear flow with various capillary number. The results are compared with analytical solutions and former numerical studies.

3.4.1 Inflation of a capsule

First, we investigate the accuracy of the finite element method on the capsule deformation by inflation of a spherical capsule. When a spherical capsule is inflated by pressure difference between the internal and external fluids, such as due to an osmotic pressure difference across the membrane, the correlation between the isotropic membrane tension τ and internal pressure p can be described by Laplace's equation

$$p = \frac{2\tau}{\ell_p} = \frac{2\tau}{(1+\alpha)\ell}, \tag{3.39}$$

where ℓ is the reference radius of the spherical capsule, α is the inflation ratio, and ℓ_p is the radius of the inflated capsule. The isotropic membrane tension can be related to the principal stretch ratio $\lambda(= 1+\alpha)$. The analytical solution for the NH membrane isotopic tension is given by

$$\tau^{NH} = G_s \left(1 - \lambda^{-6}\right), \tag{3.40}$$

and for the SK membrane

$$\tau^{SK} = G_s \left(\lambda^2 - 1 + C\lambda^2(\lambda^4 - 1)\right), \tag{3.41}$$

where G_s is the surface elastic shear modulus. In order to check the non-linear behaviour of the finite element method, we impose a normal displacement given by $\underline{u} = \alpha \underline{X}$, where $\underline{X}$ is the position vector of a material point in the reference state and equation (3.28) is solved with respect to $\{q\}$. Such a case the norm $\|\underline{q}\|$ should be equal to pressure p.

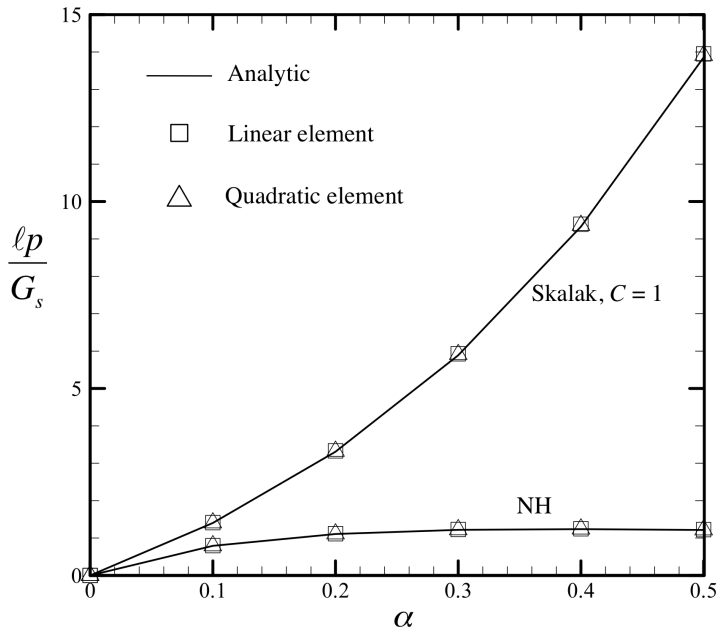

Fig. 3.4 Non-dimensional pressure for the NH and Skalak ($C = 1$) membrane. Analytical solution is given by equation (3.38). For both types elements, we use 1280 triangle meshes.

The results are shown in figure 3.4. The membrane is discretized by the linear and quadratic element with 1280 triangular meshes and 6 Gaussian integral points are used. When α takes a value between 0 to 0.5, we see good agreement with the analytical solutions and the numerical results with linear element and quadratic element, for both the NH and SK laws.

To investigate the accuracy of the finite element method more in detail, we define the numerical error as follow:

$$\text{Error} = |p^n_{ave} - p^a|/p^a, \tag{3.42}$$

where p^n_{ave} is averaged pressure obtained from the computation and p^a is the exact analytical solution. Numerical errors of the finite element method with various mesh number are shown in figure 3.5. The membrane is modeled by the SK law with $C = 1$ and the stretch ratio $\alpha = 0.5$. From this figure, we see a linear correlation between the numerical error and mesh number of the membrane for both linear element and

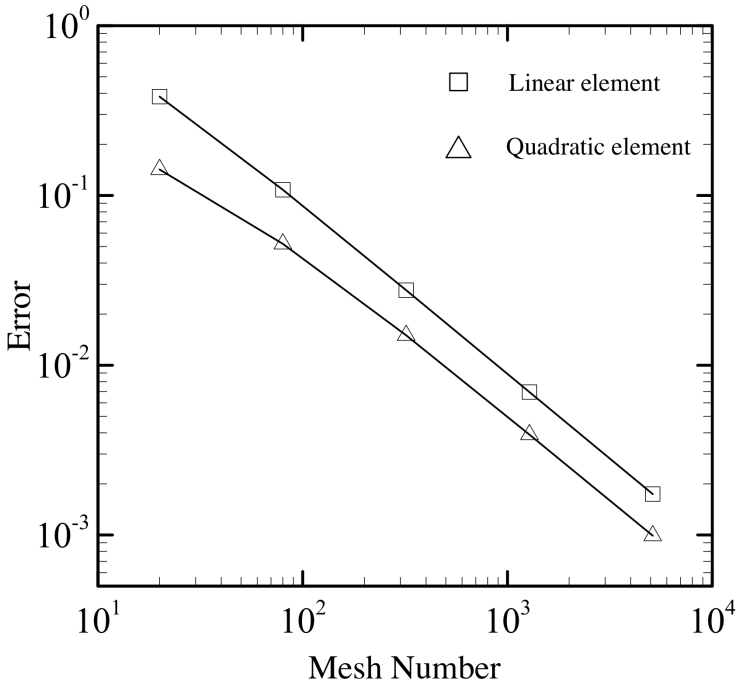

Fig. 3.5 Numerical error of the finite element method. The error is defined in equation (3.42). The membrane is modeled by the SK law with $C = 1$ and the stretch ratio $\alpha = 0.5$.

quadratic element. Slopes of the linear element and quadratic element are almost same when the mesh number is larger than 10^2. This result suggests that the linear element can be applied for the capsule inflation when the membrane is discretized by large enough mesh numbers, even though the curvature of the meshes are neglected. When the membrane is discretized by 5120 meshes, the error is about 0.2% for the linear element and about 0.1% for the quadratic element. From these results, we confirm that our numerical methods for the membrane mechanics have a good accuracy to solve the capsule inflation.

3.4.2 Capsule in shear flow

Next, we check the accuracy of the FE-BE coupling method under shear flow condition. We assume a spherical capsule is freely suspended in a simple shear flow in

the (x_1, x_2)-plane. The undisturbed background flow $\underline{v}^\infty$ is then given by

$$v_1^\infty = \dot{\gamma} x_2, \quad v_2^\infty = v_3^\infty = 0, \tag{3.43}$$

where $\dot{\gamma}$ is the shear rate. The capsule deformation is defined by the Taylor parameter, which is calculated from the deformation of its ellipsoid inertia. By symmetry, the material points initially located in the shear plane (x_1, x_2) remain in it and two of the principal axes of the ellipsoid of inertia with semi-axes L_1 and L_2 $(L_1 \geq L_2)$ are also located in the shear plane. Correspondingly, it is convenient to quantify the three-dimensional capsule deformation with the deformation of the intersection of the profile with the shear plane. The Taylor deformation parameter is then defined as

$$D_{12} = \frac{|L_1 - L_2|}{L_1 + L_2}. \tag{3.44}$$

3.4.2.1 Mesh convergence

We first check the mesh convergence of the numerical method by deformation of a spherical capsule in shear flow. The membrane is modeled by the Skalak law with $C = 1$. Capillary number and the viscosity ratio are equal to 1. Time change of Taylor parameter with various mesh number are shown in figure 3.6. The values of D_{12} in the steady state obtained from linear element with 320 and 1280 meshes differ about 2.6%. When the membrane is discretized by the linear element with 1280 and 5120 meshes, the curves of D_{12} are almost overlapped between the two cases and the values of D_{12} in the steady state differ less than 0.5% between the two cases.

To investigate the mesh convergence of the numerical method more in detail, following criterion is introduced:

$$\text{Diff} = \frac{|D_{12} - D_{12}^{fine}|}{D_{12}^{fine}}, \tag{3.45}$$

wehre D_{12}^{fine} is the Taylor parameter of the fine mesh in the steady state, which is evaluated as the reference value. Results of the linear element and quadratic element with various mesh numbers are shown in figure 3.7. Numerical conditions are the same as figure 3.6, and D_{12}^{fine} is estimated from the results of the linear element with 20480 meshes. The values of Diff decreases as mesh number increases for both the linear

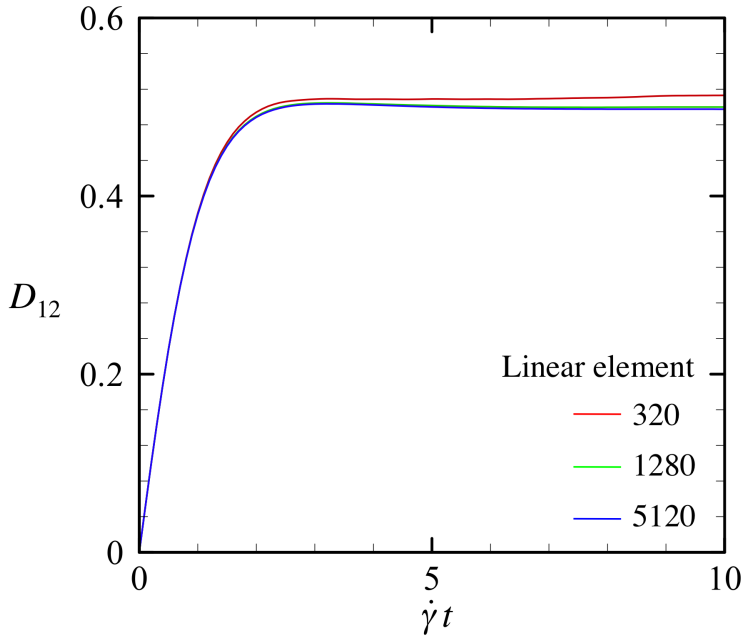

Fig. 3.6 Time change of Taylor parameter. The membrane is modeled by the Skalak law with $C = 1$. Capillary number and the viscosity ratio are equal to 1.

and quadratic element. When the mesh number is higher than 10^3, the maximum difference with the fine mesh is less than 0.6% for the linear element and 0.3% for the quadratic element. From these results, we confirm that the mesh convergence of the numerical method when the membrane is discretized by 10^3 or more higher number of meshes.

3.4.2.2 Comparison with former analytical and numerical studies

Next, we compare our results of a spherical capsule in shear flow with Barthès-Biesel [6], Lac et al. [46] and Foessel et al. [31], in which all capsule membranes are modeled by the SK law with $C = 1$. The membrane is discretized by the linear element with 5120 meshes. The results are shown in figure 3.8. The green line indicates the linear correlation between Ca and D_{12} in the small deformation limit [6], and our results match well with the analytical solution when $Ca < 0.05$. Our results also match well with Lac et al. [46] when $\lambda = 1$ and match well with Foessel et al. [31] when $\lambda = 5$ in whole range of Ca. Thus, it is confirmed that our numerical methods have

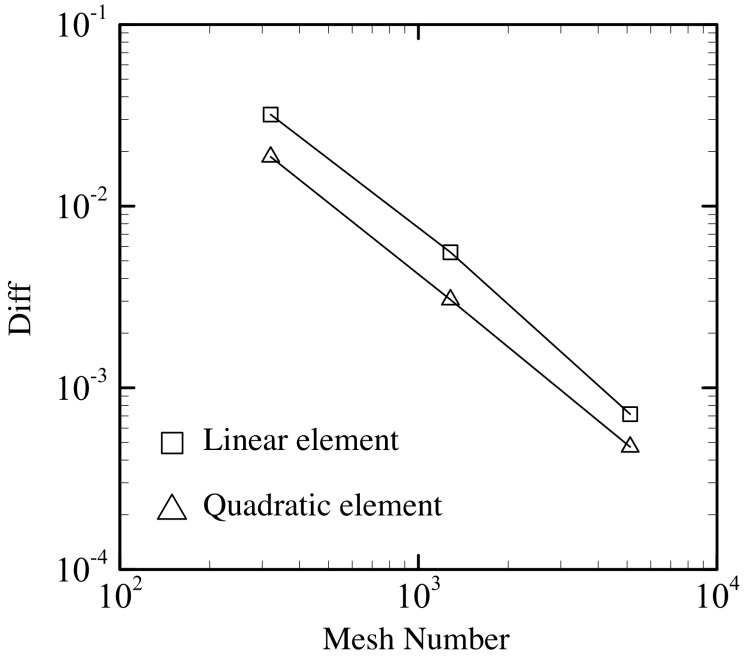

Fig. 3.7 Mesh convergence of the numerical method. D_{12} difference between a given mesh number and the fine mesh is defined as equation (3.45). For the reference value of the fine mesh is estimated from the results of the linear element with 20480 meshes.

good accuracy in simulating the deformation of a spherical capsule in shear flow with various Ca and λ.

Subsequently, we compare our results of an oblate spheroidal capsule ($a/b = 0.5$) in shear flow with Walter et al. [88], in which both capsule membranes are modeled by the neo-Hookean law. Time change of Taylor parameter of the spheroidal capsule with $Ca = 0.6$ is shown in figure 3.9. The viscosity ratio λ is set unity for both studies. Both results match well, which indicates that our numerical methods have good accuracy in simulating the deformation of a spheroidal capsule in shear flow.

From these results, we conclude that our numerical method have good accuracy in simulating a capsule in shear flow with various membrane model, reference shape, capillary number and viscosity ratio for both linear element and quadratic element.

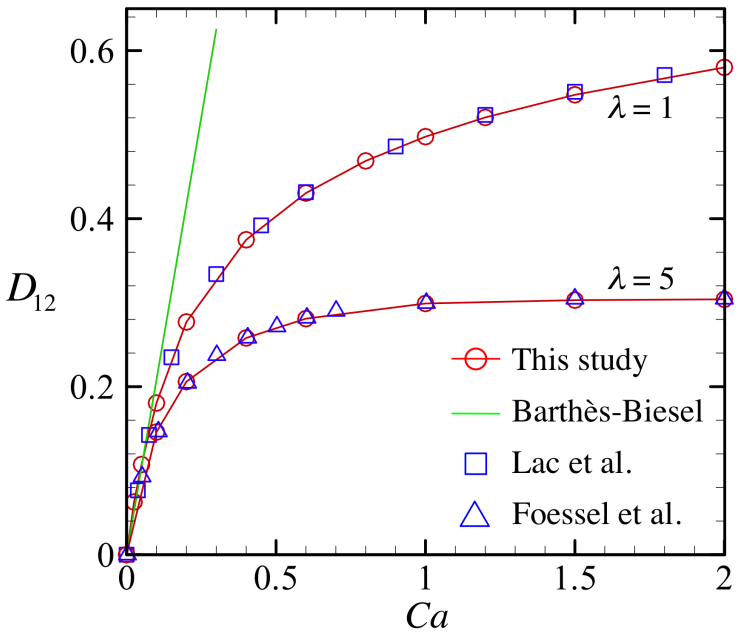

Fig. 3.8 Deformation of a spherical capsule in shear flow with various Ca and λ. The membrane is modeled by the SK law with $C = 1$. The results are compared with former analytical study for the small deformation limit: Barthès-Biesel [6], and numerical studies: Lac et al and Foessel et al. [46, 31].

3.5 GPU computation

To accelerate computation speed, general purpose computing on graphics processing units (GPGPU) is applied to the FE-BE coupling method using compute unified device architecture (CUDA). A graphics processing unit (GPU) (e.g. Geforce GTX580, NVIDIA shown in figure 3.10) is usually equipped in computers to output image to display devices. To compute 2D or 3D image datas quickly, GPU normally has many processors specialized for image processing, which are called as streaming processors. In 2011 winter, high performance GPU has 5 hundred of streaming processors, whereas central processing unit (CPU) has at most 12 cores which can be used for general-purpose computations. Thus, we can say that GPU has specialized architectures for vectorized computation. Another characteristics of GPU is that it has very wide band-width memory compared to CPU, which allows to reduce memory access

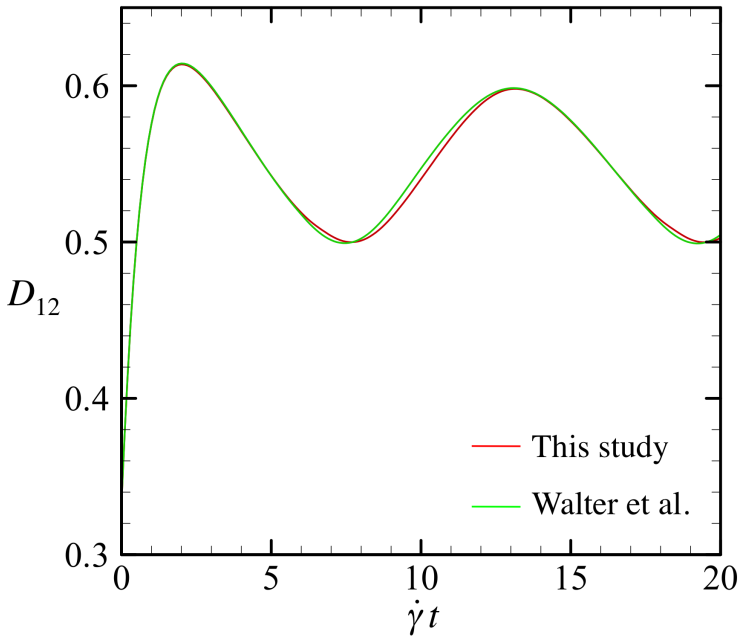

Fig. 3.9 Comparison with former numerical study of Walter et al. [88]. The capsule is modeled as a oblate spheroid capsule with $a/b = 0.5$ and the NH law is used for both studies. Capillary number is equal to 0.6 and the viscosity ratio $\lambda = 1.0$.

Fig. 3.10 GPU device: Geforce GTX580, NVIDIA

time. In 2006, NVIDIA corporation introduced computation library which is called as CUDA for general purpose computing with GPU. CUDA has good compatibility with traditional C language, then many developers are now applying GPGPU to computational fluid dynamics with CUDA. In this study, all computational procedures, described in the previous sections, are performed on GPU device using CUDA

Table. 3.1 Environments of GPU and CPU computations and numerical conditions

	GPU	CPU	Numerical conditions
Processor	NVIDIA Geforce GTX580 (using 1 device)	Intel Core i7-2600 (using 1 core)	- Capsule in shear flow, $Ca = 1.0$, $\lambda = 1.0$, SK $C = 1.0$ - Linear element with 5120 meshes - 6 Gaussian integral points per element - 9 Gaussian integral points per singular element
Compiler	nvcc ver. 4.0	gcc ver. 4.4.5	
Compiler option	-arch=sm_11	-O3	
Precision	Single	Double	

to accelerate the computation. It is hard to compare exact performance between CPU and GPU computations, because exact knowledge of hardware architectures are needed to optimize the computations, especially for optimizing CPU computations. Besides, the performance strongly depends on its definition and the environment, including numerical parameters such as the mesh number. We then simply compare the computational time between CPU and GPU computation without optimization. The computational time used for the comparison is defined as the time which is required for 1 computational time step. The principal numerical environments and numerical conditions are shown in table 3.1. The computation speed with GPU is about 230 times larger than CPU computation. Thus, we succeed acceleration of the computation with GPGPU.

Chapter 4

Mechanical modeling of an RBC membrane

4.1 Introduction

The model chosen to solve the solid mechanics of a capsule membrane plays a key role in the global accuracy of the simulation. The membrane thickness of a capsule is typically much smaller than the cell size. In such a case, one may average the stress distribution across the thickness and assume the membrane to be a two-dimensional (2D) sheet. Several 2D constitutive laws have been proposed to model the mechanical behaviour of a hyperelastic surface. For example, the neo-Hookean (NH) [35] law has been used for isotropic volume-incompressible rubber-like materials. Area incompressible biological cell membranes are well modeled by the law introduced by Skalak et al. [78] (SK). It is now generally accepted that SK law can be extended to other types of hyperelastic materials, such as reticulated membranes that have low resistance to area dilation [14].

The dynamic response of a capsule (initially spherical, ellipsoidal or biconcave) has been extensively investigated for different membrane constitutive laws. The capsule deformation has been studied in various flow types, simple shear flow [25, 44, 46, 53, 69, 71, 73], Poiseuille tube flow [21, 22, 23, 49] and elongational flow [20, 24]. In some rare cases, the bending stiffness of the membrane has been taken into account [45]. These previous studies have clarified the influence of the membrane law on the capsule deformation.

Many researchers have used discrete spring network models to represent the membrane of capsules and biological cells. One of the main advantages of the spring network models is the simplicity of the mathematical description. One can avoid the numerical implementation of the complicated solid mechanics of the continuous models. In particular, spring network models have been used to model the membrane of red blood cells (RBC), that consists primarily of a phospholipid bilayer and an elastic spectrin network. From a mechanical point, the lipid bilayer strongly resists local area change but the elasticity of the cytoskeleton enables the RBC to undergo large extensional deformation while maintaining the structural integrity of the membrane. Hansen et al. [36] have modeled the RBC membrane with an unstructured triangular network of identical linear springs. They have calculated the macroscopic elastic shear modulus and area expansion modulus of the model and show that the mechanical properties of the spring network depend on the network configuration. Their study, however, is limited to small deformation. Navot [64] computed the strain energy of a spring network model and compared it to NH law.

Spring network models have been used also to model the motion of red blood cells in different flows such as 2D pore flow [66, 75, 84], 2D rouleaux dynamics [90], tank-treading behavior of a discocyte [85]. However, it is unclear whether modeling the membrane with a spring network is sufficiently accurate to reproduce the complex behaviour of capsules and cells. Furthermore, the values used for the spring models are often empirical and obtained for small deformation.

In this chapter, we investigate the influence of the membrane model on the dynamics of a capsule in flow. We thus compare a discrete spring network and different continuum membrane models in the domain of *large deformations* that are commonly encountered for capsules or cells. Different spring network configurations are considered that correspond to different meshing strategies for a capsule membrane. We first show how the spring constant must be adjusted so that a discrete spring model has the same small deformation elastic properties as a continuum model and investigate the effect of mesh resolution. We then show how the type of model used for the membrane affects the large deformation behavior of an initially spherical capsule in a simple shear flow.

4.2 Models for a two-dimensional RBC membrane

4.2.1 Continuum models

When the thickness of a capsule membrane is small compared to the capsule dimensions and typical radius of curvature, the membrane can be modeled as a hyperelastic surface with negligible bending resistance and surface shear elastic modulus G_s, surface Young modulus E_s, surface Poisson ratio ν_s, area dilatation modulus K_s. Of course, only two of those moduli are independent as they are related by the classical relations of elasticity:

$$K_s = G_s \frac{1+\nu_s}{1-\nu_s}\,,\ E_s = 2G_s(1+\nu_s)\,, \tag{4.1}$$

For such an infinitely thin membrane, the principal components ε_1 and ε_2, of the Lagrange in-plane deformation tensor are related to the two principal extension ratios λ_1 and λ_2 by

$$\varepsilon_\alpha = (\lambda_\alpha^2 - 1)/2, \quad \alpha = 1, 2 \tag{4.2}$$

Elastic stresses are replaced by elastic tensions that correspond to the forces per unit arc length measured in the plane of the membrane. When the membrane is isotropic in its plane, the principal directions of deformation and stress are co-linear. A simple way to express the membrane constitutive law is thus to relate the two principal tensions τ_1 and τ_2 to the two principal extension ratios λ_1 and λ_2 (Figure 4.1). The Young modulus E_s is obtained from a uniaxial stretching experiment, for example in the x_1 direction : $\tau_1 \neq 0, \tau_2 = 0$. In the limit of small deformation

$$\tau_1 = \frac{E_s}{2}(\lambda_1^2 - 1) = E_s\varepsilon_1. \tag{4.3}$$

The area dilation modulus K_s is obtained from isotropic stretching ($\tau_1 = \tau_2 = \tau$) and in the limit of small deformation is given by :

$$\tau = K_s(\lambda_1\lambda_2 - 1) = K_s\Delta S/S, \tag{4.4}$$

where $\Delta S/S$ is the relative area change.

A number of laws are available to model thin hyperelastic membranes. Each law may model different material behaviours under large deformation. It is therefore

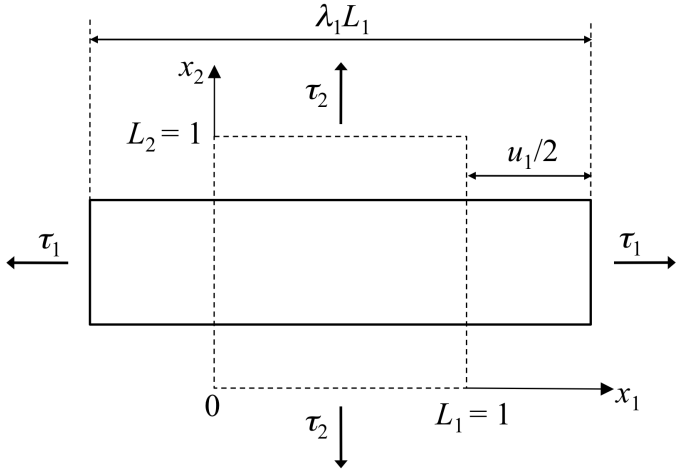

Fig. 4.1 Deformation of a 2D sheet along the principal axes. The broken and solid lines represent the reference and deformed states of the sheet, respectively. The deformation in the x_1 direction is defined by the stretch ratio λ_1 or by the displacement u_1 (with similar definitions in the x_2 direction). τ_1 and τ_2 are the tensions in the x_1- and x_2-directions, respectively.

possible to reproduce the strain-softening of gelled membranes or the strain-hardening of reticulated capsules with strong covalent links. For each law, we give only the expression for τ_1 as a function of deformation. Tension τ_2 may be found by inverting the indices 1 and 2. In the small deformation limit, all laws reduce to the two-dimensional Hooke's law (H)

$$\tau_1^H = \frac{G_s}{1-\nu_s}[\lambda_1^2 - 1 + \nu_s(\lambda_2^2 - 1)], \tag{4.5}$$

where the surface Poisson ratio, $\nu_s \in]-1, +1[$, is related to the area dilation modulus K_s according to equation (4.1). An area-incompressible membrane thus corresponds to $\nu_s \to 1$.

The 2D neo-Hookean law (NH) describes the behavior of an infinitely thin sheet of a three-dimensional isotropic material that is volume incompressible

$$\tau_1^{NH} = \frac{G_s^{NH}}{\lambda_1\lambda_2}\left[\lambda_1^2 - \frac{1}{(\lambda_1\lambda_2)^2}\right]. \tag{4.6}$$

For small deformation, the correspondence between the material properties and the law parameters is

$$G_s = G_s^{NH}\,,\ E_s = 3G_s\,,\ \nu_s = 1/2\,,\ K_s = 3G_s. \tag{4.7}$$

The law (SK) derived by Skalak et al. [78] for two-dimensional materials has independent surface shear and area dilation moduli

$$\tau_1^{SK} = G_s^{SK}\left[\frac{\lambda_1}{\lambda_2}(\lambda_1^2 - 1) + C\lambda_1\lambda_2(\lambda_1^2\lambda_2^2 - 1)\right]. \tag{4.8}$$

For small deformation, the correspondence between the material properties and the law parameters is

$$\begin{aligned} G_s = G_s^{SK}\ ,\ E_s = 2G_s\frac{2C+1}{C+1}, \\ \nu_s = \frac{C}{C+1}\ ,\ K_s = G_s(1+2C). \end{aligned} \tag{4.9}$$

For large deformation, the condition $\tau_2 = 0$ provides an expression of λ_2 as a function of λ_1 that can be reported in equations (4.5), (4.6), (4.7) to provide the expression of the tension τ_1 for the different constitutive laws. For large uniaxial deformation, the variation of τ_1 with ε_1 is non linear. It can be shown that SK law is strain-hardening, whereas NH law is strain-softening [8].

4.2.2 Spring network models

Consider a spring network to model the capsule membrane. A 2D sheet is discretized as a network of springs, with frictionless hinges at the nodal points. We assume that all the springs have the same elastic resistance proportional to the length change of the springs. Four kinds of mesh configuration are used in this study. Triangular meshes are often used to model the spectrin network of red blood cell membranes. We discuss the effect of mesh topology on the mechanical properties of the network.

4.2.2.1 Nodal forces

In general Cartesian coordinates, the spring force $\underline{f}_{ij}$ between two nodal points, i and j, is equal to

$$\underline{f}_{ij} = k(\|\underline{r}_{ij}\| - \|\underline{r}_{0,ij}\|)\frac{\underline{r}_{ij}}{\|\underline{r}_{ij}\|},\ \text{with}\ \underline{f}_{ji} = -\underline{f}_{ij}, \tag{4.10}$$

where $\underline{r}_i$ and $\underline{r}_j$ are the position vectors of the nodal points i and j, $\underline{r}_{ij} = \underline{r}_j - \underline{r}_i$ and $\|\underline{r}_{0,ij}\|$ is the equilibrium length between nodes i and j. The spring constant is k.

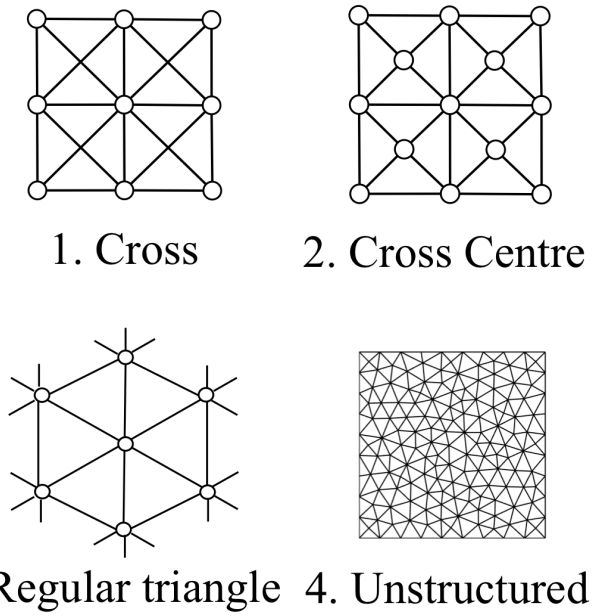

Fig. 4.2 The material is discretized by 4 types of mesh: cross, cross centre, regular triangle and unstructured.

4.2.2.2 Mesh Configuration

A 2D sheet in the (x_1, x_2) plane has initial length L_1 and width L_2. It is discretized with four different meshes (Figure 4.2). In the cross mesh (1), the membrane is discretized by squares with diagonal lines. This mesh is similar to the one used by Navot [64] to discuss correlations between the spring network model and the NH law. In the cross-centre mesh (2), nodal points are added at the intersections of the diagonal lines. In the regular-triangle mesh (3), the mesh is based on regular hexagons with a central node. An unstructured mesh (4) is created with the commercial mesh generator, Gridgen (ver. 15; Vinas Co., Ltd., Japan), based on the Delaunay triangulation algorithm.

The initial boundary grid spacings ΔL_1 and ΔL_2 are given by $\Delta L_1 = L_1/n$ and $\Delta L_2 = L_2/m$, where n and m are the number of boundary segments in the x_1- and x_2-directions, respectively. In this study, initial values of L_1 and L_2 are set to 1.0. A nodal point is described by its initial position $(X_1,\ X_2)$ and by $x_1(X_1, X_2)$ and $x_2(X_1, X_2)$ in its deformed configuration.

The L_1L_2 sheet is deformed by applying prescribed displacements at the edges

$$x_1(0, X_2) = -u_1/2, \quad x_1(L_1, X_2) = L_1 + u_1/2, \tag{4.11}$$
$$x_2(X_1, 0) = -u_2/2, \quad x_2(X_1, L_2) = L_2 + u_2/2. \tag{4.12}$$

4.2.2.3 Numerical computation of a spring network

The tension-strain relationship of 2D spring sheets is computed numerically for uniaxial and isotropic deformation. Although we are only interested in the steady state, it is numerically convenient to have a time-dependent term in the momentum equation, so that one can use an explicit time-marching scheme. The momentum equation at each node may be modified as the balance between an artificial damping force and the spring forces

$$\kappa \underline{v}_i = \sum_j \underline{f}_{ij} = \underline{F}_i, \tag{4.13}$$

where κ is the artificial damping coefficient and $\underline{v}_i$ is the velocity of node i. The viscous term has no physical meaning and generates no force when the system reaches the steady state. Using an Euler explicit scheme, the above equation can be discretized as

$$\underline{r}_i(t + \Delta t) = \underline{r}_i(t) + \frac{\Delta t}{\kappa} \underline{F}_i(t), \tag{4.14}$$

where Δt is the time step. The convergence of the numerical simulation is defined by

$$\max[\frac{\underline{r}_i(t + \Delta t) - \underline{r}_i(t)}{\Delta t}] \leq 10^{-12}. \tag{4.15}$$

The boundary conditions are those provided by (4.11) and (4.12) with $u_2 = 0$ for uniaxial deformation and $u_1 = u_2 = u$ for isotropic deformation. Once the deformation reaches a stable state, it is easy to calculate the principal extension ratios λ_1 and λ_2 and the relative area change $\Delta S/S_0$.

4.2.3 Relation between spring network and continuum models

We analyze the mechanical properties of the discrete spring network model within the context of continuum models. The boundary conditions (4.11) and (4.12) imposed

on the discrete model correspond to $\lambda_1 = (L_1 + u_1)/L_1$ and $\lambda_2 = (L_2 + u_2)/L_2$. The tensions on the edges are computed as

$$\tau_1 = \frac{\sum_i F_{i,1}|_{x_1=-u_1/2}}{\lambda_2 L_2},\ \tau_2 = \frac{\sum_j F_{j,2}|_{x_2=-u_2/2}}{\lambda_1 L_1}, \tag{4.16}$$

where $F_{i,1}$ represents the x_1-component of the total spring force $\underline{F_i}$ acting on node i and $F_{j,2}$ its x_2-component. In the limit of small deformation the relation between tensions and deformation yields the values of G_s and ν_s as a function of k.

4.3 Deformation of a 2D spring sheet

We first investigate the deformation of a 2D material under uniaxial or isotropic extension. We derive analytically the Poisson ratio, Young modulus and area dilation modulus of a spring network model in the small deformation limit and we compare those parameters with their values for continuum constitutive laws. We then compare numerically the stress-strain relationship between the discrete spring network and continuum models in large deformation.

4.3.1 Analytical solution in the small deformation limit

We consider an infinitely fine spring network and derive the relation between force and deformation for a single inner mesh (i.e. far from the edges), assuming that all the mesh elements are identically deformed so that the forces acting on the nodes are symmetric. For the sake of simplicity, we only detail here the derivation of the elastic constant for a cross mesh element; the material properties can be similarly derived for other mesh types using the same procedure.

The springs numbering is shown in Figure 4.3. Spring 1 is orientated in the x_1-direction, spring 2 in the x_2-direction and spring 3 along the cross direction. The initial angle between springs 1 and 3 is θ_0. Let the initial length of springs 1, 2, and 3 be respectively l_0, w_0 and $L_0 = (l_0^2 + w_0^2)^{1/2}$.

The spring network is deformed from l_0 to $l_0 + \Delta l$ ($|\Delta l| \ll l_0$) in the x_1-direction and from w_0 to $w_0 + \Delta w$ ($|\Delta w| \ll w_0$) in the x_2-direction. We also have

$$(L_0 + \Delta L)^2 = (l_0 + \Delta l)^2 + (w_0 + \Delta w)^2, \tag{4.17}$$

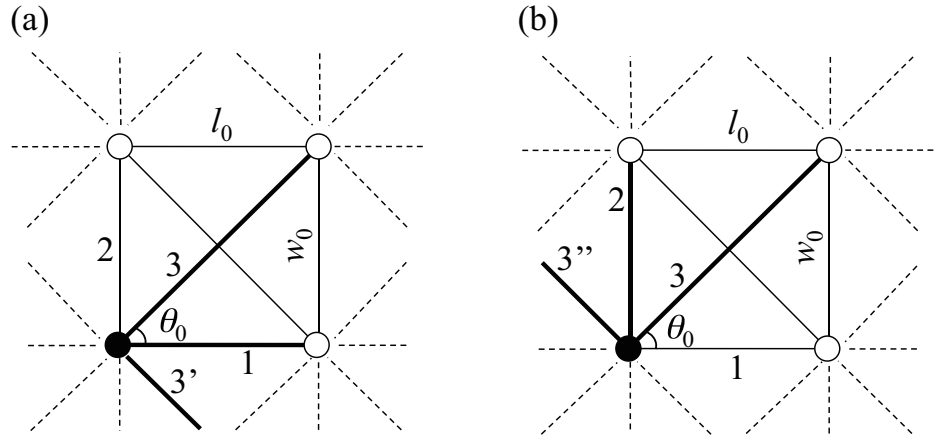

Fig. 4.3 Numbering of the springs that are taken into account to calculate the forces acting on a node for homogeneous mesh deformation: (a) springs 1, 3 and 3' contribute to the x_1-force component (b) springs 2, 3 and 3" contribute to the x_2-force component. Springs 3' and 3" are the counter part of spring 3, generated by the periodic boundary condition. The initial lengths are l_0 for spring 1 and w_0 for spring 2. The initial length of springs 3, 3' and 3" is $L_0 = \sqrt{l_0^2 + w_0^2}$. The initial angle between springs 1 and 3 is θ_0.

where ΔL is the length change of spring 3. In the small deformation limit, after neglecting the second order terms, equation (4.17) is simplified

$$\Delta L = \frac{l_0 \Delta l + w_0 \Delta w}{L_0}. \tag{4.18}$$

For homogeneous deformation, the components of total spring force F acting at the nodal point is due to springs 1, 3 and 3' in the x_1-direction and to springs 2, 3 and 3" in the x_2-direction (Figure 4.3):

$$F_1 = k\Delta l + 2k\Delta L \cos(\theta_0 + \Delta\theta), \tag{4.19}$$

$$F_2 = k\Delta w + 2k\Delta L \sin(\theta_0 + \Delta\theta), \tag{4.20}$$

where $\Delta\theta$ is the angle change. The local tensions τ_1 and τ_2 on a mesh are given by :

$$\tau_1 = \frac{F_1}{w_0 + \Delta w},\ \tau_2 = \frac{F_2}{l_0 + \Delta l}. \tag{4.21}$$

4.3.1.1 Uniaxial and isotropic deformation

The spring network is first stretched in the x_1-direction under an external tension τ_1, while $\tau_2 = 0$. The transverse displacement Δw can be deduced from equation (4.20):

$$\Delta w/\Delta l = -\frac{2l_0 \sin\theta_0}{L_0 + 2w_0 \sin\theta_0}. \tag{4.22}$$

In the small deformation limit, the Poisson ratio is thus given by

$$\nu_s = \frac{|\Delta w/w_0|}{\Delta l/l_0} = \frac{2l_0 \sin\theta_0}{L_0 + 2w_0 \sin\theta_0}\frac{l_0}{w_0}. \tag{4.23}$$

Substituting (4.22) into (4.19), we obtain the expression of F_1 as a function of Δl, from which the small deformation Young modulus follows :

$$E_s = \frac{\tau_1}{\Delta l/l_0} = \frac{L_0 + 2w_0 \sin\theta_0 + 2l_0 \cos\theta_0}{L_0 + 2w_0 \sin\theta_0}\frac{l_0}{w_0}k. \tag{4.24}$$

In another experiment, the spring network is stretched in the x_1- and x_2-directions by an isotropic tension $\tau_1 = \tau_2 = \tau$. Using equations (4.19) to (4.21), we find for small deformation

$$\frac{\Delta w}{\Delta l} = \frac{L_0 l_0 + 2l_0^2 \cos\theta_0 - 2l_0 w_0 \sin\theta_0}{L_0 w_0 + 2w_0^2 \sin\theta_0 - 2l_0 w_0 \cos\theta_0}, \tag{4.25}$$

$$\Delta S/S = \Delta w/w_0 + \Delta l/l_0. \tag{4.26}$$

The tension τ is deduced from equation (4.21)

$$\tau = 2\frac{L_0 + w_0 \sin\theta_0 + l_0 \cos\theta_0}{L_0 + w_0 \sin\theta_0 - l_0 \cos\theta_0}\frac{\Delta l}{w_0}k. \tag{4.27}$$

Thus, the area dilation modulus K_s is :

$$K_s = \frac{\tau}{\Delta S/S} = \frac{l_0 w_0 (L_0 + 2w_0 \sin\theta_0 + 2l_0 \cos\theta_0)}{L_0^3 + 2l_0^3 \cos\theta_0 + 2w_0^3 \sin\theta_0 - 2l_0 w_0 (l_0 \sin\theta_0 + w_0 \cos\theta_0)}k. \tag{4.28}$$

Table. 4.1 Relationship between the spring constant k, Young modulus E_s and Poisson ratio ν_s in the small deformation limit for a 2D material under uniaxial deformation. The material is discretized by 3 types of meshes and subjected to homogeneous deformation. The arrows indicate the directions of extension.

Mesh Type	k as a function of E_s	ν_s
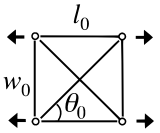	$k = \dfrac{L_0 + 2w_0 \sin\theta_0}{L_0 + 2\left(w_0 \sin\theta_0 + l_0 \cos\theta_0\right)} \dfrac{w_0}{l_0} E_s$ Isotropic mesh: $k = 2/3\ E_s$	$\nu_s = \dfrac{2l_0 \sin\theta_0}{L_0 + 2w_0 \sin\theta_0} \dfrac{l_0}{w_0}$ Isotropic mesh: $\nu_s = 1/2$
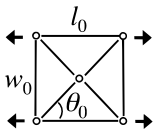	$k = \dfrac{L_0 + w_0 \sin\theta_0}{L_0 + w_0 \sin\theta_0 + l_0 \cos\theta_0} \dfrac{w_0}{l_0} E_s$ Isotropic mesh: $k = 3/4\ E_s$	$\nu_s = \dfrac{l_0 \sin\theta_0}{L_0 + w_0 \sin\theta_0} \dfrac{l_0}{w_0}$ Isotropic mesh: $\nu_s = 1/3$
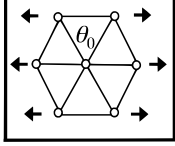	Isotropic mesh: $k = \dfrac{\sqrt{3}}{2} E_s$	Isotropic mesh: $\nu_s = 1/3$

Table. 4.2 Relationship between the spring constant k and area dilation modulus K_s in the small deformation limit for a 2D material under isotropic deformation. The material is discretized by 3 types of meshes and subjected to homogeneous deformation. The arrows indicate the directions of extension.

Mesh Type	k as a function of K_s
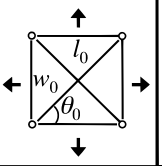	$k = \dfrac{L_0^3 + 2l_0^3 \cos\theta_0 + 2w_0^3 \sin\theta_0 - 2l_0 w_0 \left(l_0 \sin\theta_0 + w_0 \cos\theta_0\right)}{l_0 w_0 \left(L_0 + 2w_0 \sin\theta_0 + 2l_0 \cos\theta_0\right)} K_s$ Isotropic mesh: $k = 2/3\ K_s$
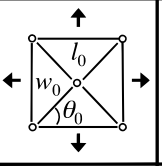	$k = \dfrac{L_0^3 + l_0^3 \cos\theta_0 + w_0^3 \sin\theta_0 - l_0 w_0 \left(l_0 \sin\theta_0 + w_0 \cos\theta_0\right)}{l_0 w_0 \left(L_0 + w_0 \sin\theta_0 + l_0 \cos\theta_0\right)} K_s$ Isotropic mesh: $k = K_s$
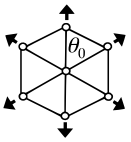	Isotropic mesh: $k = \dfrac{2}{\sqrt{3}} K_s$

4.3.1.2 Influence of mesh topology

The small deformation analytical expressions of Young modulus E_s, Poisson ratio ν_s and area dilation modulus K_s are given in Tables 4.1 and 4.2 for cross, cross-centre and regular triangle meshes undergoing homogeneous deformation. A number of conclusions can be drawn:

- A non isotropic mesh ($l_0 \neq w_0$) leads to anisotropic elastic properties for the membrane. It can be easily checked that the values of E_s and ν_s would be different from (4.23) and (4.24) if the uniaxial stretching were applied along the x_2-direction rather that the x_1-direction.
- An isotropic membrane must therefore be modelled with an isotropic mesh ($l_0 = w_0, \theta_0 = \pi/4$ for cross and cross center).
- Even for an isotropic mesh, the Poisson ratio depends on the mesh geometry as is apparent from Table 4.1. The Young modulus, and thus the shear modulus G_s, also depend on the mesh geometry and are proportional to the spring constant.

4.3.2 Effect of mesh size

To investigate the influence of the mesh-resolution in the small deformation limit, we compute numerically the ratio between the spring constant and the elastic properties for isotropic meshes with different grid-spacing, $l_0 = \Delta L$, ranging from 0.003 to 1.0. We follow the numerical method explained in section 4.2.2 and apply it to cross, cross-centre and unstructured meshes.

Figure 4.4 shows the values of k/E_s and of k/K_s as functions of mesh size, obtained for the three networks. It is clear that the geometry and size of the mesh have an influence on the results. This is due to the fact that when the mesh is coarse, the hypothesis of a homogenous deformation of the individual meshes becomes wrong (a direct consequence of the Saint-Venant principle). There is then a significant influence of the boundary conditions at the sample edges.

For cross and cross-centre settings, as the mesh is refined, the values of k/E_s and of k/K_s converge towards the analytical values for homogeneous isotropic meshes

given in Tables 4.1 and 4.2. The deviation from the analytical value is less than 1 % when $\Delta L < 0.025$. The Poisson ratio, inferred from k/E_s and of k/K_s, is also in good agreement with the analytical values. The case $\Delta L = 1$ corresponds to a single mesh. For a cross and cross-centre mesh, k/E_s is then equal to 0.375 and 0.417, respectively. These values are obtained by following the method of section 4.3.1 and applying non-symmetric boundary condition.

Mesh convergence is also found for the unstructured mesh. For $\Delta L = 0.005$, the maximum relative variation for k/E_s or k/K_s is less than 0.1%. However, the converged values of k/E_s and of k/K_s for the unstructured mesh are smaller than the analytical solution for the regular triangle. Both meshes would still be expected to behave similarly, as they are both constructed with triangle meshes, each node being connected to six springs. The difference in the spring constant between the regular triangle and unstructured meshes is therefore likely to be due to the random departure from exact isotropy of the unstructured mesh. The Poisson ratio, however, is equal to 1/3 as predicted for the regular triangular mesh. Similar results have been reached by Hansen et al. [36] who showed that the detailed geometry of an unstructured triangular mesh had an influence on the bulk elastic properties of the sheet.

4.3.3 Comparison of spring network and continuum models

We compare the small deformation mechanical properties of spring network models with an isotropic mesh and the constitutive laws NH and SK. Recall that the Poisson ratio of a spring network is determined by the mesh configuration and is independent of k. For the homogeneous square cross mesh, the Poisson ratio ($\nu_s = 1/2$) is equal to that of a SK ($C = 1$) or NH membrane according to equations (4.7) and (4.9). If the spring constant is further set to $k/G_s = 2$, the small deformation mechanical properties E_s, G_s and K_s of the square cross mesh model are identical to those of a NH or of SK ($C = 1$) membrane. In the case of the square cross-centre mesh and the regular triangle mesh with periodic boundary conditions, the Poisson ratio is 1/3, which corresponds to the Poisson ratio of a SK law with $C = 1/2$. By adjusting $k/G_s = 2$ for the cross-centre mesh and $k/G_s = 4/\sqrt{3}$ for the regular-triangle mesh, the mechanical properties of the spring network models coincides with these of a SK

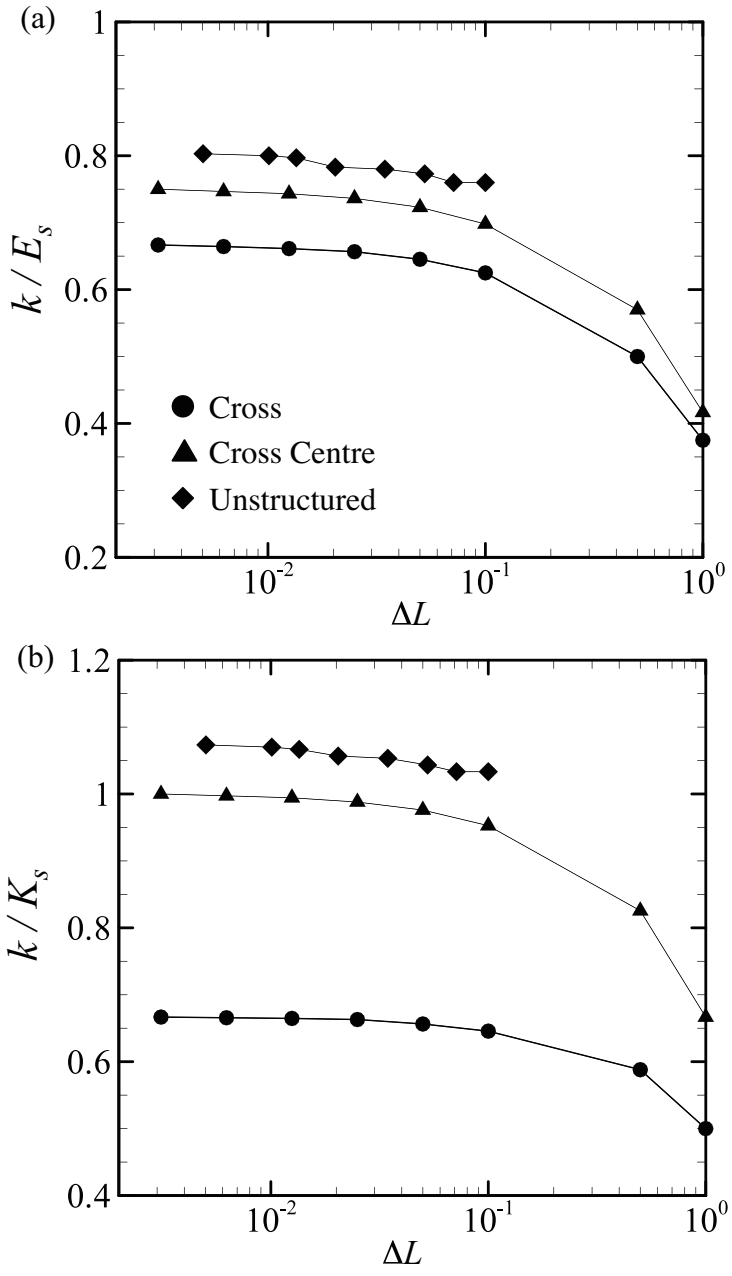

Fig. 4.4 Spring constants as a function of initial grid spacing for several mesh types under (a) uniaxial extension and (b) isotropic extension. A single mesh corresponds to $\Delta L = 1$.When the mesh is refined, the spring constant converges to the analytical value for an homogeneous network.

($C = 1/2$) law. It is not possible to match the mechanical properties of a square cross-centre model with those of a NH membrane.

4.3.4 Large deformation

We now compare numerically the tension-strain relationships of a spring network discretized with square cross, cross-centre and unstructured meshes and a continuum model under *large* uniaxial and isotropic deformation. In all the cases, we use a small enough mesh to ensure a constant ratio between k and G_s ($\Delta L = 0.003$ for the cross and cross-centre mesh and $\Delta L = 0.005$ for the unstructured mesh).

The tension-strain relationships are shown in Figure 4.5(a) for several membrane models under large uniaxial elongation. We note that SK law is strain-hardening while NH law is strain-softening, as mentioned earlier. The cross mesh model exhibits a strain-hardening behaviour similar to SK law. However, the cross-centre and unstructured meshes have a quasi-linear tension-strain relationship, similar to Hooke's law, even for large deformation.

The isotropic tension-area dilation relations are shown in Figure 4.5(b). All three spring network models are strain-softening. This can be explained by considering the isotropic deformation of a regular triangle with initial length l_0. The initial surface area is $S_0 = \sqrt{3}l_0^2/4$. When all the springs are equally elongated from l_0 to $l_0 + \Delta l$, the deformed surface area is $S = \sqrt{3}(l_0 + \Delta l)^2/4$ and the relative area change is

$$\frac{\Delta S}{S_0} = \frac{S - S_0}{S_0} = \frac{2l_0\Delta l + \Delta l^2}{l_0^2}. \tag{4.29}$$

As the spring force is given by $f = k\Delta l$, the relative area change becomes

$$\frac{\Delta S}{S_0} = \frac{f^2 + 2l_0kf}{l_0^2k^2}. \tag{4.30}$$

This equation shows that the relationship between relative area change and spring force is quadratic, yielding a strain-softening behaviour. In a similar manner, the same strain-softening behaviour can be predicted for square-mesh cases.

When modeling biological cell membranes, such as a red-blood-cell membrane, local area dilation resistance has to be enforced. In the spring network model, the

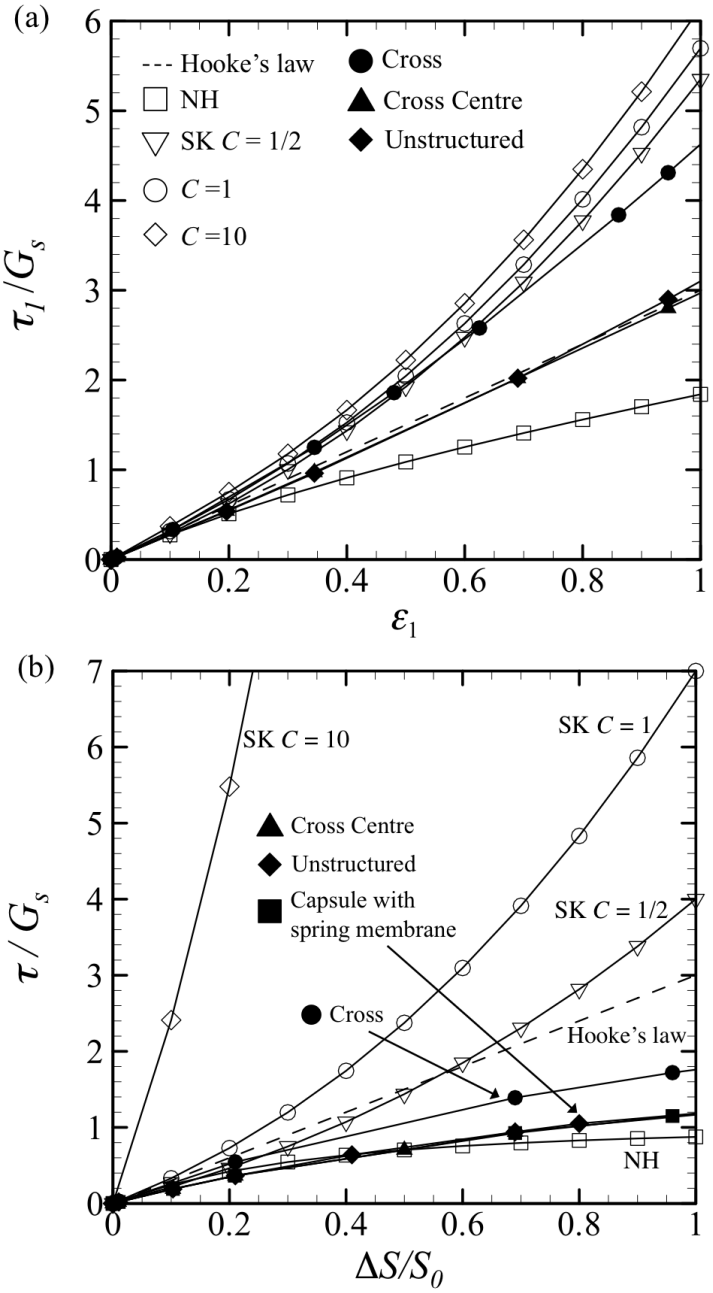

Fig. 4.5 Tension-strain relationship under (a) uniaxial elongation and (b) isotropic dilation for continuum and spring models

membrane always shows a strain-softening behavior and imposing the local area incompressibility is impossible. Thus a simple spring model does not seem appropriate to simulate the behavior of an area incompressible biological cell membrane.

4.4 Inflation of a capsule

When a spherical capsule is inflated by a radial pressure difference between the inside and outside of the membrane, its membrane is under in-plane traction. In this section, we are interested in checking whether the curved surface of the capsule influences the conclusions found for a flat 2D membrane in the previous section.

It has been observed earlier that the grid of the spring network model must be isotropic in order to reproduce isotropic material properties. It is, however, impossible to generate an isotropic mesh on a spherical surface such as the membrane of a capsule. The most regular mesh that may be generated for a sphere is a regular icosahedron. The triangles of the icosahedron are successively divided into four triangles and the new nodes are projected onto the sphere at each step. The process is repeated until the desired mesh size is obtained. In this section, the capsule membrane is discretized with 1280 triangle elements.

We set as boundary condition a uniform stretched radius $\ell = \ell_0 + \Delta\ell$, where ℓ_0 is the initial radius of the capsule and $\Delta\ell$ is the radius change. The positions of all the nodal points are therefore fixed. For the continuous-membrane model, the tension τ in the membrane can be calculated by the Laplace equation $\tau = \ell\Delta p/2$, where Δp is the pressure jump between the inner and outer sides of the membrane. In the case of the discrete spring model, we assume the equilibrium between the average pressure jump across the membrane and the component of the spring force normal to the membrane. We thus define the tension τ as

$$\tau = -\frac{\ell^{ave}}{2S}\sum_i \underline{F}_i \cdot \underline{n}_i, \tag{4.31}$$

where ℓ^{ave} is the average radius of the capsule and $\underline{n}_i$ is the outward normal unit vector to the surface at node i. The surface area S of the discrete spring model is calculated by summing the surface areas of all the triangles.

The spring constant of the capsule membrane is adjusted, so that it coincides,

in the small deformation limit, with the value of K_s/G_s of the SK law with $C = 1/2$. The tension-strain curve can be perfectly superimposed onto the results found under 2D isotropic deformation with the cross-center and unstructured meshes. Mesh refinement has not been seen to have an effect on the results, indicating that the mesh convergence is reached. From these results, we conclude that, for isotropic extensions, previous findings on the mechanical properties of flat 2D spring sheet can be applied to curved surface membranes and therefore to the study of capsule inflation.

4.5 Capsule in simple shear flow

We now consider the capsule is freely suspended in a Newtonian fluid with the same viscosity μ and density as the internal Newtonian fluid. With respect to axes centered on the capsule center, the undisturbed flow velocity field $\underline{v}^\infty$ of the external fluid is given by

$$v_1^\infty = \dot{\gamma} x_2,\ v_2^\infty = v_3^\infty = 0, \tag{4.32}$$

where $\dot{\gamma}$ is the shear rate of the external fluid.

For the spring network model, Ca is calculated assuming $k/G_s = 4/\sqrt{3}$, as discussed in the previous section 4.3.3. In order to cover a wide range of physical situations, we vary Ca from 0 to 3.5 and use either NH or SK law for the continuum model. We then discuss the difference between spring network and continuum constitutive laws.

4.5.1 Membrane mechanics with spring network

Owing to the small dimensions of the particle, the particle Reynolds number is very small and the Stokes equations apply for both the internal and external fluid motion. Then, the velocity field $\underline{v}$ at any point $\underline{x}$ is given by the integral equation, which is described in the chapter 2. When we solve the membrane equation with a spring network model, the spring forces are calculated by equation (4.10). The load $\underline{q}$ in equation (2.27) is computed at each node i:

$$\underline{q}_i = \frac{1}{dA_i} \sum_k \underline{f}_{i,k}, \tag{4.33}$$

where the summation is done on all the adjacent nodes and dA_i is the surface area calculated as follows. Let point g_j be the centre of gravity of the element e_j, which is

surrounding point i. dA_i is calculated by summing up triangles $da_{j,j+1}$ made by the points i, g_j, g_{j+1}

$$dA_i = \sum_{j}^{n_i} da_{j,j+1}, \tag{4.34}$$

where n_i is the number of elements connected to node i.

4.5.2 Numerical method

Equation (2.27) is solved with a boundary-element method following the method by Lac et al. [46, 47]. A structured quadrilateral grid based on spherical coordinates is used and the different quantities are interpolated with bi-cubic B-spline functions. The presence of poles connected to multiple nodes leads to a singularity for the solid mechanics problem, which is then solved on an unstructured triangular mesh. We therefore use an interpolation scheme to transfer the physical quantities between the triangular mesh used for the solid problem (Figure 4.6b) and the quadrilateral mesh used in fluid problem (Figure 4.6a). In this study, we use a first-order interpolation. Any quantity of the quadrilateral mesh can be projected onto the triangular mesh. Let point i be in the triangle defined by the nodes i_1, i_2, i_3 (Figure 4.6c). A function f at point i takes the value $f(i) = A_{23}f(i_1) + A_{31}f(i_2) + A_{12}f(i_3)$, where $A_{\alpha\beta}$ is the ratio of the triangle surface area made by points i, i_α and i_β to the triangle surface area made by points i_1, i_2 and i_3. In a similar manner, physical quantities on the triangular mesh can be interpolated using those on the quadrilateral mesh.

At any given time t, we know the displacement of the membrane, so that the load $\underline{q}$ on the membrane can be calculated. The integral equation yields the new velocity field and the membrane positions are updated using an explicit fourth-order Runge-Kutta method.

The non-dimensional time step $\dot{\gamma}\Delta t$ is set at 0.005 and the procedure is stopped when the dimensionless time $\dot{\gamma}t$ is equal to 20, which is larger than twice the time needed for the deformation of the capsule to reach the steady state.

The steady state three-dimensional deformation of the capsule can be measured

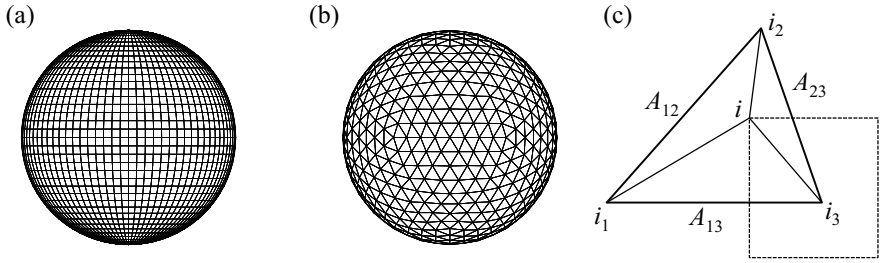

Fig. 4.6 (a) Quadrilateral mesh used in fluid solver and (b) triangular mesh used in solid solver. (c) To transfer physical quantities between the two, we use a first order interpolation. Example of a nodal point i of the quadrilateral mesh that is projected onto the triangular mesh.

using the Taylor parameter

$$D_{ij}^{\infty} = \frac{|\Lambda_i - \Lambda_j|}{\Lambda_i + \Lambda_j}, \quad \text{for } i, j = 1, 2, 3, \tag{4.35}$$

where Λ_1, Λ_2, and Λ_3 denote the three semi-axis lengths of the ellipsoid of inertia of the deformed capsule, used to estimate the capsule deformation [73].

The mesh convergence is verified by changing the mesh size. We have considered a discretization of the membrane with 1280 triangle elements for the solid solver and 3200 quadrilateral elements for the fluid solver as well as a refined mesh with 5120 triangular and 5000 quadrilateral elements. The maximum change in the Taylor parameter between the two cases is less than 1%. Since the Taylor parameter has converged for the mesh with 1280 triangular and 3200 quadrilateral elements, we will consider these mesh elements for the capsule with spring network membrane.

4.5.3 Deformation of a capsule in shear flow

Figure 4.7 shows the Taylor parameter as a function of Ca for capsules with NH and SK membrane (Lac et al. results [46]), as well as with a spring network membrane. For a capsule subjected to strong flow (large Ca), the deformation of a capsule enclosed by a spring network is larger than that of a capsule enclosed with a SK $C = 1/2$ membrane, although the two membranes have the same mechanical properties in the small deformation limit. This is due to the fact that the spring network is strain-

softening under large deformation, whereas the SK $C = 1/2$ membrane is strain-hardening.

However, since the bending rigidity of the membrane has been neglected, the membrane is mechanically stable only if it is under tension everywhere. The study of the sign of the principal tension τ in the membrane provides a way to evaluate the stability of the equilibrium state which is computed : if the minimum value τ_{min} is negative, the membrane is under compression somewhere on its surface and the equilibrium is unstable. Lac et al. [46] and Walter et al. [87] find that the membrane is under tension and thus mechanically stable for a limited range of capillary numbers where $\tau_{min} > 0$. We denote Ca_L and Ca_H the two critical capillary numbers defined by $\tau_{min}(Ca_L) = \tau_{min}(Ca_H) = 0, Ca_L \leq Ca_H$. When $Ca < Ca_L$, the initially spherical capsule is extended by the flow in the principal straining direction (oriented at $\pi/4$ with respect to the streamlines). The capsule being a closed shape with a constant volume, it is thus compressed along the equator and tends to buckle in this area. When $Ca > Ca_H$, the compression zone appears near the tip of the capsule and is due to the high curvature of this region.

We also observe low-shear (in the equator area) and high-shear (near the tips) oscillations of the normal load using a spring network as shown in figure 4.8. Such oscillations indicate a tendency towards buckling. As it is impossible to compute principal tensions in the case of a discrete spring network model, we have determined limits Ca'_L and Ca'_H on the basis of the sign of the normal component of surface load by means of the conditions $\underline{q}(Ca'_L) \cdot \underline{n} = \underline{q}(Ca'_H) \cdot \underline{n} = 0$, $Ca'_L \leq Ca'_H$. This condition is less stringent that the one on the negative principal tensions, as the membrane may be under compression but not oscillate because of numerical stiffness. As a result we find :

$$Ca'_L = 0.3,\ Ca'_H = 1.0,$$

whereas Lac et al. [46] find a smaller range of stability for a Sk law with $C = 0.5$.

$$Ca'_L = 0.8,\ Ca'_H = 1.2,$$

Although the two criteria are different, they provide a stability range which is roughly of the same order of magnitude.

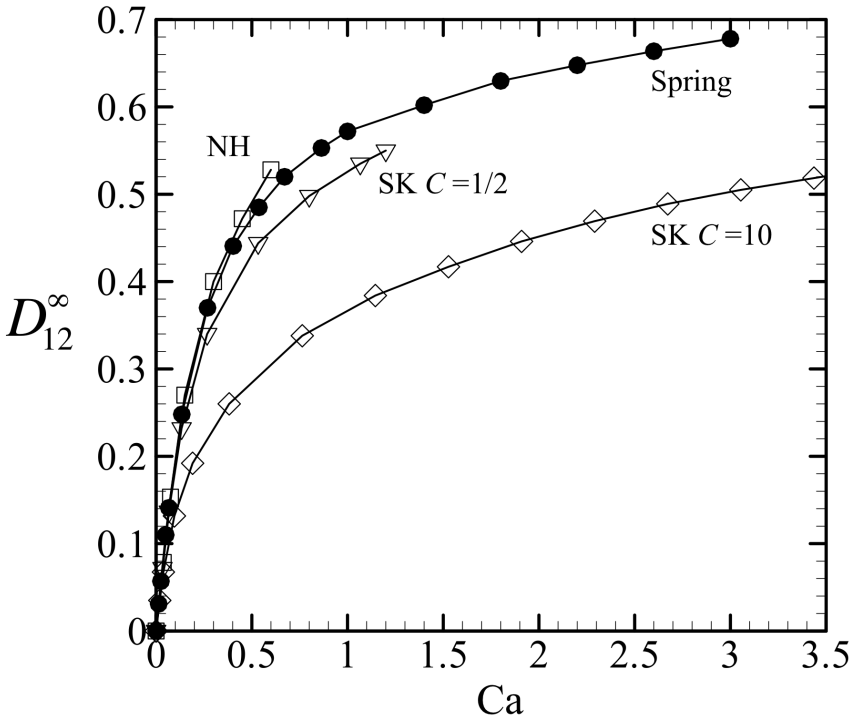

Fig. 4.7 Evolution of the Taylor deformation in the shear plane, with the capillary number Ca for capsules with NH, SK and spring network membranes.

The occurrence of negative principal tensions with a continuum membrane model or of normal load oscillations with a spring network, all denote that the membrane is undergoing compression and thus might buckle. This phenomenon is controlled by the bending resistance of the membrane. Here, we have not included any bending stiffness in the membrane model and as a consequence, we cannot model the actual buckling. However, the membrane has some numerical stiffness that prevents it from collapsing and allows us to compute the motion of a capsule even when compression occurs. Since, the aim of this study is to compare the discrete spring network model and 2D in-plane constitutive laws, we do not discuss any further the effect of the bending stiffness on the deformation of the capsule in this study.

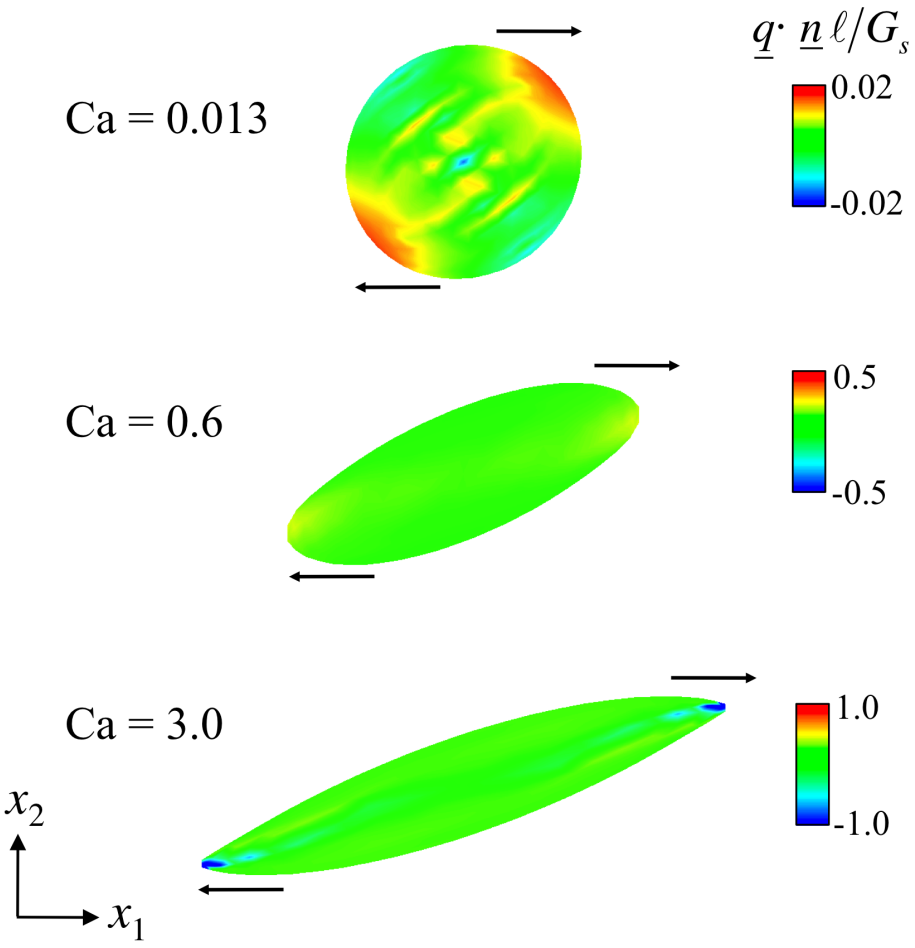

Fig. 4.8 (Color) Deformation of the capsule with a spring network model under $Ca = 0.013, 0.6, 3.0$. The background shear is applied in the $x_1 - x_2$ plane, where x_1 is taken in the flow direction. The color scale represents the normal component of the load.

4.5.4 Comparison with former experimental studies

Deformation of an artificial capsule in a simple shear flow was investigated experimentally [15, 86]. In the work of Chang et al.[15], the capsule had a nylon membrane, was filled with a silicon oil and was suspended in polybutene. The viscosity ratio of the internal to external liquids λ was about 0.004. In the work of Walter et al. [86] the capsule membrane was made from polyamid (4-Aminomethyl-1,8-diaminooctane) and the viscosity ratio λ was 0.001. In order to have similar λ values with the experiments, λ is set as 0.002 in the numerical simulations. In those two experimental

studies, the membrane Young modulus E_s was measured. To compare the experimental and numerical results, a capillary number Ca_{E_s} is defined based on the Young modulus as $Ca_{E_s} = CaG_s/E_s$.

The Taylor parameter is shown as a function of capillary number in figure 4.9. The behaviour of SK $C = 1$ is similar to nylon capsule (indicated as "Chang et al." in figure 4.9) in wide range of capillary numbers. In the case of polyamid capsule ("Walter et al." in the figure), the Taylor parameter has higher values than those of the nylon capsule. By employing proper continuum model with an appropriate model parameter, experimental results can be well captured. In the case of the simple spring model, it is difficult to express various experimental results by adjusting the spring constant. Thus, continuum models have broader applicability to actual experimental situations.

4.6 Conclusions

In this chapter, we have compared the mechanical properties of a membrane modeled with continuum constitutive laws and a discrete spring network under various conditions: uniaxial and isotropic deformations of a 2D membrane, inflation of a capsule and deformation of an initially spherical capsule in a simple shear flow. The results have shown that the mechanical properties of spring networks are strongly dependent on the mesh configuration.

In the small deformation limit, the mechanical properties of the spring network model may be predicted analytically. It is found that, the spring network model has anisotropic mechanical properties in general. However isotropic meshes have mechanical properties that converge towards those of an isotropic material. To express isotropic elasticity using a spring network model, the mesh must therefore be isotropic and sufficiently fine, relative to the variation of the stress field. Moreover, in the small deformation limit, we observe that the behaviour of the spring network with a fine square cross mesh is similar to NH and SK $C = 1$, ($E_s = 3.0G_s$, $\nu_s = 1/2$), by adjusting $k/G_s = 2.0$. Square cross-centre and regular-triangle meshes are similar to SK $C = 1/2$ ($E_s = 8/3G_s$, $\nu_s = 1/3$), by adjusting $k/G_s = 2.0$ and $k/G_s = 4/\sqrt{3}$, respectively. These correlations are important, because one can determine the spring

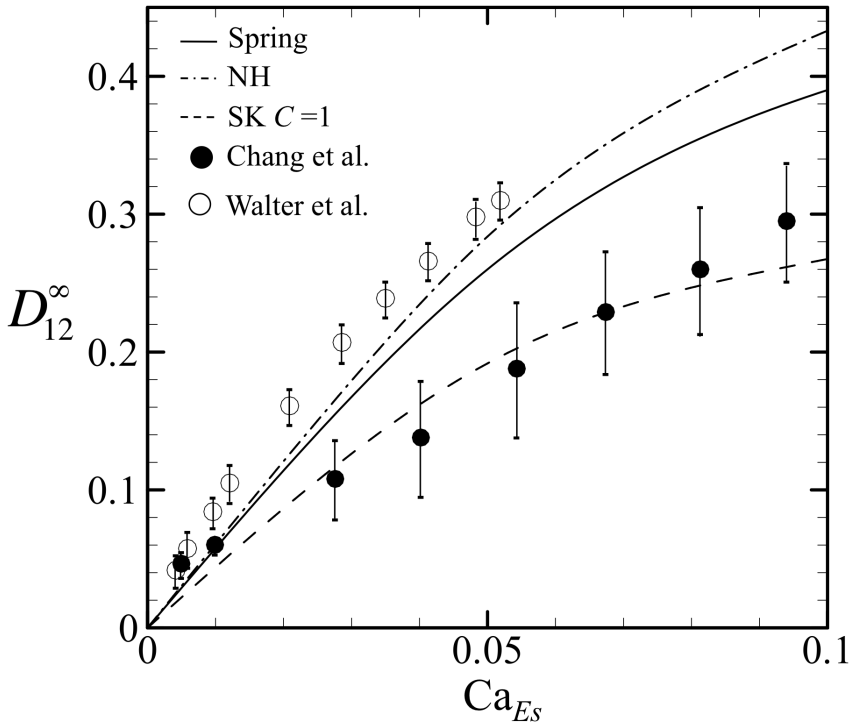

Fig. 4.9 Taylor parameter as a function of capillary number Ca_{E_s}. Ca_{E_s} is defined by using Young modulus instead of shear modulus. Viscosity ratio between internal and external liquids is set as $\lambda = 0.002$ in the numerical models, whereas $\lambda \approx 0.004$ and 0.001 in the paper of Chang et al. and Walter et al., respectively. (Note; the error bars for the two experimental results do not represent standard deviations but the maximum and minimum values in the experiments.)

constant by performing conventional mechanical experiments.

In large deformation, the stress-strain relationship under isotropic elongation shows a strain-softening behaviour for all mesh types, and it is difficult to express the area-incompressible property. For a capsule in a simple shear flow, we also confirm that a spring network cannot express the $D_{12}^{\infty} - Ca$ correlation of a capsule with an area-incompressible membrane. Thus, to express a biological cell membrane, we need to choose a membrane model that can express the local area incompressibility, such as the SK law, instead of a spring network model.

Chapter 5

Single RBC in shear flow

5.1 Introduction

Flow-induced deformation of RBCs affects the cell ability to release various molecules and regulate their concentration in blood [34]. In particular, when RBCs are strongly deformed by the surrounding fluid flow, they release ATP and ADP [3, 89]. ATP is a well-known energy source for intracellular functions, and extracellular ATP plays an important role as a signaling molecule in a variety of physiological processes [89]. In addition, ADP is known to be a factor in the primary aggregation of platelets [3]. Flow-induced deformation may also lead to RBC rupture, called hemolysis. There is no doubt that some causal relation between the stress level in the membrane and hemolysis exists. Thus, clarification of the stresses in the membrane is crucial towards understanding the physiology and pathology of microcirculation. As the membrane is very thin, we can consider only the deformation of its median surface. Furthermore, the stresses can be integrated across the thickness and be replaced by tensions.

A number of studies have investigated the motion of a single RBC in a shear flow analytically [79] and numerically [48, 70, 73]. Skotheim & Secomb [79] analytically investigated the motion of an RBC in shear flow. In their study, the RBC was modelled as a two dimensional biconcave disk and its deformation was omitted. They showed that the RBC rotates like a solid particle at low flow strength, which is called as tumbling motion. At high flow strength, on the other hand, the membrane rotates around the cell shape with constant inclination angle, called as tank-treading motion.

They also reported the tumbling-to-tank-treading transition occurred in moderate shear rate with various viscosity ratio of internal and external liquids. Ramanujan & Pozrikidis [73] first reported a 3D computation of the RBC in a simple shear flow. The RBC was modelled as a capsule with a hyper-elastic membrane and its reference shape was assumed as a biconcave disk. The non-spherical reference shape leads anisotropic membrane properties, yields a periodic shape oscillation during the tank-treading motion. In their study, however, the computation was unstable to achieve enough long computational time, because of some numerical instabilities, and only few results were discussed in the paper. Le et al. [48] also compared the motion and deformation of a biconcave disk with those of an oblate capsule in a simple shear flow using an immersed boundary method, though only few results with non-identical viscosity ratio were reported. Thus, in order to fully understand the kinematics of an RBC, further analysis with various viscosity ratio and shear rate conditions are needed.

In physiological conditions, resting shape of an RBC is a biconcave disk, which is strongly anisotropic and orientation of the RBC must be concerned when it is subjected to shear flow. About a century ago, Jeffery analytically derived the motion of a non-Brownian ellipsoid particle with arbitrary orientation in creeping linear background flow [41]. Since then, Jeffery's theory has been used to describe the alignment of rods and ellipsoids, such as carbon nanotubes [37], liquid crystal [63], bacteria [42], and platelets [62]. The theory states that the trajectory of a non-Brownian rigid ellipsoid in Stokes flow is invariant under time reversal and that reorientation over long time duration does not occur under simple shear flow conditions. The time reversibility can be destroyed by introducing inertia effects [94] or visco-elastic properties of the surrounding fluid [40], because the motion is no longer independent of time in these cases. However, the effect of particle deformability on the time reversibility is not well clarified. Many capsules in realistic situations are not perfect spheres because of the inhomogeneity of the membrane properties or folding due to unbalanced osmotic pressure. If one places a non-spherical capsule in creeping shear flow, how does the orientation change relative to the flow field over long time duration? Jeffery speculated that an ellipsoid may alter its orientation so that the viscous energy dissipation

of the system becomes minimal [41]. However, this may not be true for a capsule with large deformation. Although many former experimental and numerical studies [1, 5, 29, 73, 88] have examined the dynamics of a non-spherical capsule in shear flow, as well as the RBC type biconcave disk, none of them can answer this question.

Moreover, no study has thoroughly examined the elastic tensions of the membrane despite their relevance to understand the RBC physiology and pathologies. Pozrikidis [70] only investigated the tension on the RBC membrane in the tumbling regimes using a boundary element method: he found that compressive tensions appear on the membrane during tumbling. In his study, however, the large deformation of the RBC was not considered. To the best of our knowledge, all other former studies only discussed the kinematics and shape of RBCs.

Not only dynamics of the RBC itself but macroscopic rheological properties of the RBC suspension are also important. It is well known that blood is a dense suspension of RBCs and its macroscopic rheological properties strongly depend on the microscopic behaviour of RBCs in a solvent fluid. To determine the relation between the macroscopic rheological properties of a suspension and its microscopic behaviour of small particles, Batchelor [10] analytically introduced the stress system in a suspension of force-free particles. Which is called as stresslet or particle stress tensor and Pozrikidis and his coworker [68, 73] applied it to capsule suspensions to show the effective stress tensor for a dilute suspension of spherical capsules. Although many researchers have investigated the dynamics of the concentrated suspension of capsules, as well as RBCs, in tubes or rectangular channels numerically and experimentally [4, 30, 72, 96], none of them clarified the detailed stress system, i.e. particle stress tensor, of the RBC suspension, because these former studies only discussed the macroscopic rheological properties with apparent viscosity or velocity profiles of the RBC suspension.

In this chapter, we investigate the kinematics and rheology of a single RBC in creeping shear flow and results are applied to rheological properties of a dilute suspension of RBCs in shear flow. In section 5.3.1, we compute the kinematics of the RBC subjected to different capillary number Ca and viscosity ratio λ to investigate the phase transition of tumbling to swinging motion. In section 5.3.2, we investigate

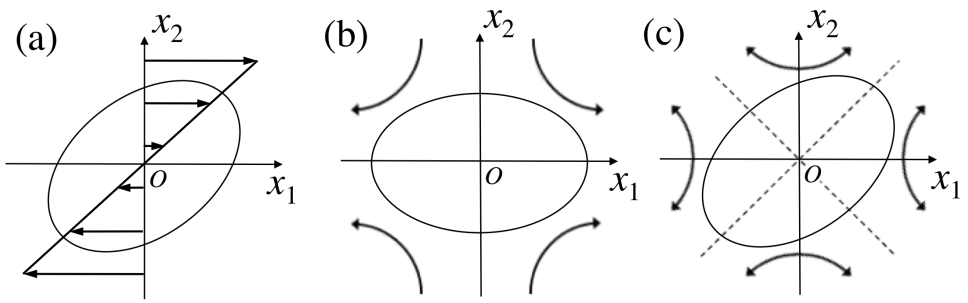

Fig. 5.1 Schematic illustration of a capsule in (a) simple shear flow, (b) steady planar elongational flow and (c) oscillatory planar elongational flow.

reorientation phenomena of a spheroidal capsule and RBC. Next, we investigate the deformation and membrane tension of the RBC with various Ca and λ condition and discuss the rheological properties of a dilute suspension of RBCs. Finally, we conclude this chapter in section 5.5.

5.2 Problem statement

An RBC is modeled as a capsule with a hyper-elastic membrane with surface shear elastic modulus G_s and area dilation modulus K_s. The SK law with $C = 10$ is employed for the membrane to express the area incompressibility of the RBC membrane. The finite element method is used to solve the membrane mechanics. We assume that an RBC is filled with an incompressible Newtonian fluid with density ρ and viscosity $\lambda\mu$ and freely suspended in another Newtonian fluid with the same density ρ but viscosity μ. Due to the small scale of the RBC, we also assume that flow is a Stokesian, i.e. inertia free, and the flow is solved by the boundary element method. Throughout this chapter, we use a linear element with 1280 or 5120 meshes for the membrane.

In a Cartesian reference frame with the RBC center as origin, the undisturbed velocity field $\underline{v}^{\infty}(\underline{x})$ is given by

$$\underline{v}^{\infty}(\underline{x}) = \left(\underline{\underline{e}} + \underline{\underline{\Omega}}\right) \cdot \underline{x}, \tag{5.1}$$

where $\underline{\underline{e}}$ and $\underline{\underline{\Omega}}$ are the rate of strain and rotation tensor, respectively. In this chapter, we use three types of background flow: (a) a simple shear flow given by $e_{12} = e_{21} =$

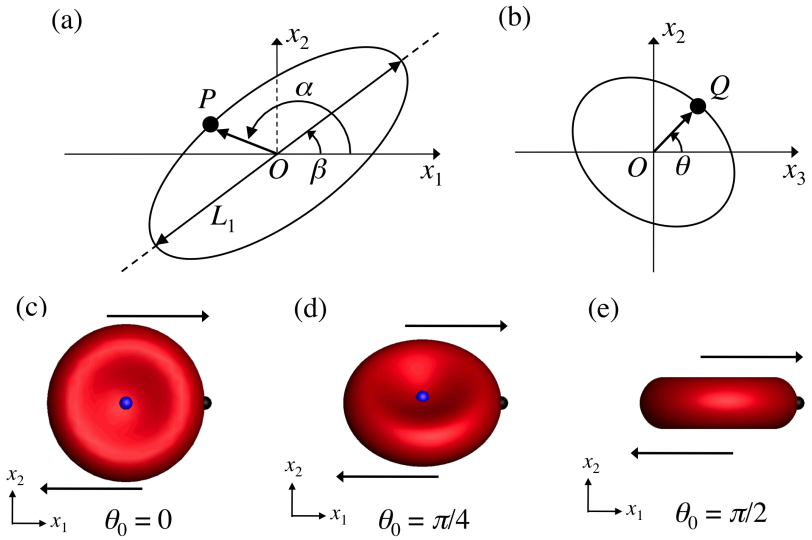

Fig. 5.2 Orientation of an RBC: (a) Angle $\alpha(t)$ is defined as the angle between the unit vector pointing to a material point on the membrane P and the x_1-axis. $\beta(t)$ is the inclination angle of the capsule. (b) Angle $\theta(t)$ is defined as the angle between the the unit vector pointing to a material point on the membrane Q and the x_3-axis. The material points P and Q are initially located on the x_1-axis with $x_1 > 0$ and the revolution axis of the spheroid ellipsoidal capsule or the biconcave disk, respectively. Initial orientation of the RBC with (c)$\theta_0 = 0$, (d) $\theta_0 = \pi/4$ and (e) $\theta_0 = \pi/2$ in the (x_1, x_2)-plane. Arrows in figures (c), (d) and (e), for instance, indicate the flow direction of a simple shear flow. Black and blue dots represent the material points P and Q, respectively.

$\Omega_{12} = -\Omega_{21} = \dot{\gamma}/2$ (all the other components = 0), as shown in figure 5.1(a); (b) a steady planar elongational flow given by $e_{11} = -e_{22} = \dot{\gamma}$ (all the other components = 0), as shown in figure 5.1(b); (c) an oscillatory planar elongational flow given by $e_{12} = e_{21} = \frac{\dot{\gamma}}{2}\cos\omega t$ (all the other components = 0), as shown in figure 5.1(c). Here, $\dot{\gamma}$ is the shear rate or the elongational rate, t is the time and ω is the angular velocity of the flow, which is correlated to the oscillation period T as $\omega = 2\pi/T$. The capillary number is given by $Ca = \mu\ell\dot{\gamma}/G_s$, where ℓ is the radius of a sphere which has the same volume as the ellipsoid or the biconcave disk.

To determine the RBC orientation efficiently, we define three different angles. Material points P and Q are initially located on the x_1-axis with $x_1 > 0$ and the revolution axis of the spheroid ellipsoidal capsule or the biconcave disk, respectively. Angle $\alpha(t)$ is defined as the angle between the unit vector pointing to the material point on the

membrane P and the x_1-axis and $\beta(t)$ is the inclination angle of the RBC (cf. figure 5.2(a)). Angle $\theta(t)$ is defined as the angle between the the unit vector pointing to the material point on the membrane Q and the x_3-axis (cf. figure 5.2(b)). In this study, the initial angle θ_0 is set to $\theta_0 = 0, \pi/4$, or $\pi/2$, as shown in figure 5.2(c), (d) and (e), respectively. The angle $\alpha(t)$ and $\beta(t)$ are also initially set to $\alpha(0) = \beta(0) = 0$ in all cases. To calculate the deformation of the RBC, we also define the semi-axis length L_1 and L_2 as the major and minor lengths of the deformed RBC in the shear plane (e.g. the length L_1 is shown in figure 5.2(a)), and L_3 as the semi-axis length towards the x_3-direction.

Consider now rheological properties of a dilute suspension of RBCs. To identify the relation between the macroscopic viscous stress tensor of the particle suspension and the microscopic particle behaviour, Batchelor [10] analytically derived the stress system of the suspension:

$$\underline{\underline{\sigma}} = -p\underline{\underline{I}} + 2\mu\underline{\underline{e}} + \underline{\underline{\Sigma}}^{(p)}, \tag{5.2}$$

where $\underline{\underline{\sigma}}$ is the viscous stress tensor of the suspension, p is the pressure, μ is the viscosity of a solvent, $\underline{\underline{e}}$ is the rate of strain, respectively. Here, $\underline{\underline{\Sigma}}^{(p)}$ is the particle stress tensor, which is defined as

$$\underline{\underline{\Sigma}}^{(p)} = \frac{1}{V}\sum_{i=1}^{N_c} \underline{\underline{S_i}}, \tag{5.3}$$

where V is the domain volume, N_c is the number of particles within V, and $\underline{\underline{S_i}}$ is the stresslet generated by i-th particle. Pozrikidis [68] analytically introduced the effective stresslet of a capsule $\underline{\underline{S_i}}$:

$$\underline{\underline{S_i}} = \int_{A_i} \{\frac{1}{2}(\underline{q}\underline{x} + \underline{x}\underline{q}) - \mu(1-\lambda)(\underline{v}\underline{n} + \underline{n}\underline{v})\} dA_i, \tag{5.4}$$

where $\underline{q}$ is the viscous load on the membrane, $\underline{v}$ is the velocity and $\underline{n}$ is the unit outward normal vector to the surface A_i. The summation in (5.3) over a large number of capsules in the volume V is equivalent to N_c times an average of the stresslet over all configurations of the surrounding capsules, it may be given by the form:

$$\underline{\underline{\Sigma}}^{(p)} = n\langle \underline{\underline{S}} \rangle. \tag{5.5}$$

Here, the bracket representation $\langle f \rangle$ indicates that the ensemble average of f_i and $n(= N_c/V)$ is the number density of capsules, which correlates to the volume fraction of the capsules ϕ as $\phi = \frac{4}{3}\pi\ell^3 n$. In the case of a suspension which is so dilute ($\phi \ll 1$) that the fluid motion near one capsule is independent of the presence of the other capsule, it is a simple matter to determine the force dipole strength $\langle \underline{\underline{S}} \rangle$. Using a leading approximation to the particle stress tensor for a dilute suspension of capsules, equation (5.5) may be written by the stresslet of the solitary case [11, 73]:

$$\underline{\underline{\Sigma}}^{(p)} \approx \left(\frac{3}{4\pi\ell^3} \underline{\underline{S}}^{sol} \right) \phi + O(\phi^2). \tag{5.6}$$

In section 5.4.3, we investigate the effective coefficient of the particle stress tensor, which has the order ϕ, using the first term in the right hand side of (5.6).

5.3 Kinematics of an RBC in creeping shear flow

In this section, we investigate the kinematics of an RBC in shear flow. First, tumbling and swinging motion of the RBC in simple shear flow are shown and discuss the tumbling-swinging transition phenomena. Next, we investigate reorientation of an oblate spheroidal capsule, as well as the RBC, in creeping shear flow.

5.3.1 Tumbling, swinging, and transition

Profiles of the deformed RBC in shear plane during a half time period in steady state with $Ca = 0.002$, 0.06 and 3.0 are shown in figure 5.3. For all cases, the viscosity ratio λ equals to 1 and the initial angle of θ is $\theta_0 = \pi/2$. In very low capillary number regime ($Ca = 0.002$, figure 5.3(a)), external fluid stress cannot overcome the elastic energy barrier of the membrane, so that the RBC rotates like a quasi-rigid body, which is called as tumbling motion. In high capillary number regime ($Ca = 3.0$, figure 5.3(c)), on the other hand, the membrane is elongated towards the flow direction and shows tank-treading motion. During the tank-treading motion, the shape of deformed RBC oscillates periodically, due to the anisotropic properties of the reference shape of the membrane. This type of cell oscillation is called as swinging motion, which was also found in former experimental [1] and numerical studies [48, 73, 82] of an RBC in shear flow. When $Ca = 0.06$ (figure 5.3(b)), the RBC is exerted by compressive

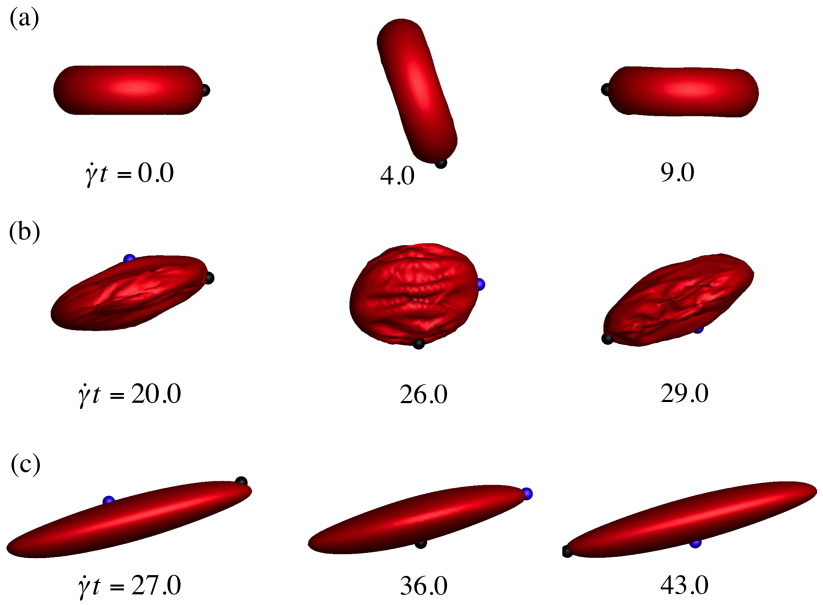

Fig. 5.3 Time sequence of the RBC in simple shear flow during a half periodic time in steady states with $Ca = (a)0.002, (b)0.06$ and (c)3. The viscosity ratio λ is set unity and the initial angle of θ is $\theta_0 = \pi/2$ in all cases. Numbers represented in each figure are non-dimensional time $\dot{\gamma}t$. The material points P and Q defined in figure 5.2 are indicated as black and blue dots on the membrane.

stress and membrane folding is observed. In this case, the shape of the RBC becomes quasi-circular profile in the shear plane ($\dot{\gamma}t = 26.0$ in the figure) and we do not see the obvious major-axis of the RBC in shear plane. The quasi-circular profile in the shear plane was also found in former numerical studies of an ellipsoidal capsule [44, 88] and experimental studies of a vesicle [19]. Even in the case of the RBC type biconcave disk, we observe the quasi-circular profile in the shear plane, and we define that such a motion is called as a tumbling-swinging transition.

For more detailed analysis of the RBC motion, the angle β during the period with $\lambda = 1$ and 3 are shown in figure 5.4. For all cases, $\theta_0 = \pi/2$. In tumbling regime ($Ca = 0.002$, figure 5.4(a)), the RBC rotates like rigid particle, thus the angle β always corresponds to α. Two lines with $\lambda = 1$ and 3 overlap, and continuously change from $-\pi/2$ to $\pi/2$. In swinging regime ($Ca = 3.0$, figure 5.4(c)), β/π oscillates slightly around a mean value about 0.08 ($\lambda = 1$) or 0.04 ($\lambda = 3$). In transition regime ($Ca = 0.06$, figure 5.4(b)), the curves of angle β is no longer continuous and the

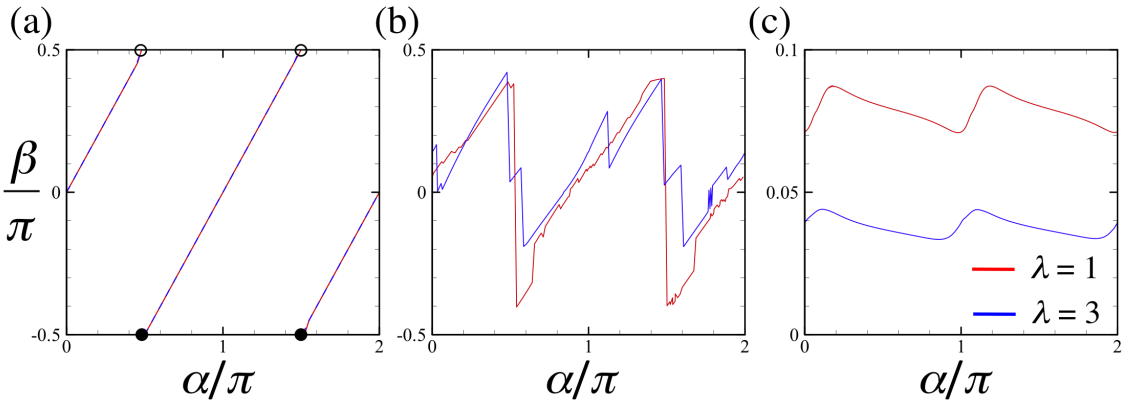

Fig. 5.4 Inclination angle β as a function the angle α in the steady periodic states with $Ca = (a)0.002, (b)0.06$ and (c)3. Definitions of α and β are shown in figure 5.2. Red curves represent the results of $\lambda = 1$ and blue curves are those of $\lambda = 3$. For all cases, $\theta_0 = \pi/2$.

discontinuous jump is frequently observed. This is because the shape of the RBC becomes quasi-circular in both $\lambda = 1$ and 3 cases, and the longest axes sometimes exist at two different positions, i.e. many material points are on the concentric circle in the shear plane. As a result, the curve of angle β is no longer continuous and the discontinuous jump is frequently observed, which means that we cannot clearly distinguish the unique orientation. To determine whether the RBC is in the transition regime or not, we use the following equation: $|\beta_{jmp}| \geq \beta_{tol}$. Where β_{jmp} is the maximum discontinuous jump of β in one period. The threshold β_{tol} is set as $\pi/4$ in this study, though the results are unaffected by β_{tol} if the value is not too small.

In order to discuss the phase of kinematic motion of the RBC with $\theta_0 = \pi/2$, it is convenient to use the amplitude of β oscillation during one period, indicated by $\Delta\beta$. Because the tumbling phase corresponds to $\Delta\beta = \pi$, and the swinging phase corresponds to $\Delta\beta < \pi$, except discontinuous β cases defined as the transition phase. The results of $\Delta\beta$ as a function of Ca and λ are shown in figure 5.5. In low Ca regime (red region in the figure), the RBC shows tumbling motion and $\Delta\beta$ is equal to π. In swinging regime (from green to blue region in the figure), $\Delta\beta$ decreases as Ca is increased. The transition regime is represented as a white-out in the figure. The results illustrate that the tumbling and swinging regime is separated by the transition

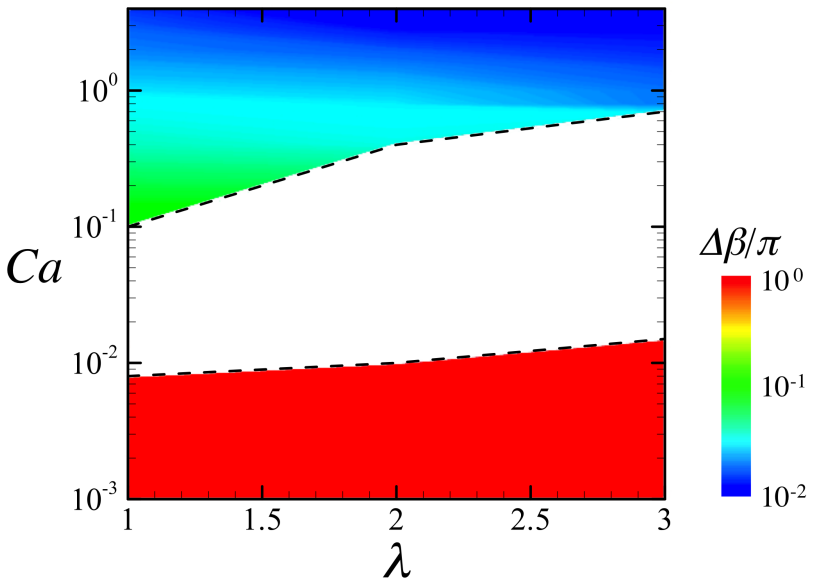

Fig. 5.5 Amplitude of the inclination angle $\Delta\beta$ as functions of Ca and λ. The color indicates $\Delta\beta/\pi$ in log scale. For all case, $\theta_0 = \pi/2$.

phase. We think the transition of the RBC motion occurs rather continuously in the parameter space of λ and Ca, and the transition phase is just where the motion cannot be distinguished accurately from one another.

5.3.2 Reorientation

Next, we investigate the kinematic motion of the RBC in simple shear flow with arbitrary angle θ_0. Due to the symmetry of the system, θ is defined in range of $[0, \pi/2]$. In figure 5.6(a), profiles of the RBC in the shear plane with $Ca = 2$, $\lambda = 1$ and $\theta_0 = \pi/4$ are shown. The motion of the RBC is unsteady with time, because the revolution axis is not initially located in the shear plane, i.e. $\theta_0 \neq 0$ or $\theta_0 \neq \pi/2$, and the membrane material properties are asymmetry towards both the flow and vorticity directions. The shape of RBC oscillates with time but the material point Q (indicated as a blue dot in the figure) gradually moves to the x_3-axis with a rotation around the deformed membrane. The material point Q reaches close enough to the x_3-axis after long time duration, the motion of the RBC becomes steady, because the material

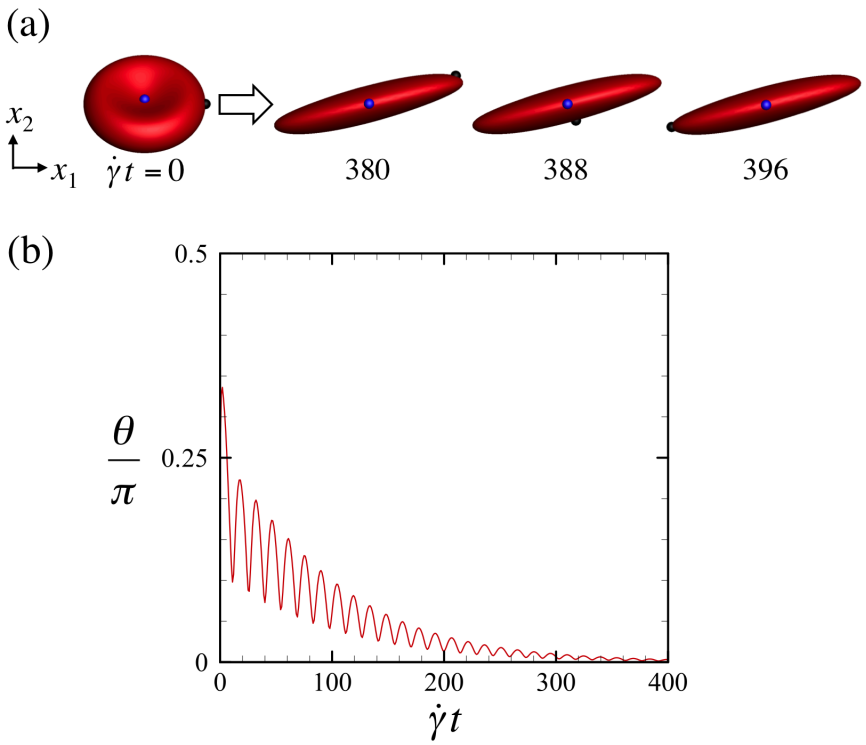

Fig. 5.6 Motion of the RBC in a simple shear flow with $Ca = 2$, $\lambda = 1$, and $\theta_0 = \pi/4$. (a) Profiles of the RBC in shear plane. Non-dimensional time is represented where the below in each figures. The material points P and Q are indicated as black and blue dots, respectively. (b) Time change of θ.

properties of the membrane are now symmetry towards both the flow and vorticity direction. The time history of θ is shown in figure 5.6(b) with $0 \leq \dot{\gamma}t \leq 400$. Due to the non-spherical reference shape of the membrane, θ oscillates two times during one rotation. After long time duration (about $\dot{\gamma}t \geq 350$ in this case), θ converges to 0. To the best of our knowledge, such a reorientation phenomena of an RBC, as well as an ellipsoidal capsule, has never been reported before, because in former numerical studies of a spheroid ellipsoidal capsule, the initial revolution axis was always in the shear plane. Such a case, the spheroid capsule shows only swinging motion or tumbling motion depending on the shear rate. Another reason why the reorientation of a capsule has not been reported, may be because of the difficulty in the control of the capsule orientation experimentally.

To discuss the reorientation phenomena of a non-spherical capsule more in general,

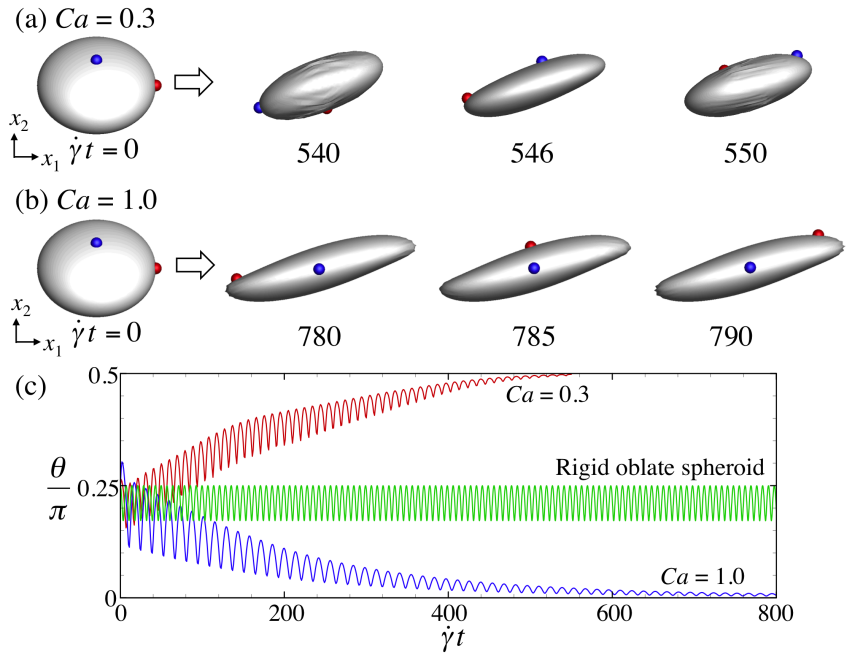

Fig. 5.7 Oblate capsule ($a/b = 0.6$) in a simple shear flow with $Ca = (a)0.3$ and (b)1.0. The membrane is modeled by the NH law and $\lambda = 1.0$. Red and blue dots represents the material points P and Q, respectively. (c) Time change of θ, where the result of a rigid spheroid with same a/b [41] is also plotted for comparison.

we investigate the motion of an oblate spheroidal capsule with the NH membrane in shear flow. The motions of an oblate capsule with $Ca = 0.3$ and 1.0 are shown in figure 5.7(a) and (b), respectively. The aspect ratio is $a/b = 0.6$, and the viscosity ratio is $\lambda = 1$. The time history of θ is also shown in figure 5.7(c) for 30 periods of rotation. The results of a rigid spheroidal with the same aspect ratio [41] are also plotted in the figure for comparison. As the same for the RBC, θ oscillates two times during one rotation. Surprisingly, θ tends to approach towards 0 or $\pi/2$, depending on Ca, over a long time duration. The reorientation of the capsules is also clear in observing figure 5.7(a) and (b), because the material point Q, which is indicated as a blue dot in the figures, moves towards $x_3 = 0$ when $Ca = 0.3$, whereas it moves towards the x_3-axis when $Ca = 1.0$. We note that the final orientation is independent of θ_0; this was confirmed numerically by changing the initial orientation randomly. Such reorientation did not happen for a rigid spheroid, as shown in figure 5.7(c).

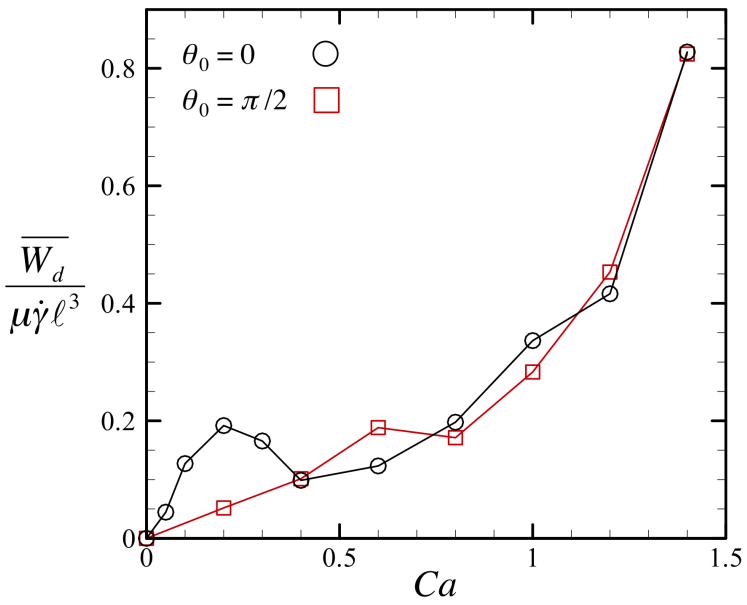

Fig. 5.8 Dissipation energy due to the capsule motion with $\lambda = 1$. The aspect ratio of the spheroid is $a/b = 0.6$ and the membrane is modeled by the NH law.

These results clearly illustrate that a deformable capsule, not only the RBC type biconcave disk but a spheroidal capsule, becomes reoriented, even in simple shear flow, and the time reversibility of Jeffery's orbit can be destroyed by introducing particle deformability.

The results of figure 5.7 raise another important question about why the reorientation direction shows transition with increasing Ca. Jeffery speculated that an ellipsoid may alter its orientation so that the viscous energy dissipation of the system becomes minimal [41]. We then investigate the viscous energy dissipation due to the capsule motion to determine whether the transition occurred to minimize the dissipation energy. In the case of $\lambda = 1$, the effective energy dissipation rate due to the capsule motion is given by

$$W_d = \int_S \underline{q} \cdot \underline{v} dS. \tag{5.7}$$

If in the case of $\lambda \neq 1$, we must consider the stress vector on the surface S^{out}, S^{in}, respectively. Time average W_d (denoted by $\overline{W_d}$) of the oblate capsule ($a/b = 0.6, \lambda =$

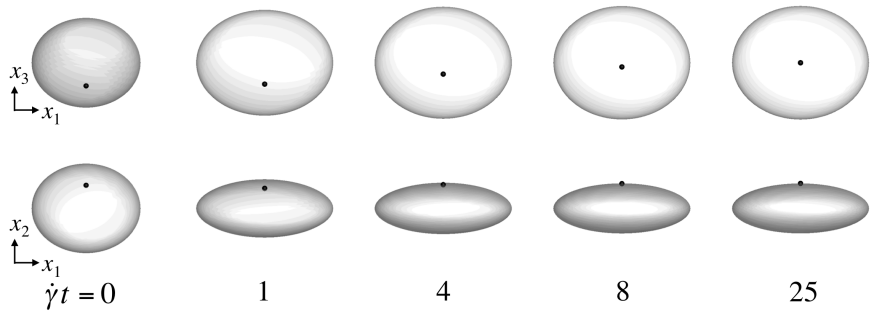

Fig. 5.9 Motion of an oblate capsule in steady planar elongational flow ($a/b = 0.6$, $Ca = 0.3$, $\lambda = 1$, the NH membrane) in the (x_1, x_2)-plane (bottom), in the (x_1, x_3)-plane (top). Black dots on the membrane indicate the material point Q. We investigate motion of the capsule with an arbitrary initial orientation and various Ca conditions, the orientation is finally directed towards the compressing direction, in all cases.

1) with the NH membrane are shown in figure 5.8. The values of $\overline{W_d}$ with $\theta_0 = 0$ and $\theta_0 = \pi/2$ are similar in $Ca > 1$ regime. Besides, in whole range of Ca, we do not observe a one-to-one correlation between the capsule reorientation and the minimum energy dissipation. This result suggests that the reorientation phenomena cannot explain only from the minimum energy dissipation of the system but the full fluid and solid mechanics must be examined to understand them.

To understand the basic mechanism of the transition, we further simplify the background flow field by deleting the rotational contribution from the shear flow. When an oblate capsule with an arbitrary initial orientation is subjected to steady planar elongational flow, as depicted in figure 5.1(b), with various Ca conditions. In the case of the steady planar elongational flow, the orientations are finally directed towards the compressing direction in all Ca cases. For example, the results of $a/b = 0.6$, $\theta_0 = \pi/4$, $Ca = 0.3$, and $\lambda = 1$ are shown in figure 5.9. Given that the reorientation transition does not appear in steady planar elongational flow, the unsteadiness in the flow field likely plays an important role in the transition.

Next, we apply oscillatory planar elongational flow, given by figure 5.1(c), to an oblate capsule. In this flow field, the elongational rate and changing frequency of the elongational direction can be independently controlled. At $t = 0$, the oblate capsule without pre-stress is placed at $\theta_0 = \pi/4$. The capsule motions for the second period

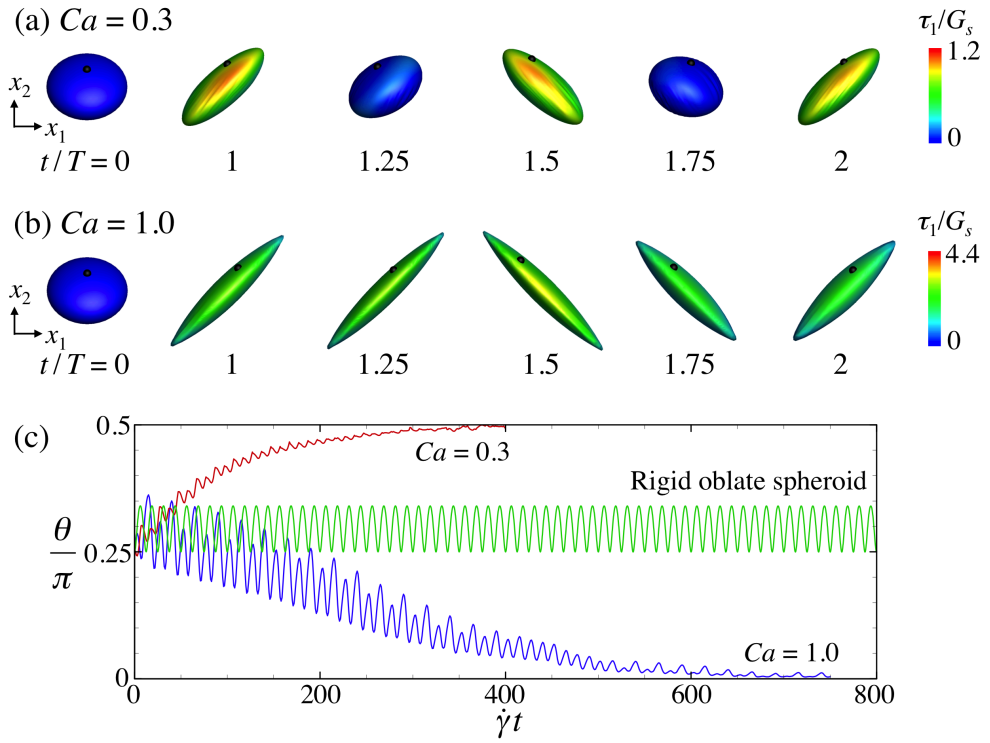

Fig. 5.10 Motion of an oblate capsule in oscillating planar elongational flow with $\omega/(\dot{\gamma}\pi) = 0.08$ and (a) Ca = 0.3 or (b) Ca = 1.0 ($\alpha = 0.6$, $\lambda = 1$, and NH membrane). Contour on the membrane represents distribution of the principal elastic tension τ_1. A black dot is placed at Q as a tracer. (c) Time change of θ, where the result of a rigid spheroid with same α [41] is plotted for comparison.

of oscillation with $\omega/(\dot{\gamma}\pi) = 0.08$ and $Ca = 0.3$ and 1.0 are shown in figure 5.10 ($a/b = 0.6$, $\lambda = 1$, and NH membrane). Color contours show the distribution of τ_1, where τ_i is the in-plane principal elastic tension and $\tau_1 \geq \tau_2$. The time history of θ is also shown in figure 5.10(c) for 30 periods of oscillation. When $Ca = 0.3$, θ approaches to $\pi/2$ after a sufficient time duration, whereas when $Ca = 1.0$, θ approaches to 0. For $Ca = 0.3$, the capsule deformation is small at $t/T = 1.25$ and 1.75, when there is no background flow, and the τ_1 distributions at $t/T = 1.0$ and 1.5 are similar. For $Ca = 1.0$, however, large deformations remain at $t/T = 1.25$ and 1.75, resulting in an asymmetry in the τ_1 distribution between $t/T = 1.0$ and 1.5. Thus, the deformation is strongly affected by the time history in the high Ca regime, whereas it is quasi-steady in the low Ca regime. This qualitative difference in the tension distribution likely causes the reorientation transition.

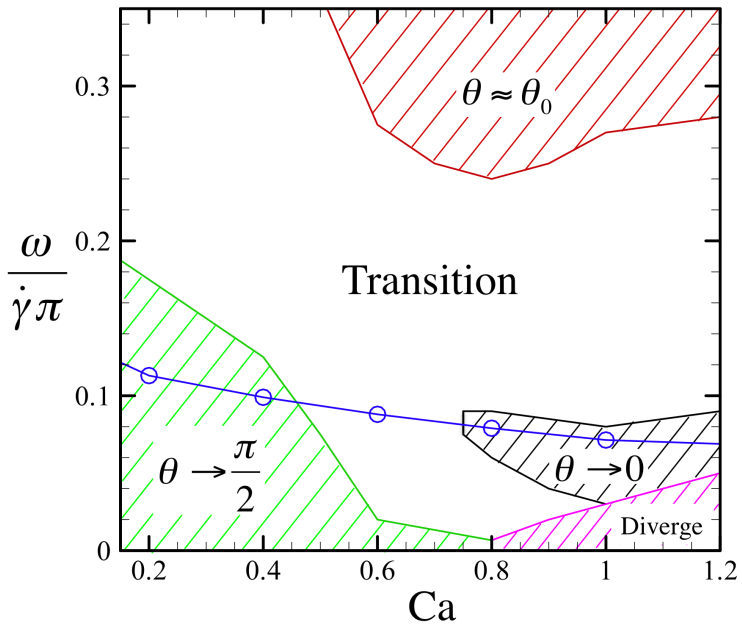

Fig. 5.11 Phase diagram of the oblate capsule in oscillating elongational flow ($a/b = 0.6$, $\lambda = 1$, and NH membrane). The circles in the figure indicate the converted results of the shear flow case.

To clarify the reorientation phenomena more in detail, we plot a phase diagram of the final orientation as a function of Ca and $\omega/\dot{\gamma}\pi$. An oblate capsule is again subjected to the oscillatory planar elongational flow with $\theta_0 = \pi/4$ ($a/b = 0.6$, $\lambda = 1$, and NH membrane). The computation is carried out for 30 periods of oscillation, which is sufficient to examine reorientation, as shown in figure 5.10(c). The convergence of the final angle is determined by the following equation: $|\theta_{30} - \theta_f| \leq \epsilon$, where θ_{30} is the average orientation vector of the 30th rotation, and $\theta_f = 0$, $\pi/2$ or θ_0. The threshold value of $\epsilon = 0.05$ is used in this study, although the results are unaffected qualitatively by the selection of ϵ if it is sufficiently small. When the convergence criteria is not satisfied, we determined that the reorientation is in the transit regime. Such capsules might have a reorientation speed that is too slow or multiple stable final angles.

The results of the phase diagram are shown in figure 5.11. θ converges to $\pi/2$ when Ca and ω are small, which is indicated as a green region in the figure. When ω is very large, no obvious change in θ is observed, which is indicated as a red region in the

figure. The magenta region in the figure indicates that the computation is diverged due to the infinitely large deformations of the strain-softening membrane, though a strain-hardening membrane can avoid this problem [9, 24]. In the white region, we did not observe the convergence of θ in 30 periods. In the high Ca regime, θ converges to 0 when ω is moderate, which is indicated as a black region in the figure. These results clearly illustrate that the convergence of $\theta \to 0$ appears only when the deformation is strongly affected by the time history.

In the case of shear flow, the elongational direction relative to the material point on the membrane oscillates with the angular velocity of the membrane motion. Thus, one may assume ω as the average rotational velocity of a capsule in shear flow and draw the curve shown in figure 5.11. The results of an oblate capsule in shear flow, shown in figure 5.7, are plotted in figure 5.11 by circles. A curve with small Ca exists in the $\theta \to \pi/2$ region, whereas a curve with large Ca exists in the $\theta \to 0$ region. These results indicate that the reorientation transition found in the shear flow can also be explained by using figure 5.11.

Next we investigate the reorientation of an RBC in shear flow with various Ca and λ conditions. To effectively discuss the effect of λ and the constitutive law on the reorientation transition in shear flow, we define critical values of Ca: $Ca_{\pi/2}$ indicates the maximum Ca value to show $\theta \to \pi/2$ convergence, and Ca_0 indicates the minimum Ca value to show $\theta \to 0$ convergence. The criterion of the convergence is the same as figure 5.11. The results of the RBC as well as spheroidal capsules with $a/b = 0.4$ and 0.6, and with two types of membrane constitutive laws are shown in figure 5.12 as a function of λ. $Ca_{\pi/2}$ and Ca_0 tend to decrease as λ increased. This is because the time history of deformation remains for a longer time as the inside viscosity increased, which leads to the transition in the smaller Ca conditions. The figure also indicates that the effect of the constitutive law is considerable. A capsule with the SK membrane tends to have a larger critical Ca_0 than that with the NH membrane. This is because the SK law shows the strain-hardening property, whereas NH law shows the strain-softening, so large deformations are suppressed by the SK membrane. Thus, the reorientation transition can be understood by considering the fluid and solid mechanics of capsule deformation. We also note that the phase transition during

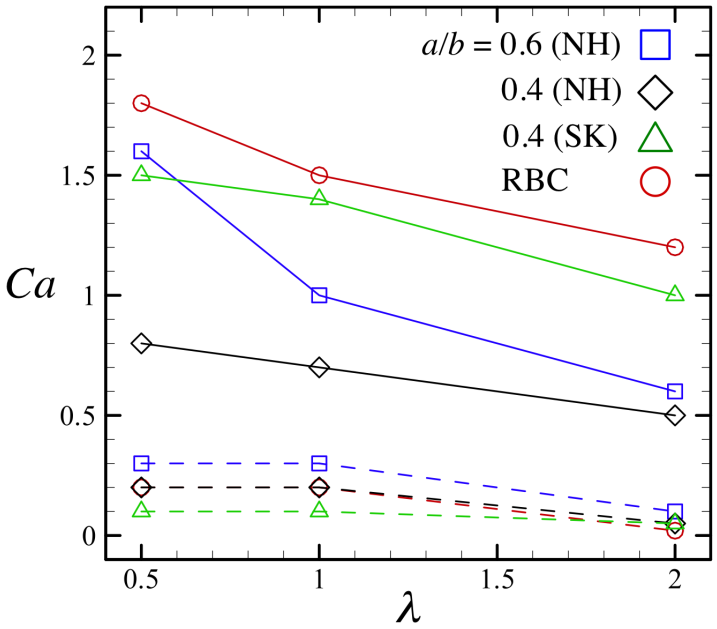

Fig. 5.12 Effects of λ on the critical Ca number of oblate capsules and a RBC (NH:neo-Hookean, SK:Skalak's law with $C = 10$). The solid lines in the figure indicate Ca_0, and the broken lines indicate $Ca_{\pi/2}$.

reorientation is observed for a prolate spheroidal capsule, although the results are not included here. Thus, reorientation transition is robust regardless of the reference shape of the capsule.

When $\theta = 0$, the RBC membrane have a pure tank-treading motion, and the membrane no longer oscillates during the rotation. Such a pure tank-treading motion of the RBC was observed in classical studies performed at high shear stress conditions. Fischer et al. (1978) [29], for instance, measured the motion of tracer particles on an RBC in shear flow and reported that the RBC showed the steady tank-treading motion. This fact was actually recognized by Abkarian et al. (2007) [1], who first reported the swinging motion of a RBC. In order to compare our results and the experimental results of two former studies: Fischer et al. (1978) and Abkarian et al (2007), the experimental conditions are inserted in figure 5.12 and results are shown in figure 5.13. The experimental conditions of two former experimental studies are as

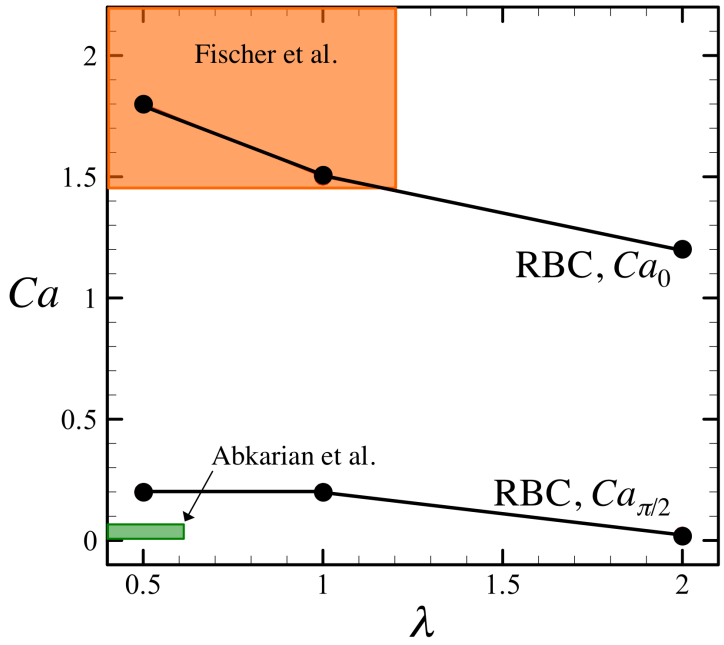

Fig. 5.13 Comparison between the present results and former two experimental studies [1, 29].

follow: Dextran solutions were used as the outer working fluid in these two studies. The viscosity of the working fluid μ is estimated from 22 to 47 (mPa.s) in Abkarian et al., and from 11 to 59 (mPa.s) in Fischer et al.. The maximum shear rate exerted on RBCs is set as 5 (s^{-1}) in Abkarian et al., and 800 (s^{-1}) in Fischer et al.. If we assume that the internal volume of an RBC equals to 94 (μm^3) [27], the characteristic length ℓ is derived as 2.82 (μm). If the shear elastic modulus G_s is assumed as 11 to 17 (μN/m) [18], the maximum capillary number ($Ca_{\max}$) of each experimental study is estimated from 0.018 to 0.06 (Abkarian et al.), and from 1.46 to 7.69 (Fischer et al.). When the internal viscosity $\lambda\mu$ is estimated from 10 to 13.2 (mPa.s) [17], the viscosity ratio λ becomes about 0.21 - 0.6 (Abkarian et al.), and 0.167 - 1.2 (Fischer et al.). The orange region in figure 5.13 indicates $Ca_{\max}$ of Fischer et al. and the region exists above the curve Ca_0, which indicates that the RBC motion does not oscillates with time. This tendency is consistent with the Fischer's observation that the RBC shows steady tank-treading motion. $Ca_{\max}$ region of Abkarian et al. (indicated as

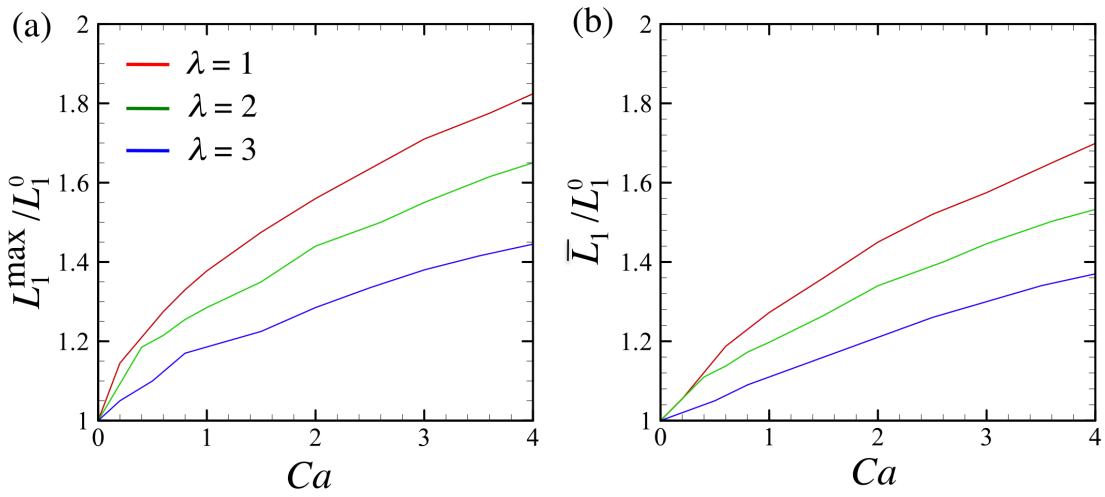

Fig. 5.14 Major axis length L_1 of the RBC in simple shear flow with various Ca and λ conditions. $\theta_0 = \pi/2$ in all cases. (a)The maximum value of L_1 and (b)time average of L_1 during steady periodic motion are shown in the figure, respectively. Even when the RBC is in the transition regime, the magnitude of L_1 can be estimated but it is impossible to determine the inclination angle.

green region in the figure) exists below the curve of $Ca_{\pi/2}$, which indicates that the RBC motion oscillates with time. This tendency is consistent with the Abkarian's observation that the RBC shows swinging motion. Therefore, our results can nicely explain the difference of two former experimental observations by Abkarian et al. and Fischer et al..

5.4 Rheology of a dilute-suspension of RBCs

5.4.1 Deformation of an RBC in shear flow

Next, we investigate the deformation of the RBC in simple shear flow with various Ca and λ. Flow-induced deformation is directly correlated to the membrane tension and the stresslet, so that the knowledge of the deformation can be useful for better understanding the rheology of the RBC in shear flow.

The maximum and averaged major axis length during one period $L_1^{\max}$ and $\overline{L}_1$ are shown in figures 5.14(a) and (b), respectively. θ_0 is set to $\pi/2$ in all cases. The RBC is gradually elongated towards the flow direction as Ca increases. The slope

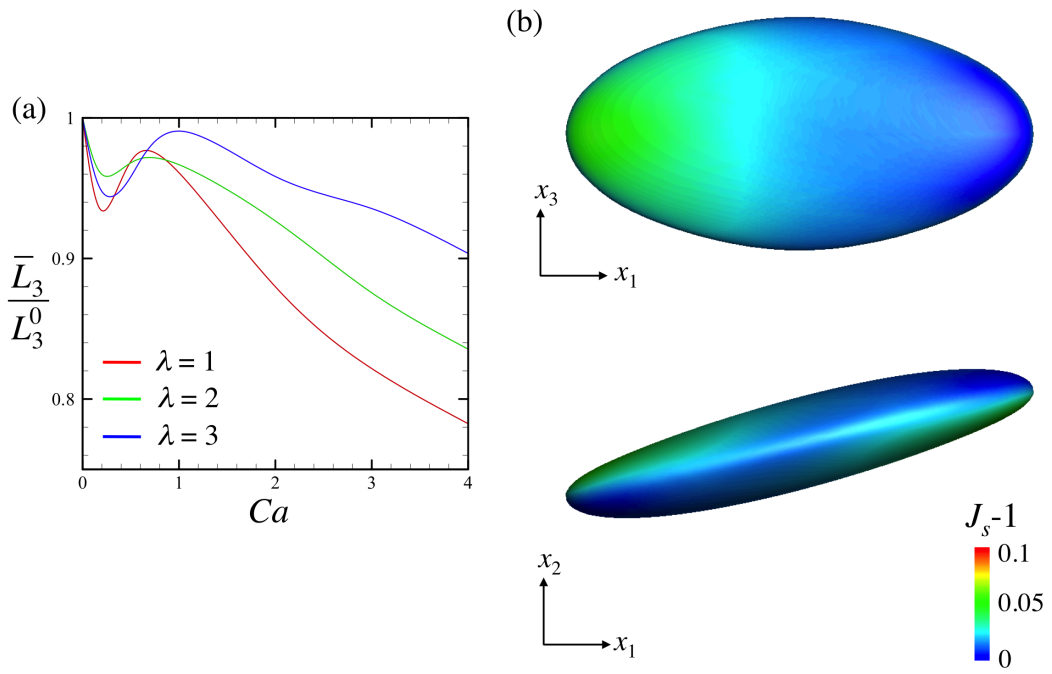

Fig. 5.15 (a) Time average semi-axis length L_3 with various Ca and λ conditions. (b) Distributions of the relative surface area change ($Ca = 2.0$, $\lambda = 1.0$). The color contour on the membrane indicates the value of $J_s - 1$, which corresponds to the relative local area change.

becomes smaller as Ca is enough large, because the membrane is modelled by the SK law, which shows a strain-hardening property and the large deformation is suppressed. The deformation also tends to be suppressed when the viscous effect inside the capsule becomes large, i.e. high λ condition. These results suggest that not only the shear rate but the viscosity ratio of the internal and external liquids dominate the deformation of the RBC in shear flow. We note that even when the RBC is in the tumbling-swinging transition regime, the magnitude of L_1 can be estimated but it is impossible to ditinguish the inclination angle.

The semi-axis length L_3 are also shown in figure 5.15(a). The numerical conditions are the same with figure 5.14. The values of L_3 decrease as Ca increases for all λ cases. In this study, the RBC membrane is modeled by the SK law with $C = 10$. In the case of the SK law with higher value of C, the area dilation is strongly suppressed.

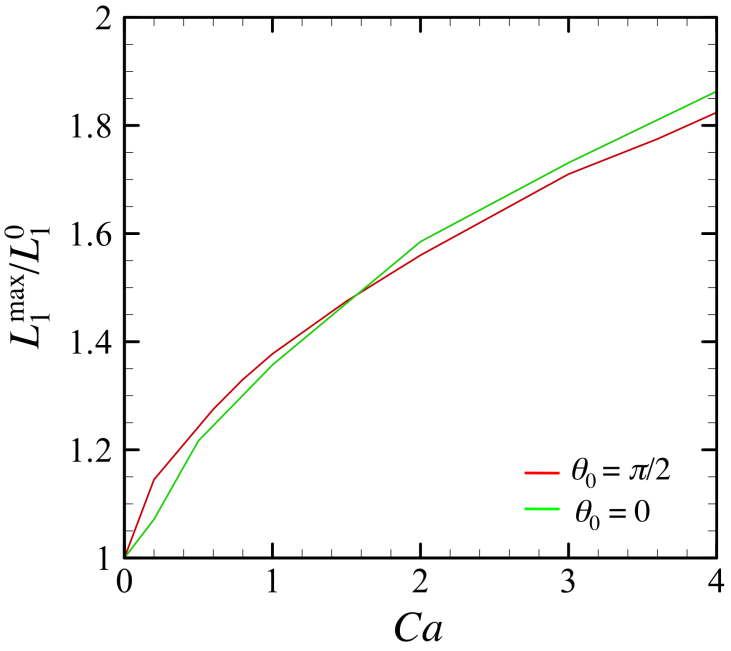

Fig. 5.16 Effects of θ_0 on the deformation of an RBC with $\lambda = 1$.

In high Ca regime, the RBC is elongated towards flow direction, as shown in figure 5.14. To preserve the surface area of the RBC membrane, L_3 tends to decrease as Ca increases. Distributions of the relative surface area change are shown in figure 5.15(b) ($Ca = 2.0$, $\lambda = 1.0$). The color contour on the membrane indicates the value of $J_s - 1$, which corresponds to the relative local area change. This figure indicates that the areal change is less than 5% at any point on the membrane. The overall areal change of the RBC is less than 2%, which can be much smaller in low Ca cases. Thus, the area incompressibility of the RBC membrane is satisfied through the computation. From these results, we conclude that the RBC deformation is strongly dependent on the membrane model and we must choose a suitable model to express the mechanical properties of the biological membrane.

We also investigate the effects of θ_0 on the deformation of the RBC. The major axis length L_1 with $\theta_0 = 0$ and $\pi/2$ are shown in figure 5.16. The viscosity ratio is unity in all cases. In the case of $\theta_0 = 0$, the RBC shows pure tank-trading motion in high Ca regime and L_1 becomes constant with time. In the case of $\theta_0 = \pi/2$, the RBC

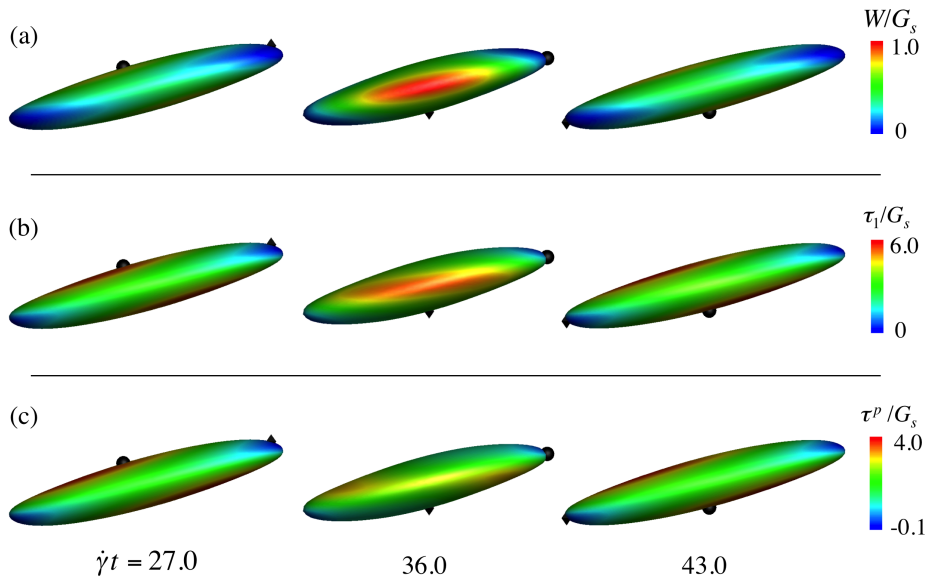

Fig. 5.17 Distributions of (a) the elastic energy function W, (b) in-plain elastic principal tension τ_1, and (c) the isotropic membrane tension τ^p. Capillary number is set as $Ca = 3$, and $\lambda = 1$. The initial angle θ is $\theta_0 = \pi/2$, then the RBC shows the swinging motion. A diamond and black dot on the membrane indicate the material point P and Q, respectively.

shows swinging motion in high Ca regime and L_1 oscillates with time. The values L_1 with $\theta_0 = 0$ are similar to the maximum values of L_1 with $\theta_0 = \pi/2$ during the period in whole range of Ca. The maximum difference between $\theta_0 = 0$ and $\theta_0 = \pi/2$ is less than 2%. Then, the shape of deformed RBC with $\theta_0 = 0$ is similar to the maximum deformation of the RBC with $\theta_0 = \pi/2$. This result suggests that the orientation of an RBC is important for its kinematic motion but the effect is moderate to the deformation of an RBC in shear flow.

5.4.2 Membrane tension

Knowledge of the membrane tension profile is important in predicting the membrane rupture and mechano-transduction of RBCs. We investigate now the in-plane principal tensions τ_i ($\tau_1 \geq \tau_2$) and the isotropic tension τ^p in the membrane of the RBC.

In figure 5.17 (a), distributions of the elastic strain energy W in the shear plane during a half time period is shown ($Ca = 3$ and $\lambda = 1$). The angle $\theta_0 = \pi/2$, then the

RBC shows swinging motion. W distribution changes periodically together with the shape oscillation, accordingly the principal tension τ_1 oscillates periodically (figure 5.17(b)). When the RBC is most elongated along the flow direction ($\dot{\gamma}t = 27.0, 43.0$ in the figure), high values of τ_1 appear on the top and bottom of the deformed RBC. When the RBC is most elongated along the x_3-direction ($\dot{\gamma}t = 36.0$), however, τ_1 becomes the highest at the side, which is the maximum value during the period. In the case of a hyper-elastic membrane, high values of the principal tension should be correlated to the yield tension of the material, i.e. the tolerated maximum elastic tension, thus these results about the high τ_1 region would be important for understanding the hemolysis.

Recently, some researchers have worked on the mechano-transduction of biological cells [3, 89, 93, 92]. Wiggins & Phillips [92] analytically investigated the elastic deformation of the bilayer surrounding the mechano-sensitive channel of large conductance (MscL). They showed that the deformation free energy becomes large under isotropic deforamtion and the importance of the isotopic tensions to opening of the mechano-sensitive channel on the membrane. Yoshimura et al. [93] reported that the mechano-sensitive ion channel MscL found in *Escherichia coli* cells is opened by isotropic tensions. Though ion channel structures of an RBC membrane is more complicated than that of bacteria, the isotropic tensions likely play an important role in the regulation of ion channels. In the case of a 2D isotropic elastic membrane, the isotropic membrane tension is calculated as $\tau^p = (\tau_1 + \tau_2)/2$. The distributions τ^p is also shown in figure 5.17(c). High value of τ^p only appear on the top and bottom of the deformed RBC, though the high principal tension periodically appeared at the side and top/bottom. Thus, the distributions of τ_1 and τ^p are qualitatively different in the RBC in shear flow.

We also investigate effect of θ_0 on the membrane tension. Distributions of τ_1 with $Ca = 3.0$, $\lambda = 1$, and $\theta_0 = 0$ are shown in figure 5.18(a). In the case of $\theta_0 = 0$, the RBC has a pure tank-treading motion in high Ca regime and τ_1 does not oscillate. The highest τ_1 appear on the side of deformed RBC as the same for $\theta_0 = \pi/2$. In figure 5.18(b), the maximum values of τ_1 during the period are shown. The results of $\theta_0 = 0$ are always higher than those of $\theta_0 = \pi/2$, even though the maximum deformed

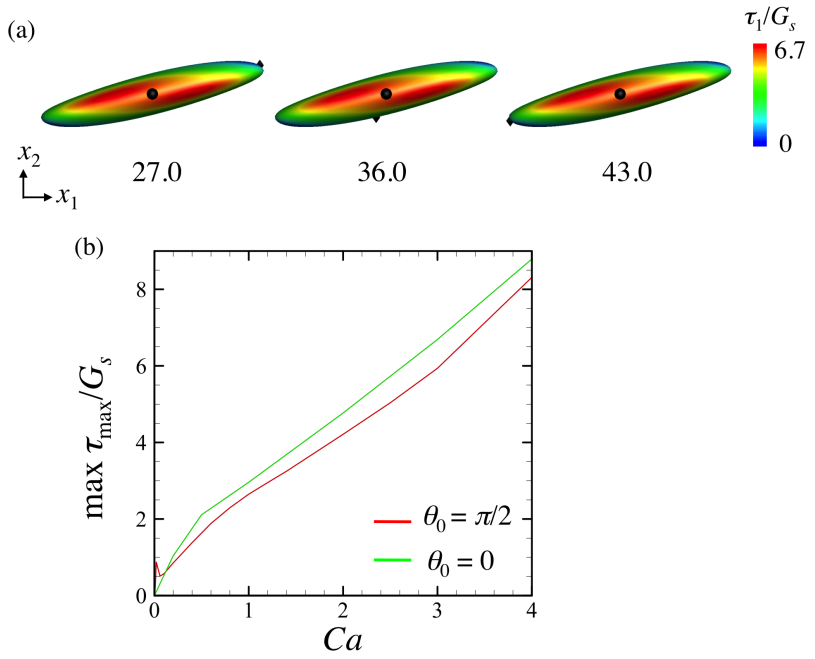

Fig. 5.18 (a) Distributions of τ_1 during a half time period of the membrane rotation with $Ca = 3$, $\lambda = 1$, and $\theta_0 = 0$. Material points P and Q is represented by black diamond and black dot on the membrane, rtespectively. (b)The maximum values of τ_1 during the period with $\theta_0 = 0$ and $\pi/2$. The viscosity ratio is unity.

length L_1 is similar between the two cases. The maximum difference between the two cases is about 10% in whole range of Ca. The biconcave disk, which is assumed as the reference shape, is strongly anisotropic, thus the membrane tensions depend on the stretch direction. These results suggest that not only the deformation but the orientation of the RBC should be taken into account for the membrane tension when the RBC is subjected to shear flow.

To more efficiently investigate the effect of Ca and λ on the principal tension, we define the maximum principal tension as:

$$\max(\tau_{\max}) = \max_{t}[\max_{\underline{x}} \tau_1(\underline{x}, t)], \tag{5.8}$$

where $\max_t$ indicates the maximum value in one period, and $\max_{\underline{x}}$ indicates the maximum value on the membrane. Results of $\max(\tau_{\max})$ with various Ca and λ are shown in figures 5.19. For all cases θ_0 is equal to $\pi/2$. The maximum principal tension $\max(\tau_{\max})$ is almost linearly increased with Ca, whereas the deformation of the RBC

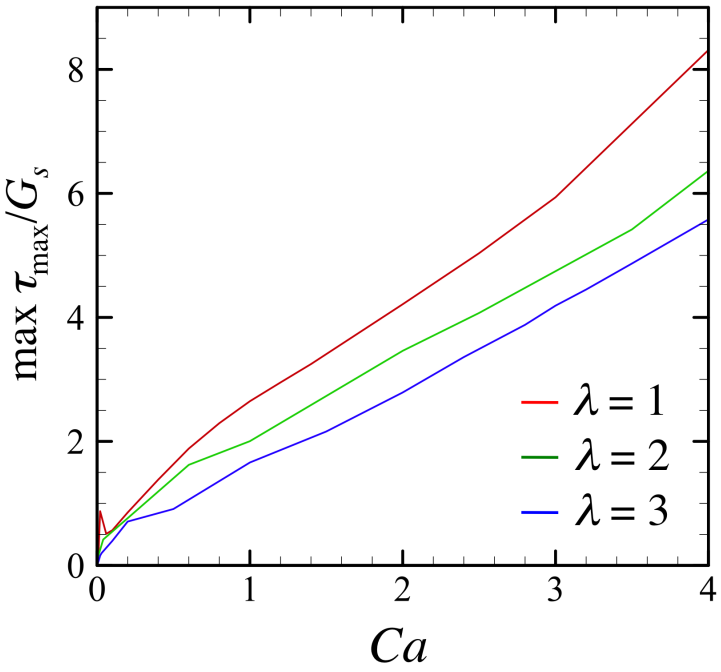

Fig. 5.19 The maximum principal tension during the period with $\lambda = 1, 2$ and 3. For all cases, $\theta_0 = \pi/2$.

becomes saturated in high Ca regime as shown in figure 5.14. The SK membrane shows the strain-hardening property, thus the membrane tension and deformation show different tendencies.

Next, we calculate the instantaneous maximum isotropic tension $\max(\tau^p_{\max})$, which may be considered as the criterion for the opening of the mechano-sensitive ion channel. We also calculate the averaged value of τ^p by using the equation:

$$\bar{\tau}^p = \frac{1}{ST} \int_T \int_S \tau^p(\underline{x}, t) dS dt, \tag{5.9}$$

where S is the surface area of the membrane and T is the period of rotation. Since the molecular release due to the RBC deformation may be proportional to the time of channel opening and the number of opened channel, $\bar{\tau}^p$ may be correlated with the total amount of molecules released from the RBC. We again see the almost linear relationships between Ca and $\max(\tau^p_{\max})$ as well as Ca and $\bar{\tau}^p$ (cf. figure 5.20). Wan et al [89] investigated shear-induced release of ATP from RBCs using a micro fluidic

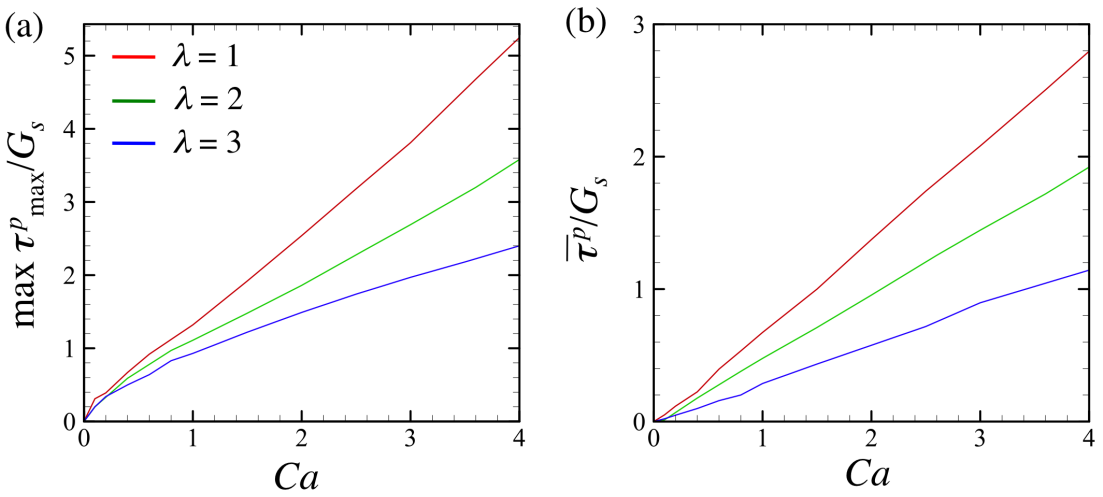

Fig. 5.20 (a) The maximum isotropic tension and (b) averaged τ^p with $\lambda = 1, 2,$ and 3. For all cases, $\theta_0 = \pi/2$.

channel. They reported that the amount of ATP release increased linearly with the shear rate. In their experiments, however, they could not measure the membrane stress due to experimental limitations. $\bar{\tau}^p$ increases linearly with the shear rate as shown in figure 5.20(b), which suggests that the mechano-transduction reported Wan et al. might also be regulated by the isotropic tension on the membrane.

Presence of the negative tension on the membrane often causes of the numerical instabilities. When the membrane is compressed by the fluid flow, the membrane is buckled and the computation becomes unstable. To investigate the negative tension on the membrane efficiently, we seek the maximum values of the spatial minimum principal tension during the period, which is denoted by $\max(\tau_{\min})$. When the membrane is always compressed somewhere during the period, $\max(\tau_{\min})$ becomes negative. $\max(\tau_{\min})$ with various Ca and λ conditions are shown in figure 5.21. For all cases, $\theta_0 = \pi/2$. In low Ca regime, $\max(\tau_{\min})$ become negative in all cases. The RBC is therefore exerted by the compression and membrane folding is observed in this regime, as shown in figure 5.3(b). In moderate Ca regime, $\max(\tau_{\min})$ become positive in lower λ cases ($\lambda = 1.0$ and 2.0), whereas these are still negative in higher λ. In high Ca regime (about $Ca \geq 3.8$ in the figure), all results again negative,

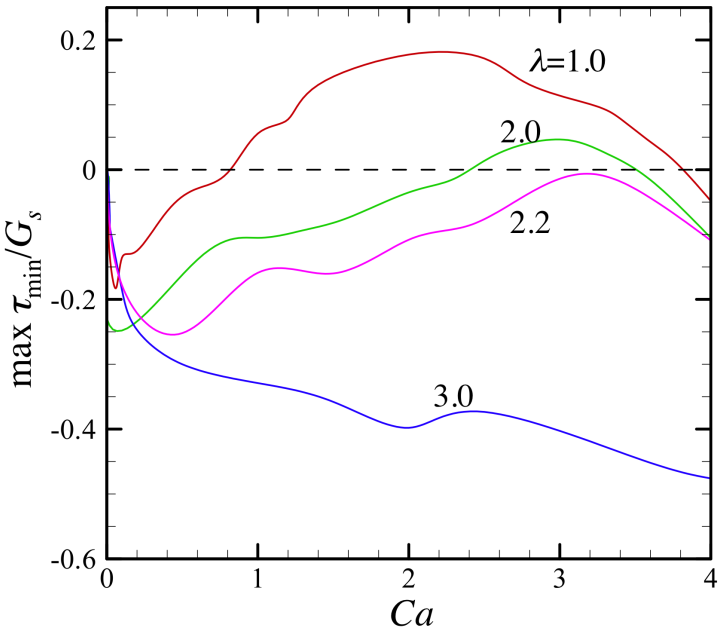

Fig. 5.21 Maximum values of the spatial minimum principal tension during the period $\max(\tau_{\min})$. For all cases, $\theta_0 = \pi/2$. When negative tension appear within the period, $\max(\tau_{\min})$ becomes negative.

because the membrane is too elongated at two tips of the capsule and membrane is buckled. In the case of $\lambda \geq 2.2$, $\max(\tau_{\min})$ are always negative, which suggests that the RBC membrane is always compressed somewhere and the calculation tends to unstable with higher λ.

Hemolysis is one of the biggest problem in the research field of artificial organs. Due to the non-physiological fluid stress level in the artificial organs, RBCs are often destroyed and internal hemoglobin solutions are seeped out. Freed hemoglobin scavenges NO in plasma, which is an inhibitor of platelet activation and a regulator of the smooth muscle tone [76]. Depletion of NO therefore contributes to thrombosis and many researchers have investigated the correlation between the subjected fluid shear stress level and the RBC membrane rupture. A threshold fluid shear stress is now commonly believed to the order of hundred pascal in plasma solution [50]. If we assume that the length scale $\ell = 2.82 \times 10^{-6}$ (m) [27] and the shear modulus $G_s = 1.7 \times 10^{-5}$ (N/m) [18], one hundred pascal is equivalent to $Ca \approx 16.6$, which is

about 4 times higher than our maximum Ca results. In this study, it is impossible to carry out the computation with such a higher number of Ca, because the mesh is too elongated to the flow direction at the two tips of the deformed RBC. If $\max(\tau_{\max})$ increase linearly with Ca until such a higher Ca regime, the maximum membrane tension in rupture regime will be about the order of 10^{-4} (N/m).

Yoshimura et al. [93] investigated the mechano-sensitive ion channel MscL in *E. coli* cells by patch clamp technique. They reported that mechano-sensitive Ca^{2+} channel in *E. coli* cells activated by 5 to 10 (kPa) with micropipette aspiration. In the case of RBCs, Wan et al [89] investigated shear-induced release of ATP from RBCs using a micro fluidic channel. In their experiment, applied average fluid shear stress is ranged in about 0.1 to 10 pascal, which value is much smaller than the studies of Yoshimura et al.. These results suggest that the mechano-sensitive channel of the RBC may be activated by much smaller membrane tension than that of *E. coli* cells.

5.4.3 Particle stress tensor

Consider now rheological properties of a dilute suspension of RBCs. Before discussions of the RBC suspension rheology, we first investigate the effective viscosity of a dilute suspension of spherical capsules with $Ca \ll 1$. The effective viscosity μ^* of identical rigid particles with $\phi \ll 1$ can be described by the well-known Einstein's viscosity equation [26]:

$$\mu^* = \mu(1 + 2.5\phi). \tag{5.10}$$

The effective shear viscosity contribution of the capsule, $\bar{S}_{12}^{sol}$, are shown in figure 5.22. The viscosity ratio is $\lambda = 1$ and the SK law with $C = 1$ is employed for the membrane. The effective shear viscosity is asymptotic to 2.5 in very low Ca regime. Which value corresponds to the analytical solution of the rigid spherical particle as described in (5.10), then we confirm that good agreement with our numerical results of a spherical capsule and analytical solution of rigid particle when $Ca \ll 1$.

Time change of effective shear viscosity contribution of the RBC in shear flow with $Ca = 0.002, 1.0$ and 4.0 are shown in figure 5.23. All results obtained with $\lambda = 1$ and $\theta_0 = \pi/2$. All curves oscillate with time, because the RBC shows a tumbling ($Ca = 0.002$) or swinging motion ($Ca = 1.0$ and 4.0) in these cases. We also see

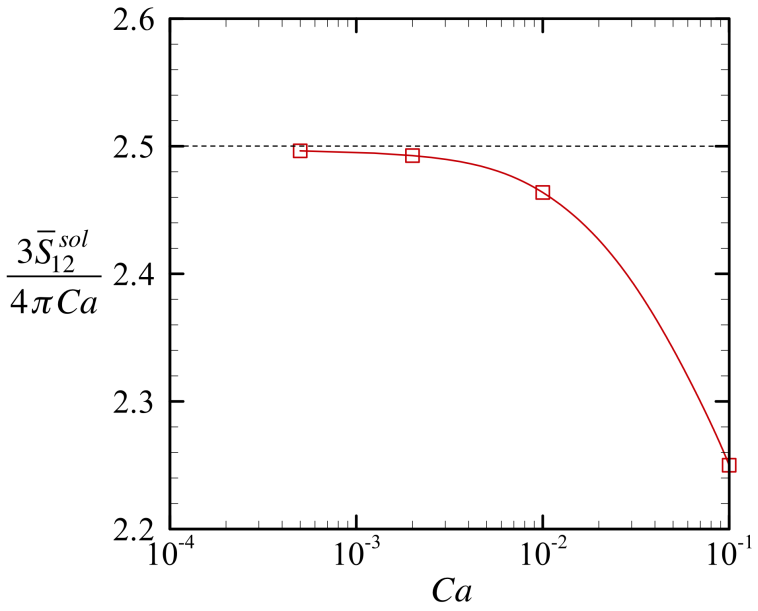

Fig. 5.22 Effective shear viscosity contribution of a spherical capsule with $\lambda = 1$. The broken line in the figure indicates the analytical solution of the identical rigid particles, which is given by (5.10).

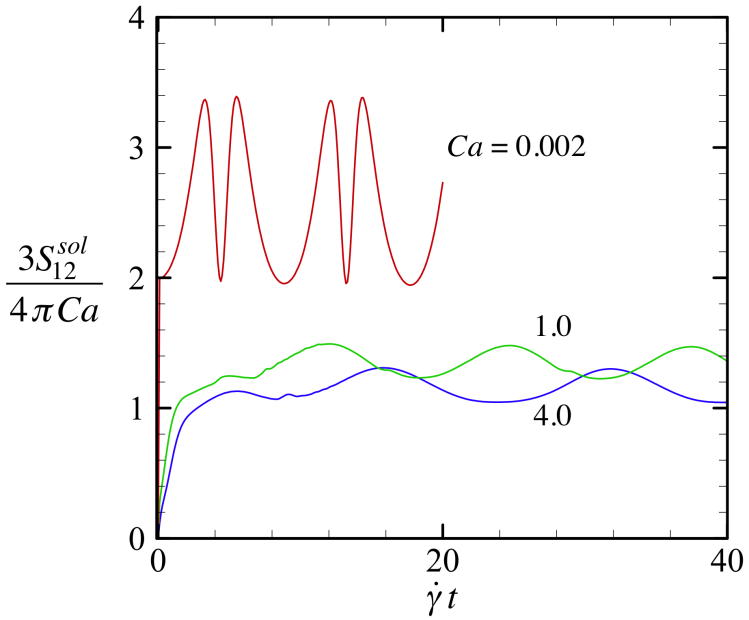

Fig. 5.23 Time change of effective shear viscosity contribution of the RBC with $Ca = 0.002, 1.0$ and 4.0. For all cases, $\lambda = 1$ and $\theta_0 = \pi/2$.

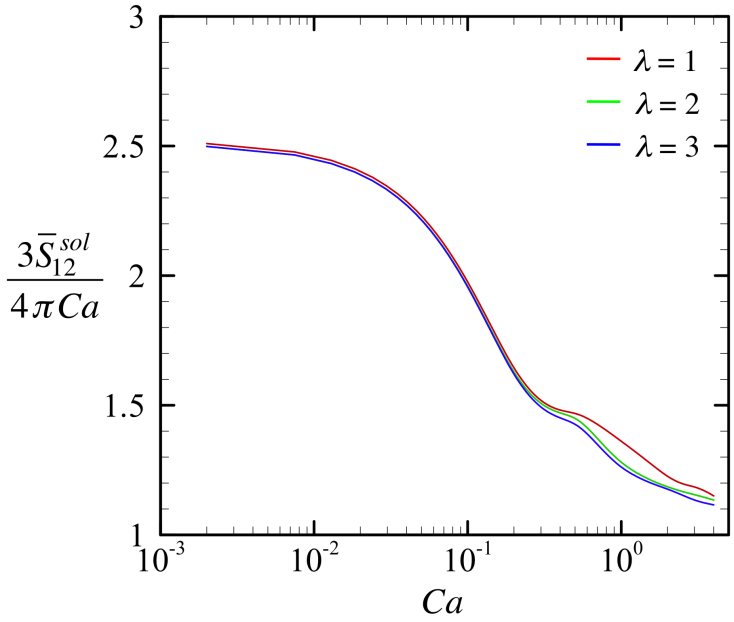

Fig. 5.24 Time average S_{12}^{sol} with $\lambda = 1, 2$ and 3. $\theta_0 = \pi/2$ in all cases.

that the average values of S_{12}^{sol} tends to decrease as Ca increases. Capillary number can be viewed as a non-dimensional shear rate for a given capsule in shear flow, this tendency then indicates that the shear-thinning behavour of the RBC suspension.

Next, we investigate the effects of λ on the effective shear viscosity of the RBC suspension. Time average effective shear viscosity $\bar{S}_{12}^{sol}$ with $\lambda = 1, 2$ and 3 are shown in figure 5.24. $\theta_0 = \pi/2$ in all cases. From this figure, we again see the shear-thinning behaviour of the RBC suspension in all λ cases. This tendency corresponds to former numerical studies of capsules and drops [58, 73]. In very low Ca regime, all curves overlap and are asymptotic to about 2.5. In this regime, the RBC shows rigid like tumbling motion, thus the effect of inner viscosity becomes small. In large Ca, on the other hand, the effective shear viscosities decrease as λ increases. This result is surprising because the shear viscosity of the suspension decreases, even though higher viscous capsules are immersed in. Moreover, it suggests that a suspension of inner-viscous capsule has efficient fluidity in the dilute regime.

To investigate the detailed mechanics of the shear viscosity of the suspension, we

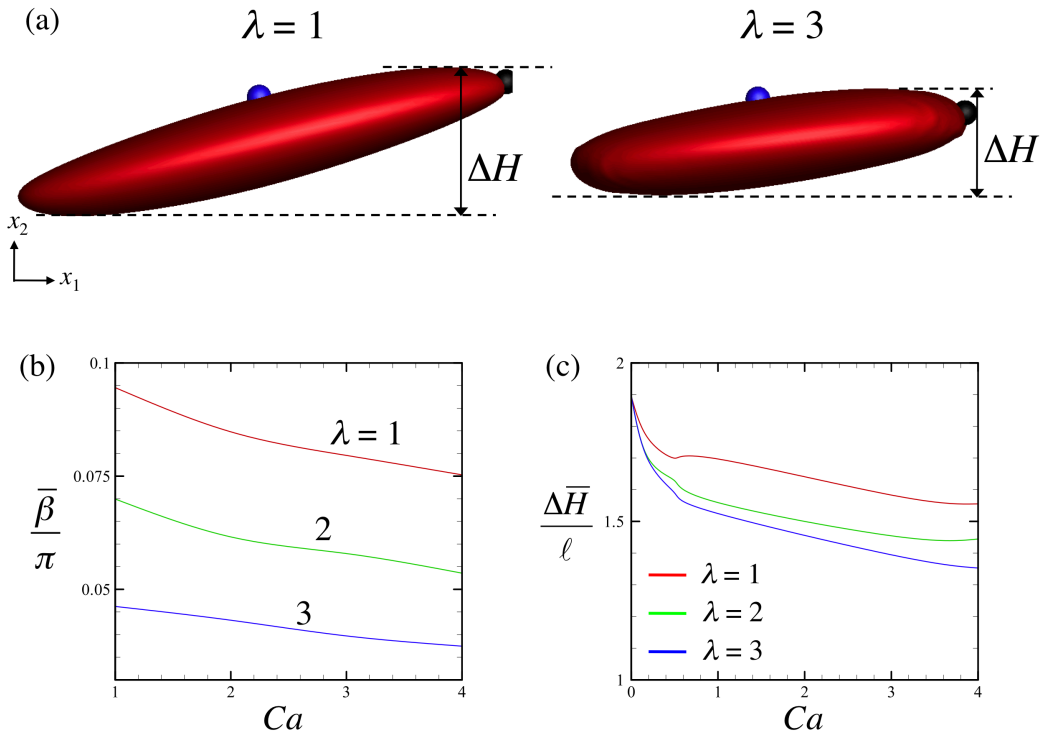

Fig. 5.25 (a)Hight of deformed RBC in the shear plane ΔH. (b)Time average inclination angle with $\lambda = 1, 2$ and 3 in swinging regime. (c)Time average ΔH with $\lambda = 1, 2$ and 3. $\theta_0 = \pi/2$ in all cases.

analyze the inclination angle β and hight of deformed RBC in the shear plane, which is denoted by ΔH (depicted in figure 5.25(a)). The results are shown in figures 5.25(b) and (c). Time average inclination angle $\bar{\beta}$ decrease with higher λ (cf. figure 5.25(b)). Accordingly, ΔH become small as λ increases (cf. figure 5.25(c)). In the case of simple shear flow, flow strength is proportional to the position of x_2. The effective shear viscosity S_{12}^{sol} then becomes small with higher λ, as shown in figure 5.24.

Next we investigate the effects of θ_0 on S_{12}^{sol} and the results are shown in figure 5.26. λ is set to unity in all cases. In the case of $\theta_0 = 0$, S_{12}^{sol} converges to about 4.3 in very low Ca regime, which value is higher than that of $\theta_0 = \pi/2$. In this Ca regime, the RBC behaves as a rigid like particle. In the case of anisotropic rigid particles, the effective shear viscosity strongly depends on its orientation. Jeffery [41] analytically derived the effective shear viscosity of an ellipsoidal rigid particle. In the case of an oblate rigid particle, the value becomes minimum when $\theta_0 = \pi/2$ and

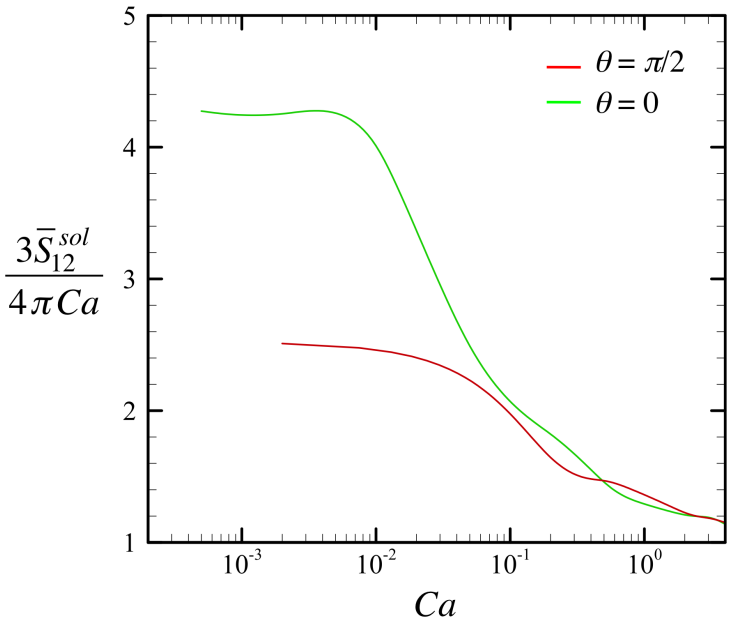

Fig. 5.26 Effects of θ_0 on time average S_{12}^{sol}. All cases, $\lambda = 1$.

becomes maximum when $\theta_0 = 0$ (if in the case of a prolate rigid particle, those are opposite). According to Jeffery's theory, the effective shear viscosity of the oblate spheroidal particle with $a/b = 0.3$, which has the same volume-surface area ratio of the RBC type biconcave disk, are ranged in [2.21,4.35]. Our numerical results of the RBC in very low Ca regime are similar to Jeffery's solutions for the oblate particle with $a/b = 0.3$.

In high Ca regime, on the other hand, the curves of $\theta_0 = 0$ and $\theta_0 = \pi/2$ are almost overlapped and the maximum difference between the two is less than 5% when $Ca \geq 1$. This is because the shape of RBC, as well as the inclination angle, between $\theta_0 = 0$ and $\theta_0 = \pi/2$ are similar and the effect of θ_0 becomes small. These results suggests that the orientations of the RBC less affect on the shear viscosity component of the stresslet in high Ca regime when the RBCs have no interaction to other cells.

Not only the shear viscosity, but the diagonal components of the stresslet are also important for the suspension rheology. The effective diagonal components of the stresslet are shwon in figures 5.27 (a) and (b). For all cases $\theta_0 = \pi/2$. The component

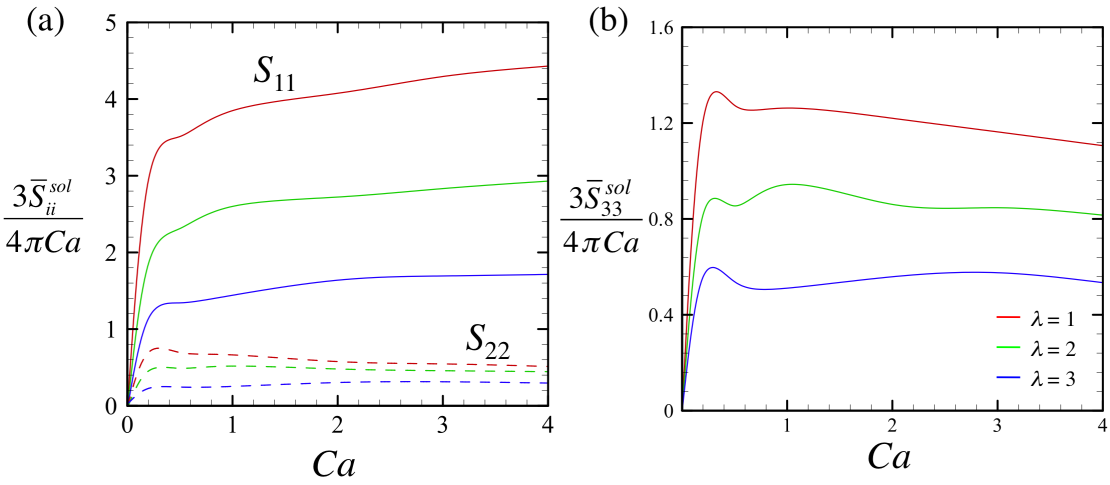

Fig. 5.27 Diagonal components of the stresslet (a)S_{11} (solid line), S_{22}(broken line) and (b)S_{33}. For all cases $\theta_0 = \pi/2$.

S_{11} become large as Ca increases and λ decreases (cf. figure 5.27(a)). The values of S_{33} also become large as λ decreases (cf. figure 5.27(b)). When the RBC is subjected to a simple shear flow, the length L_1 increases as λ decreases. Due to the area incompressibility of the membrane, the length L_3 is reciprocal to the length L_1, which is relevant to the strong deformation in x_3-direction when the RBC is subjected to strong flow strength. Thus, these results of S_{ii} suggest that the diagonal components S_{ii} are strongly dependent on the RBC deformation L_i, respectively. Which are also suggest that the membrane area incompressibility strongly affects on the stress component of S_{33}. The curves of S_{22} become almost plateau in whole range of Ca with all λ conditions. In whole range of λ and Ca, the RBC is not significantly elongated towards x_2-direction, then S_{22} become almost independent of Ca.

As shown in figure 5.27, the diagonal components of the stresslet are no longer isotropic, whereas a Newtonian fluid has the isotropic components in shear flow. Such anisotropic stress components cause of the visco-elastic properties of the suspension. Subsequently, we investigate the first normal stress difference of the RBC suspension $N_1(= S_{11} - S_{22})$, as well as the second normal stress difference $N_2(= S_{22} - S_{33})$. Results of N_1 and N_2 are shown in figures 5.28(a) and (b), respectively. The first normal stress difference N_1 becomes positive and the second normal stress difference

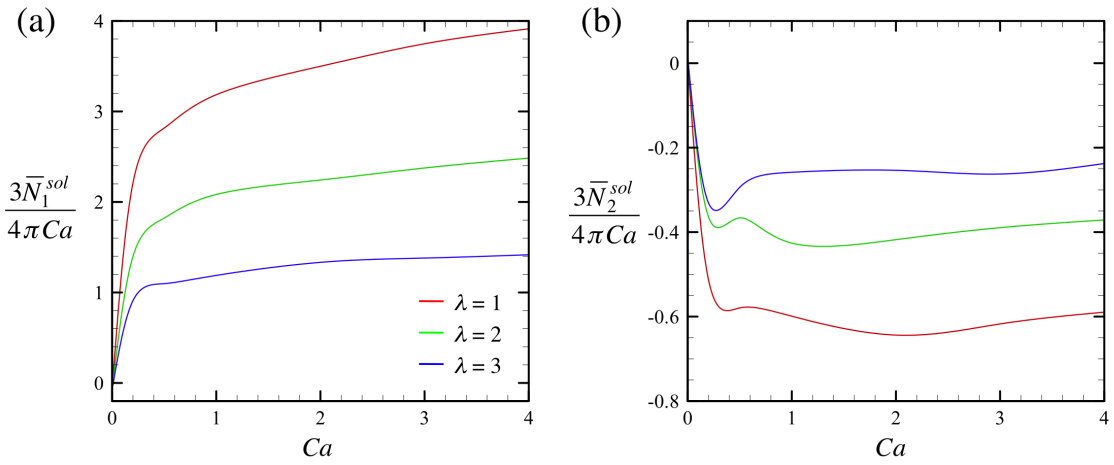

Fig. 5.28 First and second normal stress difference of the RBC suspension in shear flow. $\theta_0 = \pi/2$ in all cases.

N_2 becomes negative, respectively. The first and second normal stress difference N_i ($i = 1$ or 2) illustrate the visco-elastic behaviour of the RBC suspension in shear flow, i.e. non-Newtonian effects of the suspension in shear flow, because the normal stress difference N_i are always 0 in the case of a Newtonian fluid. The absolute values of N_i become large as λ decreases. Which suggests that the elasticity effects of a dilute suspension of RBCs become larger with smaller λ and larger Ca.

The ratio between the normal stress difference and the effective shear viscosity are also shown in figure 5.29. This value can be viewed as the ratio between effective elasticity and viscosity of the RBC suspension in shear flow. Due to the shear-thinning behaviour of the suspension, the effect of elasticity becomes large in high Ca regime. We again observe higher values of N_i/S_{12} with smaller λ. Then, we conclude that the elasticity effects of the dilute suspension become larger with smaller λ and larger Ca.

5.5 Conclusions

In this chapter, we investigated the kinematics and rheology of a single RBC in creeping shear flow and the results were applied to rheological properties of a dilute suspension of RBCs in shear flow. The RBC was modeled as a liquid capsule enclosed by a 2D hyper-elastic membrane. To express the area incompressibility of the RBC

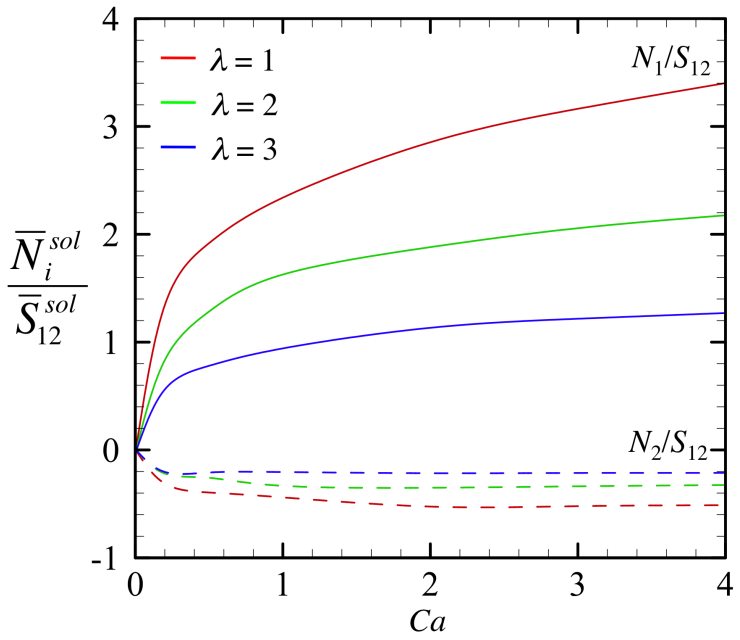

Fig. 5.29 The ratio between the normal stress difference and the effective shear viscosity.

membrane, the SK law with $C = 10$ was employed for the membrane. To solve the membrane mechanics, we used the finite element method. Due to the small size of the RBC, the flow was assumed as a Stokesian and the boundary integral equation of the flow field was solved by the boundary element method.

In very low Ca regime with $\theta_0 = \pi/2$, the RBC showed quasi-rigid like tumbling motion. In high Ca regime with $\theta_0 = \pi/2$, the RBC showed swinging motion. These results were consistent with former experimental observations and numerical computations of an RBC in shear flow. We also observed quasi-circular profiles of the RBC in the shear plane, and we defined such a motion as tumbling-swinging transition.

When the revolution axis of a spheroidal capsule, as well as the RBC type biconcave disk, was not initially located in the shear plane, the capsule showed reorientations. Steady orientation of the capsule depended on the strength and unsteadiness in the background flow. Given that the transition can be controlled by adjusting the background flow strength as well as the unsteadiness in the background flow direction, the results obtained here can be utilized for particle-alignment techniques in engineer-

ing applications, such as counting non-spherical particles by light scattering, making anisotropic materials, etc.

The large deformation of the RBC was suppressed by a strain-hardening property of the SK law. We also observed that the length in the x_3-axis L_3 decrease as L_1 increase to preserve the surface area of the membrane. Deformation of the RBC is strongly dependent on the membrane model, thus we again conclude that we need to choose a suitable membrane model to express the mechanical properties of biological membrane. The deformation also tended to be suppressed when the viscous effect inside the capsule becomes large, i.e. high λ condition. These results suggest that not only the shear rate but the viscosity ratio of the internal and external liquids dominate the deformation of the RBC in shear flow.

Distributions of the principal tensions change periodically together with the shape oscillation and the maximum tensions appeared on the side of the deformed RBC when $\theta_0 = \pi/2$, whereas the high isotropic tension only appeared at the top/bottom of the deformed RBC. The maximum principal tension should be correlated to the membrane rupture, and the isotropic tension should be correlated to the regulation of the mechano-transduction of the RBC, these regions are then important to understand the mechanisms of the hemolysis and the mechano-transduction of the RBCs. We also investigated the maximum and average tensions, $\max(\tau_{\max})$, $\max(\tau^p_{\max})$ and τ^p and $\bar{\tau}^p$, and these tensions increase monotonically with Ca even though the deformation is suppressed in high Ca regime. These findings on the membrane tension would be useful for better understanding of the mechanisms of the hemolysis and the mechano-transduction of RBCs.

The effective shear viscosity converged to 2.5 in the case of $\theta_0 = \pi/2$ and 4.3 in the case of $\theta_0 = 0$, respectively in very low Ca regime. We saw that the shear-thinning behaviour of the effective shear viscosity, which is consistent with former experimental observations of the RBC suspension. Surprisingly, the effective shear viscosity of the suspension became small with higher λ, because the hight of the deformed RBC became small with higher λ. Which is relevant to that a suspension with inner-viscous capsules has efficient fluidity in dilute regime. The diagonal components of the stresslet were no longer isotropic, then the first normal stress difference N_1 became

positive, whereas the second normal stress difference N_2 became negative, respectively. These results indicate that the visco-elastic properties of the RBC suspension does exist. The elasticity effects of the suspension become large with smaller λ and larger Ca. These findings presented here form a fundamental basis for the knowledge of complicated suspension mechanics of capsules and biological cells.

Chapter 6

Hydrodynamic interaction between two RBCs

6.1 Introduction

Suspensions of small capsules in liquids are common in nature and in several engineering field. Blood, for instance, is a dense suspension of red blood cells (RBCs) and its macroscopic suspension properties are strongly dependent on the microscopic cell behaviours [72]. Now, it is desirable to know how small RBCs respond to imposed forces or motions at their boundaries. When multiple RBCs are immersed in a liquid, the cell-cell interaction must be concerned. In the case of a suspension of RBCs in dilute to semi-dilute regime, probability that in a particular realization of the suspension there is one other cell within a certain distance of a given RBC is proportional to the volume fraction ϕ, and the probability of there being two RBCs in this region is proportional to ϕ^2 [12, 13]. Given that the first approximation to the effect of the cell-cell interaction may be obtained by considering only pairwise hydrodynamic interaction of RBCs. As a first step to tackle the problems of the cell-cell interaction of RBCs, we consider simple situation where only two RBCs interact in a simple shear flow. In last decades, many researchers have been investigated the hydrodynamic interaction of the RBCs in a tube or a rectangular channel, as well as the interaction with the other cells, such as platelets and white blood cells [4, 23, 30, 59, 72, 96]. However, detailed analysis of the pairwise interaction of the RBCs has not been performed, yet. This may be because that blood is a dense suspension of RBCs and the

pairwise interaction of the RBCs has not been featured. However, the pairwise interaction is important phenomenon, because the effects of cell-cell interaction can be described by it until ϕ^3 effects can be negligible. Which is relevant to that the effect of pairwise interaction can be used for the discussions of a suspension rheology up to $\phi \approx 0.1$, because ϕ^3 is 10 times smaller than ϕ^2. An RBC suspension with $\phi = 0.1$ is common in engineering field, such as in micro-fluidic devices. Thus, knowledge of the pairwise interaction of RBCs can be applied to many engineering field and will give us a fundamental basis of the suspension mechanics.

A number of researchers have investigated pairwise interaction of small rigid particles, drops, micro-organisms and capsules in shear flow [11, 38, 39, 47, 57]. Batchelor & Green [11] analytically investigated the hydrodynamic interaction of two non-Brownian rigid spheres in shear flow. They showed that trajectories of a given particle become symmetry and no displacement perpendicular to the flow direction is generated by the pairwise interaction. The symmetry of the pairwise interaction is broken by the deformability of particles. Loewenberg & Hinch [57] numerically investigated the pairwise interaction of drops in shear flow using a boundary element method. In the case of pairwise interaction of deformable drops, trajectories are no longer symmetry and the displacement was observed to both the velocity gradient and the vorticity directions. Lac et al. [47] numerically investigated the hydrodynamic interaction of two identical capsules in shear flow with a B-spline projection for the membrane and a boundary element method for the fluid mechanics. They showed that trajectories of deformable capsules are also asymmetry and the displacement to the perpendicular to the flow direction was observed. They also reported that the pressure between the two capsules significantly changes during the interaction and the capsule trajectories are strongly dependent on the pressure filed. Such irreversible displacements to the cross-flow direction produce the shear-induced self-diffusivity of deformable particles. Diffusion or dispersion of RBCs in fluid flow is important phenomenon, because it is relevant not only to the mixing or efficiency of the mass-transport but to the rheological properties of blood in microcirculation [34, 54, 61]. In section 6.3, we calculate the self-diffusion coefficients of the RBCs generated by the pairwise interaction. During the interaction, we neglect Brownian motion of RBCs. This treatment corresponds

to large Péclet number flow to the RBCs. In section 6.3.2, we discuss the effect of Brownian motion of the RBCs.

The hydrodynamic interaction between the RBCs also play important role on the membrane tension. Lac et al. [47] investigated the membrane tension of spherical capsules with various capillary number during the pairwise interaction. They reported that the maximum tension occurs in the equatorial region of the deformed shape of capsule in crossing regime. In separating regime, however, the region of high principal tension changes depending on capillary number. In high capillary number regime, the high principal tension appear the same area as for a single capsule, whereas a stress concentration located at the tips of the capsules in low capillary number regime. Even in the case of simple spherical capsule, the effects of the interaction on the membrane tension are complicated and it would be much more complicated in the case of the RBC type biconcave disk. Flow-induced deformation of RBCs affects the cell ability to release various molecules and regulate their concentration in blood [34]. In addition, high stress level is correlated to cause of membrane rupture. For better understanding the physiology and pathology of the RBCs in a suspension, detailed analysis of the membrane tension of the RBCs during the interaction are needed.

To construct a continuum rheological model of the small particle suspension, Batchelor (1970) analytically introduced the particle stress tensor of the suspension. When a suspension is so dilute that the fluid motion near each RBC is effectively independent of the existence of other RBCs, the particle stress tensor can be approximate from the solitary cases, whose order is equivalent to ϕ. For larger ϕ, but still $\phi \ll 1$, the effect of hydrodynamic interaction of the RBCs must be allowed for. Assume that isotropic structures of a suspension, the first approximation to the effect of the hydrodynamic interaction of RBCs may be obtained by considering only pairwise interaction of RBCs. Batchelor et al. [12] corrected the leading order approximation of the stresslet to order ϕ^2 with the effect of pairwise interaction of particles. In section 6.4.2, we investigate the effect of the pairwise interaction to the stresslet of the RBCs subjected to various capillary number and viscosity ratio in simple shear flow.

6.2 Problem statement

An RBC is modeled as a capsule with a hyper-elastic membrane with surface shear elastic modulus G_s and area dilation modulus K_s. The SK law with $C = 10$ is employed for the membrane to express the area incompressibility of the RBC membrane. The finite element method is used to solve the membrane mechanics. Consider two RBCs are filled with a Newtonian fluid with density ρ and viscosity $\lambda\mu$ and freely suspended in another Newtonian fluid with the same density ρ but viscosity μ and subjected to a simple shear flow in with shear rate $\dot{\gamma}$ in the (x_1, x_2)-plane. Due to the small scale of the RBC, we also assume that flow is a Stokesian, i.e. inertia free, and the flow is solved by the boundary element method. Capillary number is also defined as $Ca = \mu\dot{\gamma}\ell/G_s$, where ℓ is the radius of the sphere with the same volume as the RBC type biconcave disk. Throughout this chapter, we use a linear element with 1280 or 5120 meshes for the membrane.

Denoting the centres of mass of the RBCs G_1 and G_2, we use a Cartesian system centred on the middle O of $\underline{x}^0\,(\mathrm{G}_1) - \underline{x}^0\,(\mathrm{G}_2)$ (cf. figure 6.1(a)), where $\underline{x}^0$ is the initial position of the RBC. In this system, the undisturbed background flow $\underline{v}^\infty$ is given by

$$v_1^\infty = \dot{\gamma} x_2, \qquad v_2^\infty = v_3^\infty = 0. \tag{6.1}$$

To describe the positions of two RBCs efficiently, we define the relative position vector $\underline{\Delta x}$:

$$\underline{\Delta x} = \underline{x}\,(\mathrm{G}_1) - \underline{x}\,(\mathrm{G}_2)\,. \tag{6.2}$$

The RBC centres G_1 and G_2 are initially located at position $\pm\underline{\Delta x}^0/2$. In this study, Δx_1^0 and Δx_2^0 always have opposite signs, so that the RBCs are naturally convected towards each other by the flow and we set Δx_1^0 to a negative value. To eliminate the initial deformation of the RBCs during the interaction, the absolute values of Δx_1^0 should be large enough. We use the following equation to determine the initial position of the RBCs: $|x_2^0|/|x_1^0| \leq \epsilon$. In this study, the threshold value is set as 0.025. Which value is small enough that results obtained in this chapter are unaffected qualitatively by the selection of ϵ if it is sufficiently small, which is numerically confirmed by comparing with $\epsilon = 0.02$ (data not shown).

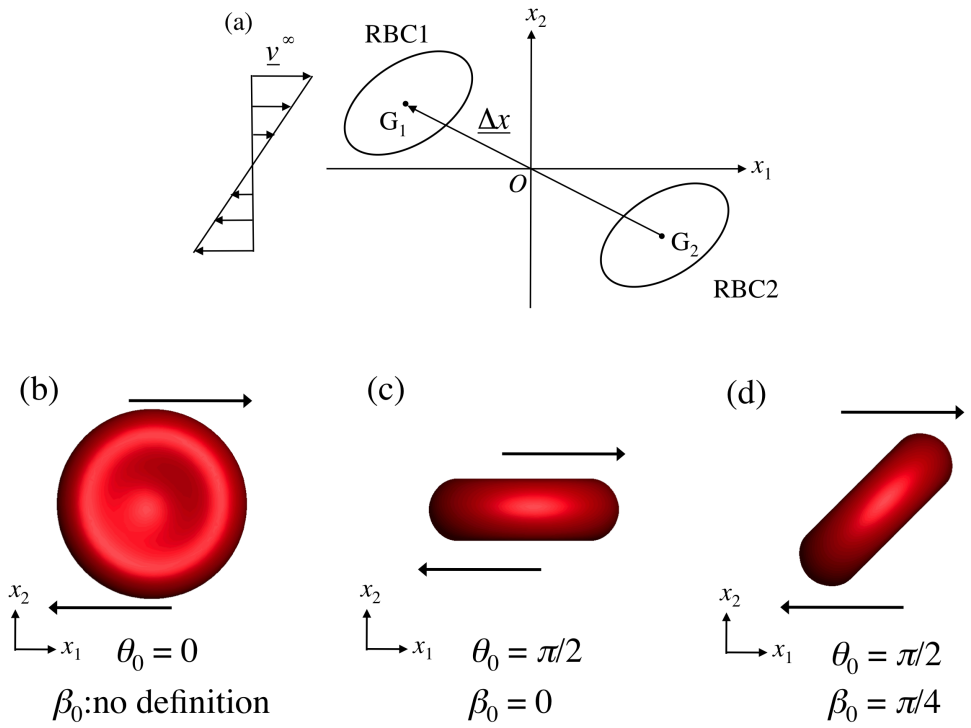

Fig. 6.1 Representation of the RBCs position and orientation. (a) Schematic illustration of the relative position of the RBCs in the shear plane (x_1, x_2). Orientation of the RBC in the shear plane, for instance: (b) $\theta_0 = 0$, (c)$\theta_0 = \pi/2$ and (d)$\beta_0 = \pi/4$. θ_0 is defined as the angle between the revolution axis of the RBC and the x_3-axis at $t = 0$. β_0 is defined as the angle between the major axis of the RBC in the shear plane and the x_1-axis at $t = 0$. Arrows in the figure represent the background shear flow.

The biconcave disk shape, which is assumed as the reference shape of the RBC, is strongly anisotropic, then we must consider its orientation when the RBC is subjected to shear flow. To discuss the orientation efficiently, we define two angles θ_0 and β_0. The angle θ_0 is defined as the angle between the revolution axis of the biconcave disk and the x_3-axis at $t = 0$ (cf. figure 6.1(b) and (c)). The angle β_0 is the initial inclination angle of the RBC, i.e. the angle between the major axis of the RBC in the shear plane and the x_1-axis at $t = 0$ (cf. figure 6.1(d)). When $\theta_0 = 0$, the angle β_0 can be omitted, because the material properties are no longer asymmetry towards flow direction. Moreover, we define the relative angle difference $\Delta\beta_0$ as $\Delta\beta_0 = \beta_0^1 - \beta_0^2$, where β_0^α is β_0 of the α-th RBC. For simplicity of the problem, β_0^2 is fixed to $\beta_0^2 = 0$, for all cases. In a dilute suspension, the difference of angle θ_0 between the two RBCs

may be omitted, because the orientation of a single RBC in shear flow is converged to $\theta_0 = 0$ or $\pi/2$ in a certain range of Ca, as shown in chapter 5. Then, we do not consider the angle difference of θ_0 between the two RBCs.

Consider now macroscopic suspension properties of RBCs. In self-diffusion, a single marked RBC executes a random walk in a suspension at a uniform concentration. The cross-flow self-diffusion is defined as half the rate-of-change of the random walk variance [57]:

$$\underline{\underline{\mathscr{D}}} = \lim_{t\to\infty} \frac{1}{2t} \langle \underline{\Delta}(t) \otimes \underline{\Delta}(t) \rangle, \tag{6.3}$$

where $\underline{\Delta} = (\delta x_2, \delta x_3)$ is the random walk displacement in the cross section of the shear flow, i.e. in the (x_2, x_3)-plane. We consider a semi-dilute suspension ($\phi \ll 1$) with a uniform concentration. Let n be the number density of the RBCs in the suspension and so the volume fraction is $\phi = \frac{4\pi}{3}\ell^3 n$. Assume that there are no long-range correlations in the suspension, so that the probability distribution of RBC is uniform in space when they are far upstream and each collisions is uncorrelated. The rate of interactions that result in a particular cross-flow displacement is proportional to relative approaching velocity $2\dot{\gamma}|x_2^0|$ and number density n. Neglect Brownian motion of the RBC, the self-diffusion coefficient is given by [57]:

$$\mathscr{D}_{ii} = \frac{1}{2} \int_{-\infty}^{\infty} \int_{0}^{\infty} 2(\delta x_i)^2 n \dot{\gamma} |x_2^0| dx_2^0 dx_3^0 \qquad (i = 2, \text{ or } 3). \tag{6.4}$$

Due to the symmetry of the problem, the integration range is reduced to the first quadrant and non-dimensional cross-flow self-diffusion coefficient is given by

$$\frac{\mathscr{D}_{ii}}{\phi \dot{\gamma} \ell^2} = \frac{3}{2\pi} \int_{0}^{\infty} \int_{0}^{\infty} (\delta x_i)^2 |x_2^0| dx_2^0 dx_3^0 \qquad (i = 2, \text{ or } 3). \tag{6.5}$$

Next, we consider particle stress tensor of the RBC suspension in semi-dilute regime. In very dilute regime, the particle stress tensor can be described by the stresslet of single RBC in viscous flow. To seek the next order term of the particle stress tensor, the effect of hydrodynamic interaction of the RBCs must be allowed for. In semi-dilute regime, the probability of there being two RBCs in a given region is proportional to ϕ^2. Given that the effects of cell-cell interaction may be obtained by the summation of the pairwise interaction of the RBCs. Batchelor et al. [12] analytically introduced

the ϕ^2 term of the particle stress tensor with pairwise interactions as follow:

$$\underline{\underline{\Sigma}}^{(p)} = \frac{3\phi}{4\pi\ell^3}\,\underline{\underline{S}}^{sol} + \frac{9\phi^2}{16\pi^2\ell^6}\int_0^\infty \left(\langle \underline{\underline{S}} \rangle - \underline{\underline{S}}^{sol}\right)\; dV + O(\phi^3), \tag{6.6}$$

where dV is the finite volume of the suspension. The integrand of the second term represents the stress variation due to the pairwise interaction. In general, the above integral is not absolutely convergent, because the stresslet generated by a point force with a certain distance r is reduced as $1/r^3$ when $r \gg \ell$ and the infinite integral is diverged as fast as $\ln r$. Batchelor et al. [12] avoided such integral divergence by recasting the ensemble average before reducing it to an average over the separation of spheres. This method is based on the relation:

$$\underline{\underline{S}}^{sol} = \frac{4\pi \int_{\underline{x}^0}^\infty \underline{\underline{S_i}}(\underline{x}^0, \underline{r}) r^2 dr}{4\pi \int_{\underline{x}^0}^\infty r^2 dr}, \tag{6.7}$$

where $\underline{\underline{S_i}}(\underline{x}^0, \underline{r})$ is the stresslet of a given particle i located on $\underline{x}^0$ and the other particle is located on $\underline{x}^0 + \underline{r}$. In the case of a rigid spherical particle, the above relation is exactly satisfied, because the stresslet is a function of only the rate of strain $\underline{\underline{e}}(\underline{x}^0, \underline{r})$ and $\underline{\underline{S}}^{sol}$ can be determined only from bulk average rate of strain $\underline{\underline{E}}$ $(= \frac{1}{V}\int \underline{\underline{e}}(\underline{x}^0, \underline{r}) dV)$. In the case of non-spherical particles, deformable drops, and also capsules, equation (6.7) may not be satisfied due to the time and orientation dependencies of them. Then, another treatment for the integral divergence may be needed for the RBCs. In this study, the integration of the right hand side of (6.6) is conducted only from in near-field interactions.

6.3 Self-diffusion of RBCs in a semi-dilute suspension

6.3.1 Trajectories

We first investigate trajectories of the RBCs in shear flow with various orientation, Ca and λ conditions. Time sequence of the RBCs in the shear plane during the interaction with $Ca = 0.5, 1.0$ and 2.0 are shown in figures 6.2(a), (b) and (c), respectively. $\lambda = 1$, $\theta_0 = \pi/2$ and $\Delta\beta_0 = 0$, for all cases. Initial positions are set to $\Delta x_1^0/2\ell = 10$, $\Delta x_2^0/2\ell = 0.25$, and $\Delta x_3^0/2\ell = 0$. Then, the centre of mass G_1 and G_2 are always in

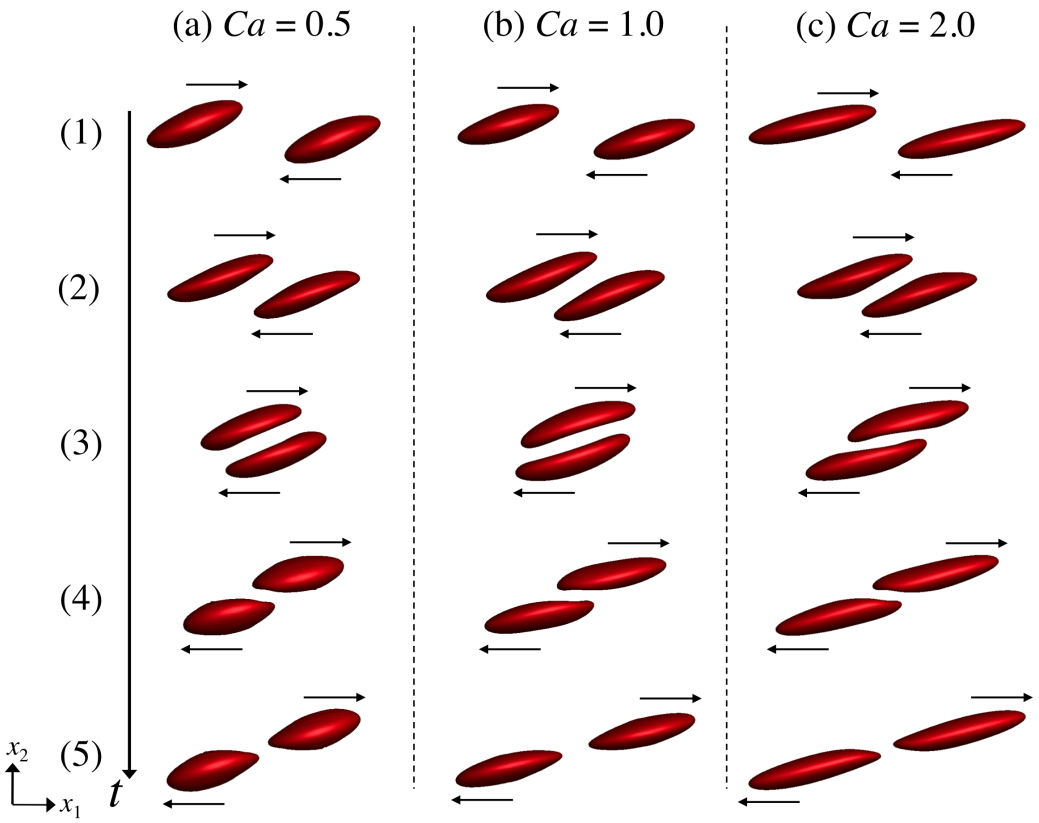

Fig. 6.2 Time sequence of the interaction of RBCs in the shear plane with (a) $Ca = 0.5$, (b) 1.0 and (c) 2.0. For all cases, $\lambda = 1.0$, $\theta_0 = \pi/2$ and $\Delta\beta_0 = 0$. Initial positions are set to $\Delta x_1^0/2\ell = -10$, $\Delta x_2^0/2\ell = 0.25$, and $\Delta x_3^0/2\ell = 0$. Numbers appeared in the figure are numbering of the time sequence. Arrows in each figure are also indicate that flow directions.

the shear plane. The deformed shape of a single RBC in shear flow is symmetrical with respect to its centre. Thus, the appearance of asymmetry profile coincides with the onset the hydrodynamic interaction between two RBCs. When the RBCs start to interact each other (cf. figure 6.2(2)), the shapes are no longer symmetrical with respect to its mass centre. When the RBCs are in crossing regime (cf. figure 6.2(3)), the centre of mass are shifted across the streamlines and the membrane in contact side become concave. After crossing, the membrane gradually recover from concave shape to symmetrical shape (cf. figure 6.2(4)). When the RBCs are in separation regime (cf. figure 6.2(5)), large curvatures appear at the tip of the deformed membrane. These tendencies are the same as the numerical results of spherical capsules in shear flow

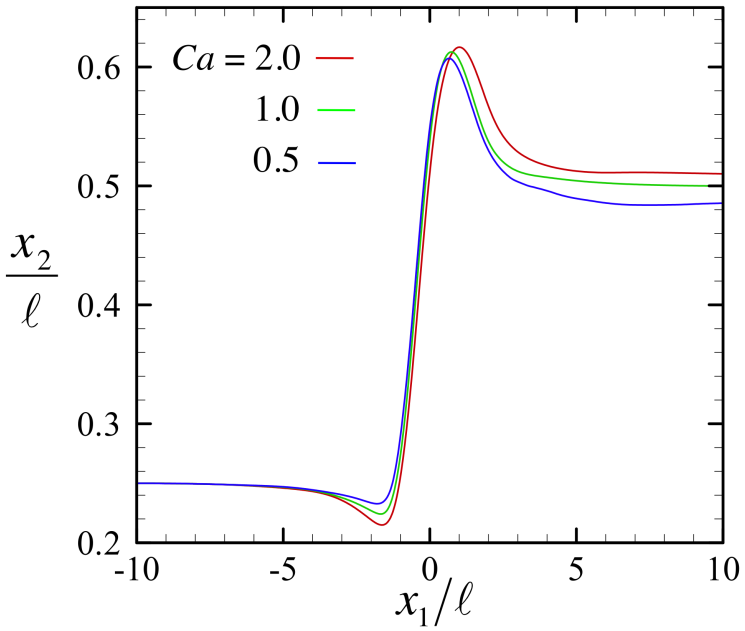

Fig. 6.3 Trajectories of the centre of mass G_1 with $Ca = 0.5$, 1.0 and 2.0. Numerical conditions are the same as figure 6.2.

[47]. In all cases, the RBCs are always separate and do not contact each other.

We track the centre of mass G_1 with respect to time and its trajectories are shown in figure 6.3. Numerical conditions are the same as figure 6.2. When the RBCs start to interact each other, the position x_2 become once small. After that, in crossing regime, x_2 become maximum. In separation regime, x_2 gradually decrease as x_1 increase, but they do not reach the initial values of x_2. After the interaction, the trajectories become steady. In the limiting case of $Ca \to 0$, the RBCs behave as the rigid body, whose trajectories in Stokes flow are symmetry during the pairwise interaction. Deformability of the RBCs is then cause of the asymmetric trajectories as shown in the figure.

To investigate the hydrodynamic interactions more efficiently, it is useful to compute pressure of the flow field p. Pressure at a point $\underline{x}$ in outer fluid is given by [68]

$$p(\underline{x}) - p^{\infty} = -\frac{1}{8\pi}\int_S \underline{q}(\underline{y}) \cdot \underline{P}(\underline{x},\underline{y}) dS(\underline{y}) + \frac{1-\lambda}{8\pi}\mu \int_S \underline{v}(\underline{y}) \cdot \underline{\underline{\Pi}}(\underline{x},\underline{y}) \cdot \underline{n}(\underline{y}) dS(\underline{y}), \quad (6.8)$$

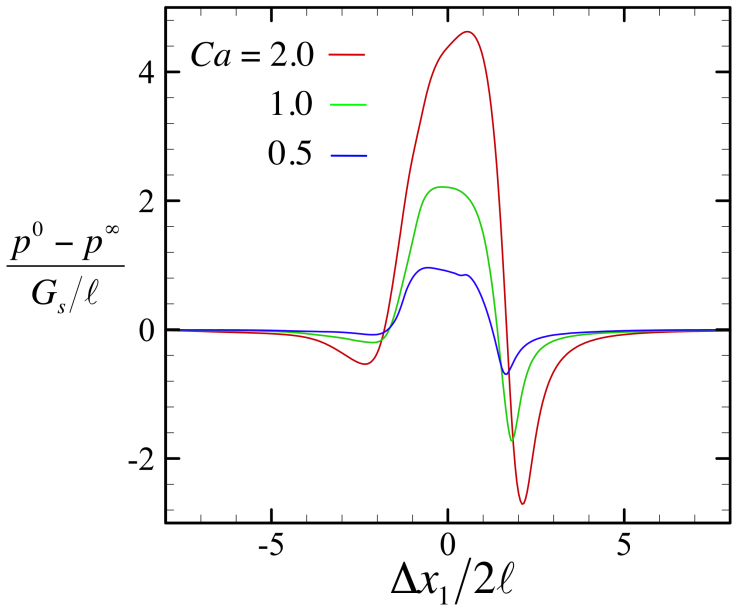

Fig. 6.4 Pressure at the origin O. p^0 is the pressure at the origin and p^∞ is the far field pressure. Numerical conditions are the same as figure 6.2.

where

$$P_i = 2\frac{r_i}{r^3}, \qquad \Pi_{ij} = 4\left(-\frac{\delta_{ij}}{r^3} + 3\frac{r_i r_j}{r^5}\right), \tag{6.9}$$

and p^∞ is the far field pressure. Pressure at the origin O with $Ca = 0.5, 1.0$ and 2.0 are shown in figure 6.4. When the RBC start to interact each other, the pressure become negative, then the RBCs are suction to the origin (cf. figure 6.3). In crossing regime, the high pressure appeared. Such a high pressure field produces the concave shape of the RBCs in crossing regime (cf. figure 6.2(3)). In separation regime, on the other hand, the pressure becomes negative rapidly and takes the minimum value. In this regime, the RBCs have the high curvature of the membrane at the tips, as shown in figure 6.2(5). From these results, we see strong correlations between the pressure filed and the hydrodynamic interaction of the RBCs.

Next, we investigate the effect of the viscosity ratio λ on the hydrodynamic interactions. Profiles of the RBCs during the interaction with $\lambda = 0.5, 1.0$ and 2.0 are shown in figures 6.5(a), (b) and (c), respectively. For all cases, $Ca = 1.0$, $\theta_0 = \pi/2$ and $\Delta\beta_0 = 0$. The initial positions are the same as figure 6.2. When the RBCs are

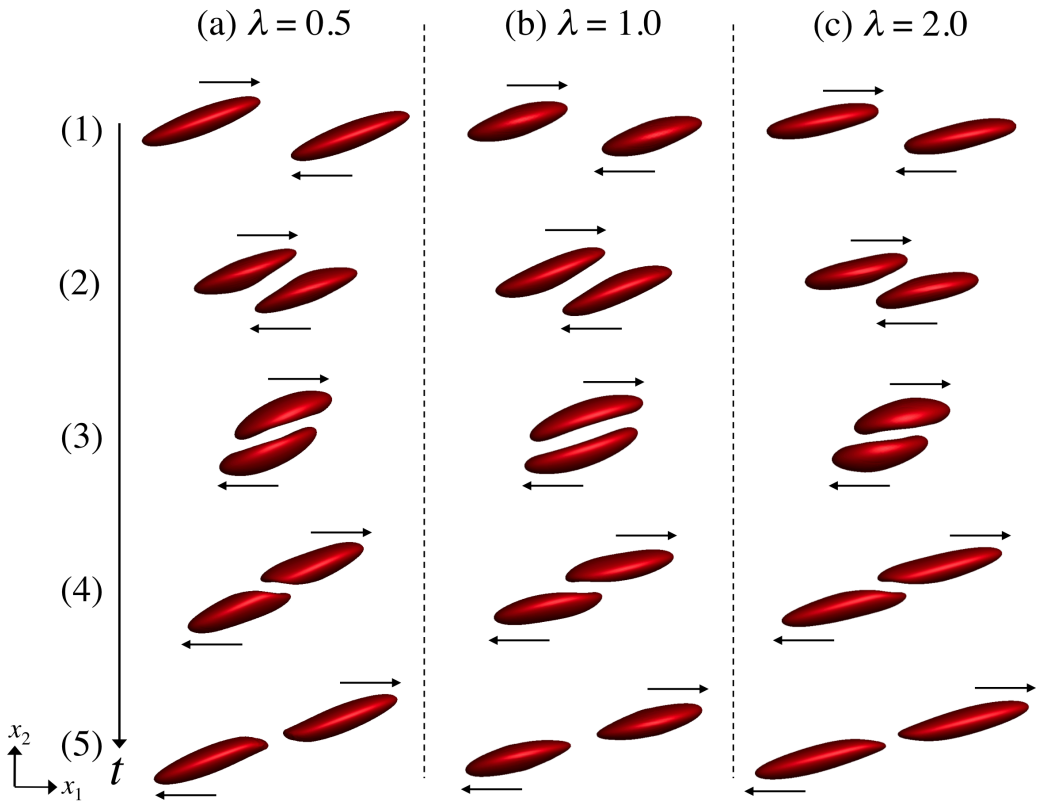

Fig. 6.5 Time sequence of the interaction of RBCs in the shear plane with (a) $\lambda = 0.5$, (b) 1.0 and (c) 2.0. For all cases, $Ca = 1.0$, $\theta_0 = \pi/2$ and $\Delta\beta_0 = 0$. The initial positions are the same as figure 6.2. Numbers appeared in the figure are numbering of the time sequence. Arrows in each figure are also indicate that flow directions.

in crossing regime, the centre of mass more shifted across streamlines with lower λ to overcome another cell. This is because the inclination angle increases as λ decreases, as shown in figure 5.4(c), and need to more deform or move to perpendicular to the flow in lower λ cases.

To investigate the effect of λ more in detail, trajectories of G_1 with various λ are shown in figure 6.6. Numerical conditions are the same as figure 6.5. We again see the asymmetrical curves during the interaction. Displacement towards the x_2-direction decreases as λ increases. In the limiting case of $\lambda \to \infty$, capsules will behave like rigid particles, then the trajectories will be symmetric. The trajectories are strong function of the viscosity ratio λ, which are moderate on Ca (cf. figure 6.3 and figure

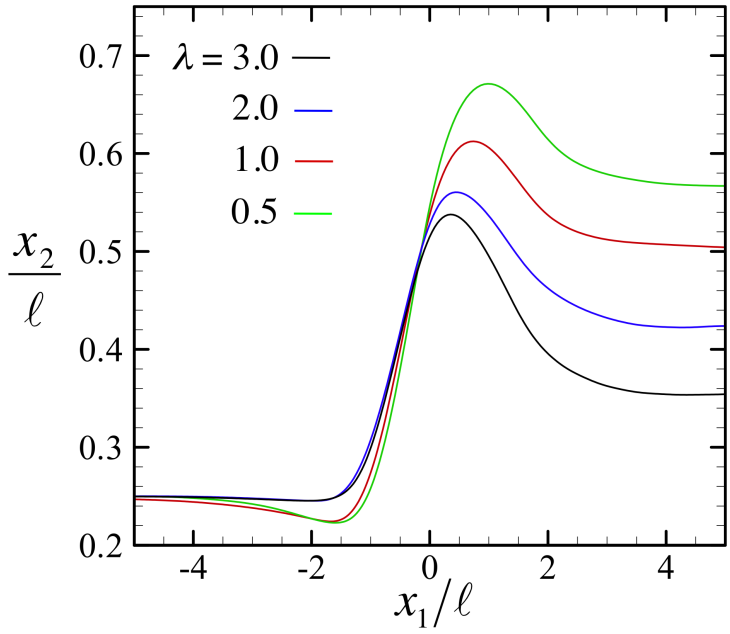

Fig. 6.6 Trajectories of G_1 with various λ. Numerical conditions are the same as figure 6.5 in all cases.

6.6). This result suggests that the trajectories during the hydrodynamic interaction between the two RBCs are dominant significantly to λ and moderately to Ca.

Next we investigate the effect of angle difference $\Delta\beta_0$ on the RBCs trajectories. Time sequence of the interaction of RBCs in the shear plane with $\Delta\beta_0 = 0, \pi/6$, and $\pi/2$ are shown in figure 6.7. For all cases, $\lambda = 1.0$, $\theta_0 = \pi/2$ and $Ca = 2.0$. Initial positions are set to $\Delta x_1^0/2\ell = -10$, $\Delta x_2^0/2\ell = 0.25$, and $\Delta x_3^0/2\ell = 0$. Shapes of the RBCs during the interaction are dependent on $\Delta\beta_0$, but we do not see the significant change of trajectories among the three $\Delta\beta_0$ cases.

Trajectories of G_1 with various orientations ($\Delta\beta_0 = 0, \pi/6, \pi/2$, and $2\pi/3$; $\theta_0 = 0$ and $\theta_0 = \pi/2$) are shown in figure 6.8. Ca is set to 2 and λ is equal to 1, in all cases. Initial positions are the same as figure 6.7. From this figure, we see that all trajectories are almost overlapped. Which is relevant to that the trajectories of the RBC during the hydrodynamic interaction are independent of the angle and orientation of the RBCs. It is also found that the displacements towards the x_3-direction are almost

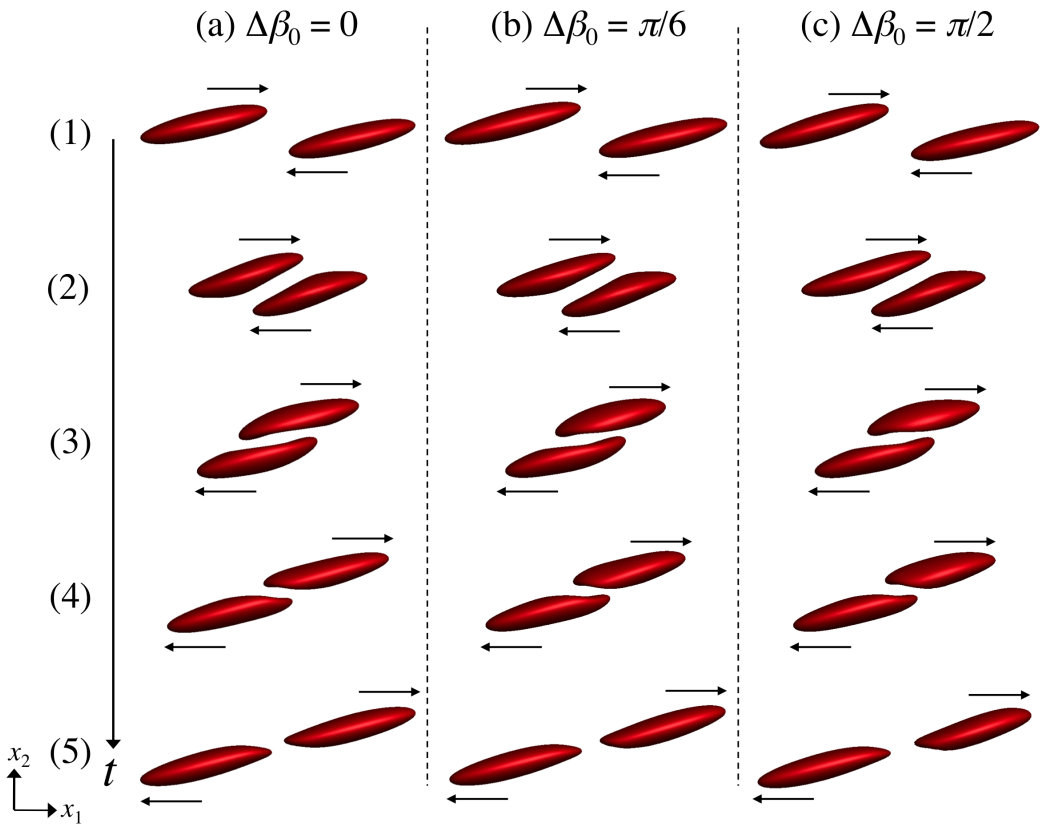

Fig. 6.7 Time sequence of the interaction of RBCs in the shear plane with $\Delta\beta_0 = 0, \pi/6$, and $\pi/2$. For all cases, $\lambda = 1.0$, $\theta_0 = \pi/2$ and $Ca = 2.0$. Initial positions are set to $\Delta x_1^0/2\ell = -10$, $\Delta x_2^0/2\ell = 0.25$, and $\Delta x_3^0/2\ell = 0$. Numbers appeared in the figure are numbering of the time sequence. Arrows in each figure are also indicate that flow directions.

independent of the angle difference $\Delta\beta_0$ and the orientation θ_0 (data not shown). This may be because that the RBCs do not close so much each other during the interaction and they can easily pass away another cell, thus the trajectories are likely independent of the angle and orientation of the RBCs. For the simplicity, the initial orientation of the RBCs are fixed to $\theta_0 = \pi/2$ and $\Delta\beta_0 = 0$ to determine the self-diffusivity of the RBCs in the next section.

6.3.2 Shear-induced self-diffusion coefficient

In this section, we investigate the cross-flow self-diffusivity of the RBC suspension in semi-dilute regime. Before calculating the self-diffusion coefficient of the RBCs in

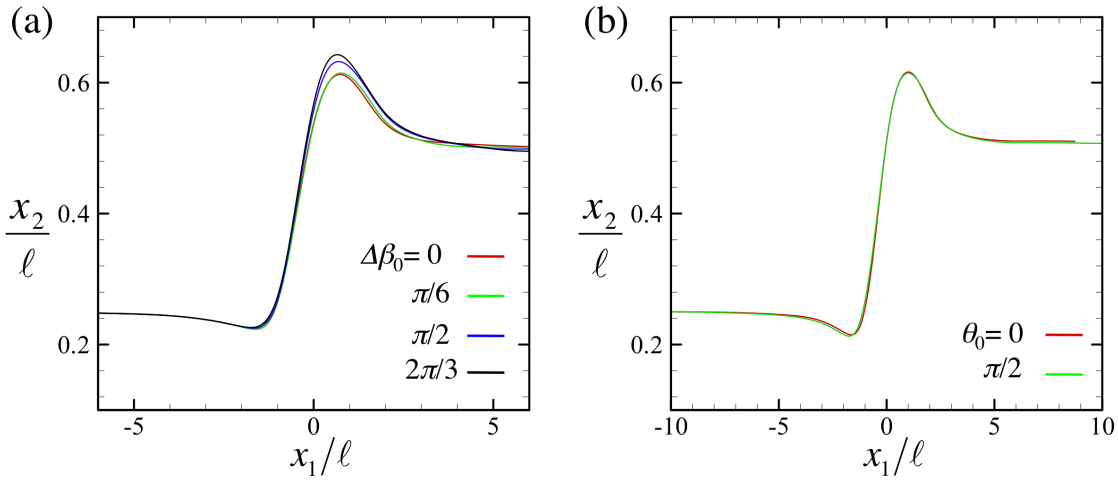

Fig. 6.8 Trajectories of G_1 with various orientations: (a) $\Delta\beta_0 = 0, \pi/6, \pi/2$, and $2\pi/3$; (b)$\theta_0 = 0$ and $\theta_0 = \pi/2$. $Ca = 2$, $\lambda = 1$ are used in all cases. Initial positions are the same as figure 6.7.

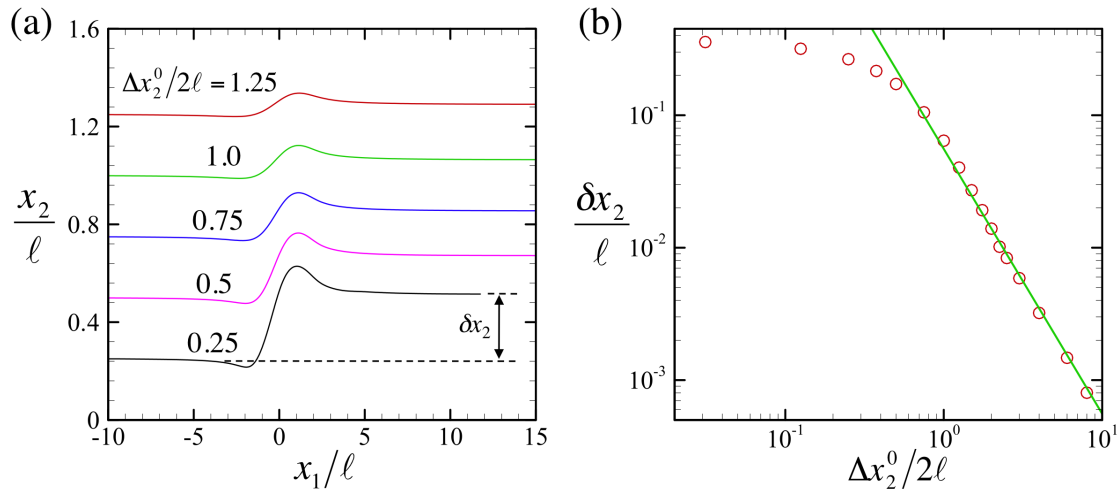

Fig. 6.9 Trajectories and displacement δx_2 of the mass centre G_1 with various initial relative potion Δx_2^0.

shear flow, we investigate the effect of the initial position on the interaction of the two RBCs. In figure 6.9(a), trajectories of G_1 with various initial relative position Δx_2^0 are shown. $Ca = 2.0$ and $\lambda = 1.0$ in all cases. The effect of interaction between the RBCs decreases as Δx_2^0 increases. We define displacement towards the x_2-direction in the steady state as δx_2, as shown in figure 6.9(a). We see that the displacement δx_2 decreases as Δx_2^0 increases. To investigate the effect of Δx_2^0 more in detail, δx_2 as a function of Δx_2^0 in log-log scale are plotted in figure 6.9(b). In far-field displacement $(\Delta x_2^0/2\ell) > 1$, the displacement δx_2 decreases as quasi-linear with respect to $\Delta x_2^0/2\ell$. The green line in figure 6.9(b) represents linear fitting line with its slope -2. Loewenberg & Hinch (1997) numerically investigated the hydrodynamic interaction between two deformable drops and they showed the scaling of δ_2 with respect to the relative position of drops in the (x_2, x_3)-plane. According to their work, we estimate the scaling of δ_2 with respect to the relative position in the (x_2, x_3)-plane: For widely separated neutrally-buoyant RBCs, the cross flow velocity is $d\Delta/dt \propto (R/r)r^{-2}$, where $r \approx \left[R^2 + (\Delta x_1)^2\right]^{1/2}$ is the cell separation, Δx_1 is the component of separation in the flow direction and $R = \left[(\Delta x_2^0)^2 + (\Delta x_3^0)^2\right]^{1/2}$ is the initial cross-flow separation. If we assume $dx_1/dt \sim R$, we obtain $d\Delta/dx_1 \propto r^{-3}$. Integrating zero to infinity with respect to x_1, we obtain the estimation $\Delta \propto -R^{-2}$ when $R \gg 1$. The numerical results shown in figure 6.9(b) are then consistent with the above scaling estimation.

We now seek for the self-diffusion coefficient of the RBCs in shear flow. To calculate the self-diffusion coefficient of the RBCs, we use the G_1 trajectories and displacement $\underline{\delta x}$ with various initial potions in the (x_2, x_3)-plane. To efficiently compute equation (6.5), we introduce the polar coordinate (r, ψ) centred on the origin O. Equation (6.5) then can be written as

$$\frac{\mathscr{D}_{ii}}{\phi\dot{\gamma}\ell^2} = \frac{3}{2\pi}\int_0^{\infty}\int_0^{\pi/2} (\delta x_i)^2 r^2 \sin\psi dr d\psi \qquad (i = 2, \text{ or } 3). \tag{6.10}$$

To compute the above infinite integration, it is divided into two parts with respect to

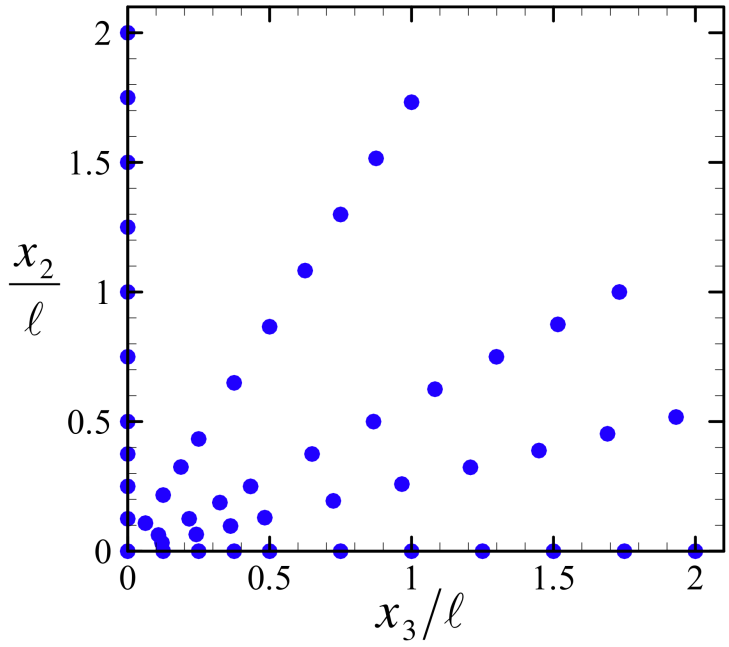

Fig. 6.10 Initial positions of integrand trajectories. Note: In the case of $x_2/\ell = 0$, the integrand function should be zero and do not calculate the trajectories.

the distance r:

$$\frac{3}{2\pi}\int_0^{\infty}\int_0^{\pi/2}(\delta x_i)^2 r^2 \sin\psi dr d\psi = \frac{3}{2\pi}\int_0^{r_c}\int_0^{\pi/2}(\delta x_i)^2 r^2 \sin\psi dr d\psi + \frac{3}{2\pi}\int_{r_c}^{\infty}\int_0^{\pi/2}(\delta x_i)^2 r^2 \sin\psi dr d\psi, \quad (6.11)$$

where r_c is the domain truncation. In far-field interaction ($\Delta x_2^0/2\ell > 1$), the displacement δx_2 decreases as r^{-2}, as shown in figure 6.9(b). We then assume that δx_i decreases proportional to r^{-2} when $r \geq r_c$. Accordingly, the second term in the right hand side of (6.11) is derived by asymptotic form and analytically calculated. To compute the first term in the right hand side of (6.11), we use a Gaussian numerical integration scheme with bi-linear element. The number of Gauss point in each element is 25 in all cases. The vertex of each element corresponds to the initial position of G_1 in the (x_2, x_3)-plane. We numerically check the domain truncation error by comparing the results of $r_c/\ell = 2.0$ and $r_c/\ell = 2.25$. 50 and 55 trajectories are used for the comparison, respectively. Results between the two cases differ less than 2%

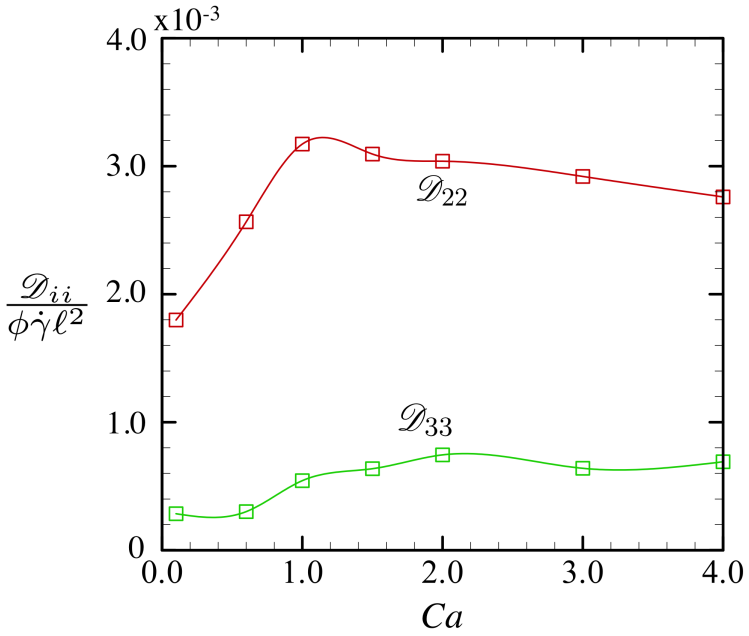

Fig. 6.11 Self diffusion coefficient with various Ca conditions. $\lambda = 1.0$ in all cases.

(data not shown) and we confirm that $r_c/\ell = 2.0$ is high enough that results obtained in this chapter are unaffected qualitatively by the selection of r_c. Besides, we investigate the numerical accuracy by comparing the results of 50 and 60 trajectories with $r_c/\ell = 2.0$. Difference between the two cases is less than 1% (data not shown), then we decide to use 50 trajectories for the numerical integration as shown in figure 6.10.

Non-dimensional shear-induced self-diffusion coefficient of the RBCs with various Ca are shown in figure 6.11. The viscosity ratio λ is unity in all cases. As indicated in the figure, $\mathscr{D}_{22}$ (red line in the figure) is always larger than $\mathscr{D}_{33}$ (green line in the figure). This is because the displacement towards the x_2-direction is always larger than the displacement towards the x_3-direction. This tendency is consistent with former numerical studies of the pairwise interaction of drops in shear flow [57] and a semi-dilute suspension of spheres with shear flow [39]. We also observe $\mathscr{D}_{22}$ has a peak value when $Ca \simeq 1$. The trajectories of pairwise interaction of the RBCs are asymmetric, due to the deformability of the membrane. The displacement δx_2 then increases as Ca increases in the near-field, as shown in figure 6.3. In the far-field, however, the displacement δx_2 slightly decreases as Ca increases, which may

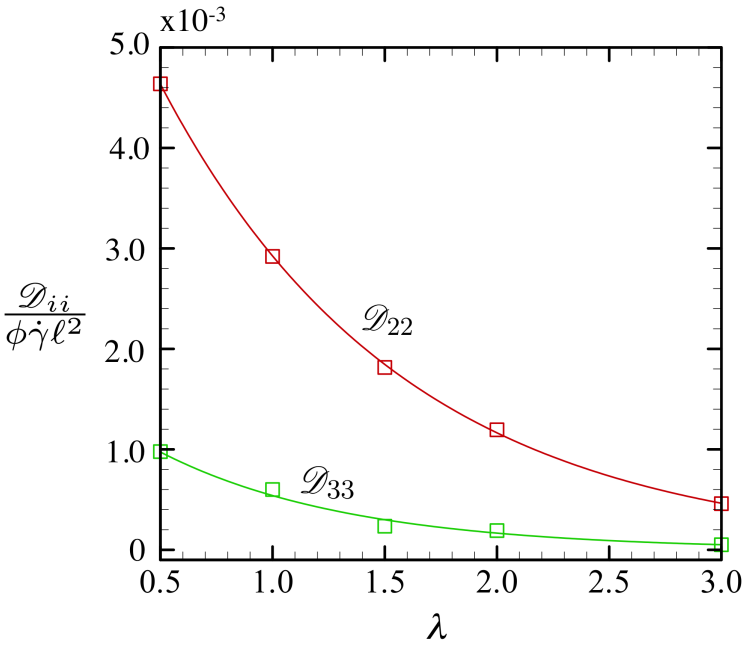

Fig. 6.12 Self diffusion coefficient with various λ conditions. $Ca = 3.0$ in all cases.

result of a balance between the negative pressure between the RBCs in separating regime and the shift of mass centre in crossing regime. The curve of $\mathscr{D}_{22}$ result from a balance between the effect of the near-field interaction and the far-field interaction. $\mathscr{D}_{33}$ is almost independent of Ca and the curve becomes almost plateau. These results suggest that diffusivity of the RBCs in a semi-dilute suspension is no longer isotropic and we must consider the individual behaviour of RBCs in fluid flow to determine the macroscopic self-diffusivities of RBCs.

Next, we investigate the effect of the viscosity ratio λ on the self-diffusion coefficient of the RBC and the results are shown in figure 6.12. $Ca = 3.0$ in all cases. The curves of $\mathscr{D}_{22}$ and $\mathscr{D}_{33}$ are decrease as λ increases, which suggests that the self-diffusivities of the RBCs are a strong function of the viscosity ratio. Compare between the effects of Ca and λ on the self-diffusivity of the RBCs (cf. figures 6.5 and 6.6), both $\mathscr{D}_{22}$ and $\mathscr{D}_{33}$ are strongly dependent on λ but moderately on Ca.

Loewenberg & Hinch [57] numerically investigated the pairwise interaction of drops and discussed the self-diffusion of the drops. The diffusion coefficients of drops were

also strongly dependent on the viscosity ratio λ but moderately on Ca. Besides, the curve of $\mathscr{D}_{22}$ has a peak in a certain value of Ca. They also showed that $\mathscr{D}_{22}$ of drops were always larger than $\mathscr{D}_{33}$. These tendencies are similar to our numerical results of RBCs, thus the self-diffusion of drops and capsules are similar in qualitatively. The typical values of self-diffusion coefficients of drops, however, became about 10 times larger than our numerical results. The interfacial velocity is determined by the surface load $\underline{q}$ both drops and capsules. The surface load is, however, a function of the surface tension in the case of drops but a function of elastic tension in the case of capsules. This qualitative difference of the load likely cases of the quantitative difference of the diffusivity of drops and capsules.

Next, we compare the results with experimental observations. Lima et al. [54] investigated the self-diffusion of the RBCs with various hematocrit ϕ in a glass capillary using micro-PTV systems. The diameter of the capillary was 100 μm and Dextran40 was used for the working fluid. The viscosity and density of the Dextran40 are $\mu =$ 3.8 (mPa.s) and $\rho = 1.046 \times 10^3$ (kg/m^3) at 37(°C), respectively. Flow rate was controlled by syringe pomp in the experiments and the Reynolds number was determined to 0.005. If we assume a Hagen-Poiseuille flow in the glass capillary, average velocity is estimated as $U = 1.9 \times 10^{-4}$ (m/s). In the above experimental conditions, the experimental results of non-dimensional radial dispersion of RBCs are estimated as $\mathscr{D}_{22}/(\phi U \ell) = 3.1 \times 10^{-2}$ ($\phi = 0.03$). The characteristic length $\ell = 2.82 \times 10^{-6}$ (m) [27] was used in the above estimation. Typical our numerical results are the order of 10^{-3} (cf. figures 6.11 and 6.12), which is 10 times smaller than the results of Lima et al.. When RBCs were subjected to tube flow, each individual cells tended to migrate to radial direction and RBCs were concentrated around the tube centre in their experiment and the local hematocrit in the cross-section of the tube is no longer isotropic. Then, the hydrodynamic interaction between the cells cannot be approximated by the pairwise interaction even in the dilute case in tube flow, and the results of the two studies are quantitatively different.

Last, we discuss effects of the self-diffusion due to the Brownian motion, which is neglected in the present study but self-diffusion due to the Brownian motion may appear in the case of practical fluid. The self-diffusion coefficient due to the Brownian

motion $\mathscr{D}^b$ should be proportional to the thermal energy and reciprocal proportional to the outer fluid viscosity μ and characteristic length ℓ:

$$\mathscr{D}^b \propto \frac{k_b T_k}{\mu \ell},$$

where k_b is the Boltzmann constant and T_k is absolute temperature. When $\mathscr{D}^b$ is much smaller than $\mathscr{D}$ of the present study, the Brownian effect can be negligible. When $\mathscr{D}^b \gg \mathscr{D}$, on the other hand, the self-diffusion is mainly generated by the Brownian motion and the effect of pairwise interaction can be negligible. If we assume room temperature (300 (K)) and $\ell = 2.82 \times 10^{-6}$ (m), we have a following non-dimensional self-diffusion coefficient $\mathscr{D}^b/(\dot{\gamma}\ell^2)$:

$$\frac{\mathscr{D}^b}{\dot{\gamma}\ell^2} = \frac{k_b T_k}{\mu \dot{\gamma} \ell^3} \simeq 1.85 \times 10^{-4}/(\mu\dot{\gamma}).$$

If we approximate the shear-induced self-diffusion is about $\phi \times 10^{-3}$ (cf. figures 6.11 and 6.12), the shear-induced diffusivity becomes significant when $\phi\mu\dot{\gamma} \gg 0.2$.

6.4 Stresslet of two RBCs and its impact on the rheology

Next, we investigate rheological properties of the RBC suspension from the pairwise interactions. In the previous section 5.4.3, we investigated the dilute suspension rheology from a single RBC in shear flow, whose order becomes ϕ. In this section, the leading approximation of the particle stress tensor is expanded to the order of ϕ^2 using the pairwise interaction of the RBCs and discuss the stresslet of two RBCs and its impact on the semi-dilute suspension rheology. We first show the membrane tension during the hydrodynamic interaction between the two RBCs. Next, we discuss the stresslet of the RBCs to investigate the effect of ϕ^2 order term of the particle stress tensor of the semi-dilute suspension.

6.4.1 Membrane tension

We first investigate the membrane tension during the pairwise interaction of the RBCs. Distributions of the principal tension τ_1 and the isotropic tension τ^p during

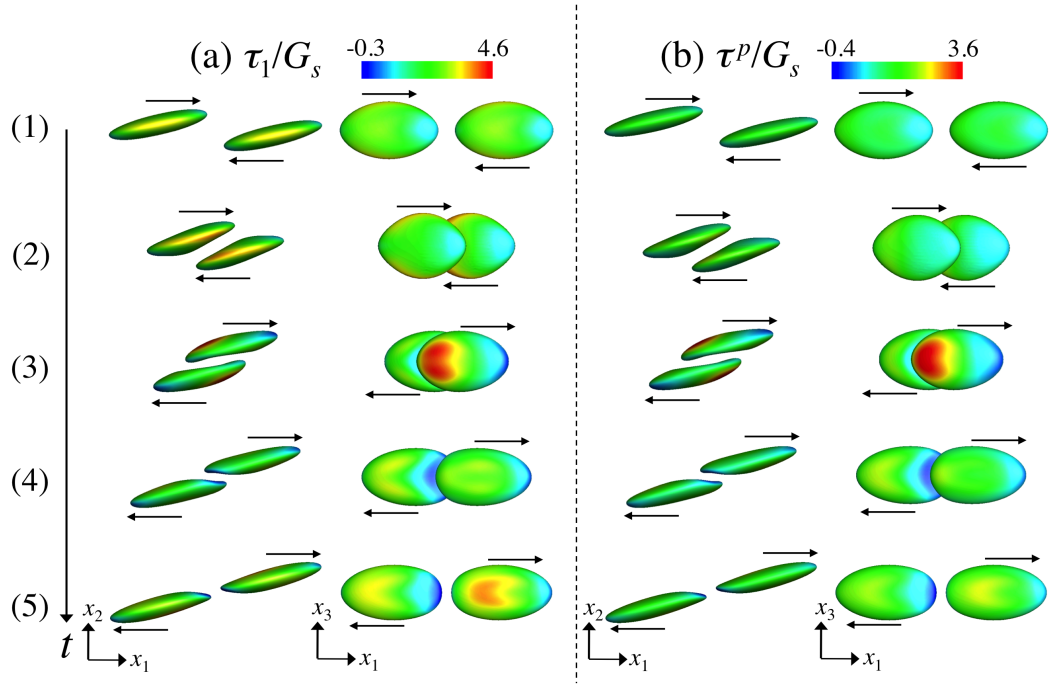

Fig. 6.13 Distributions of (a) the principal tension τ_1 and (b) the isotropic tension τ^p during the interaction. Capillary number is 2.0, the viscosity ratio is 1.0, the angle $\theta_0 = \pi/2$, $\Delta\beta_0 = 0$. The initial positions are set to $\Delta x_1^0 = -10.0$, $\Delta x_2^0 = 0.25$ and $\Delta x_3^0 = 0$, respectively. Numbers in the figure represents the numbering of the time sequence. Arrows represented in each figures indicate the flow direction.

the interaction are shown in figure 6.13(a) and (b), respectively. Capillary number is 2.0, the viscosity ratio is 1.0, and the angle $\theta_0 = \pi/2$, $\Delta\beta_0 = 0$, respectively. The initial positions are the same as figure 6.2. When the interaction start (cf. figure 6.13(2)), the principal tension becomes high where the contact side of the membrane, whereas the isotropic tension does not change significantly. Then, this higher value of τ_1 is mainly caused by the shear deformation effects not the areal deformation effects. In crossing regime (cf. figure 6.13(3)), both the principal tension and the isotropic tension become high at the top side the RBC membrane, which value is the maximum through the interaction period. This result suggest that both the shear deformation effects and areal deformation effects are significantly on the membrane tensions in the crossing regime. When the RBCs are in the separating regime (cf. figure 6.13(4) and (5)), the membrane where surrounded by the two RBCs are compressed and both the

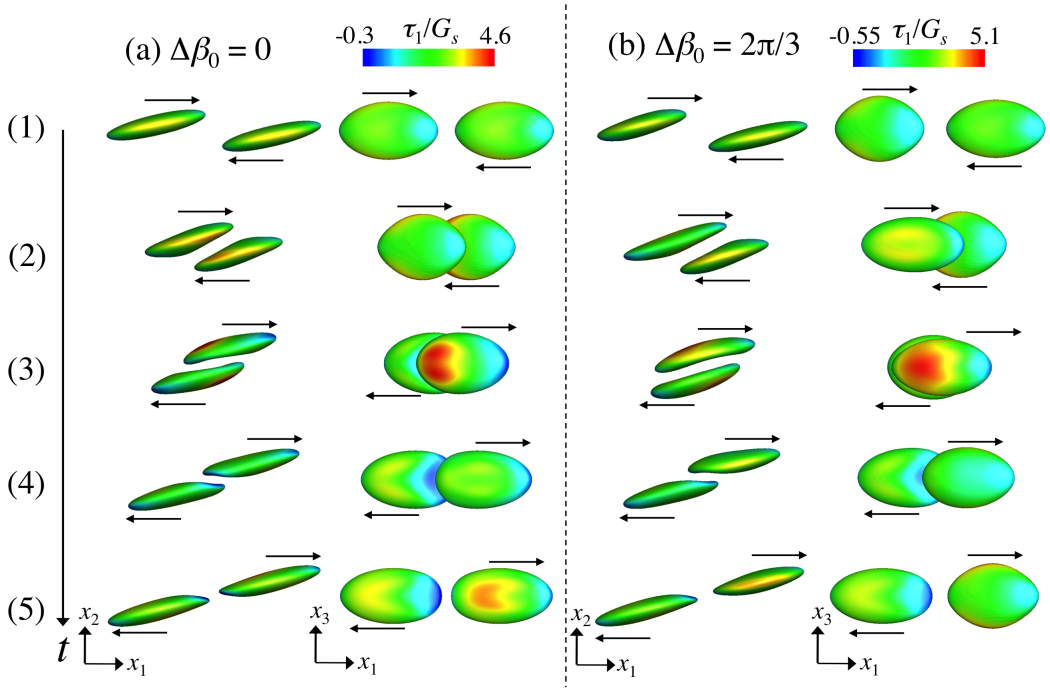

Fig. 6.14 Distributions of the principal tension τ_1 with $\Delta\beta_0 = 0$ and $2\pi/3$ during the interaction. The other numerical conditions are the same as figure 6.13. Numbers in the figure represents the numbering of the time sequence. Arrows represented in each figures indicate the flow direction.

principal tension and the isotropic tension become negative. After the interaction, the membrane tensions become steady periodic, as shown in figure 5.17.

To investigate the membrane tension more in detail, we analyze the effect of angle difference $\Delta\beta_0$ on the membrane tension, i.e. the effect of the shape of the RBCs at the beginning of the interactions. The shape of the RBCs at the beginning of the interaction not only depend on $\Delta\beta_0$ but the initial positions $\underline{\Delta x}^0$. For the simplicity of the discussion, hereafter, $\underline{\Delta x}^0$ is fixed to $\Delta x_1^0 = -10.0$, $\Delta x_2^0 = 0.25$ and $\Delta x_3^0 = 0$, respectively, when we discuss the effect of $\Delta\beta_0$. Distributions of the principal tension τ_1 with $\Delta\beta_0 = 0$ and $2\pi/3$ during the interaction are shown in figure 6.14(a) and (b), respectively. The other numerical conditions are the same as figure 6.13. When $\Delta\beta_0 = 0$, the RBC1 interact to the RBC2 with the most elongation towards the x_3-direction, as shown in figure 6.14(a)(2). Whereas, when $\Delta\beta_0 = 2\pi/3$, the RBC1 interact to the RBC2 with the most elongation towards the x_1-direction, as shown in figure 6.14(b)(2). In the case of $\Delta\beta_0 = 0$, τ_1 becomes high where the contact side of

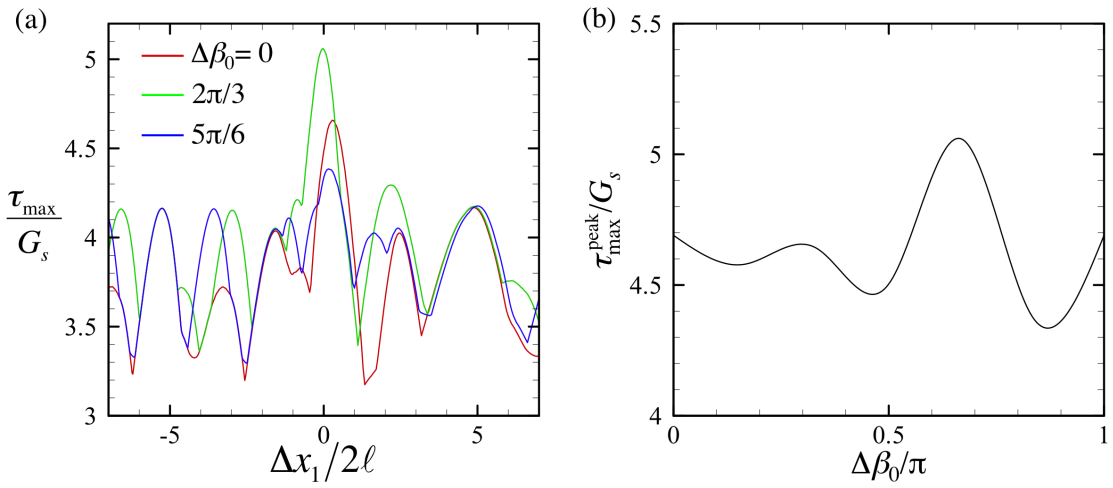

Fig. 6.15 (a)Maximum principal tension of the RBC1 $\tau_{\max}$ as a function of Δx_1. (b)The peak value of $\tau_{\max}$ during the interaction with various $\Delta\beta_0$. In all cases, $Ca = 2.0$ and $\lambda = 1.0$.

the membrane when the RBCs start to interact each other (cf. figure 6.14(a)(2)). In the case of $\Delta\beta_0 = 2\pi/3$, however, τ_1 of the RBC1 becomes high where the top side of the RBC1 (cf. figure 6.14(b)(2)) not where the contact side of the RBC1. Moreover, the maximum values of τ_1 during the interaction (cf. figure 6.14(3)) differ between the two cases, even though the region of the maximum τ_1 are the same. These results suggests that the membrane tension during the pairwise interaction quantitatively and qualitatively depends on the angle difference $\Delta\beta_0$, i.e. the shape of the RBC at the beginning of the interaction.

To investigate the effect of $\Delta\beta_0$ more in detail, the maximum principal tension of the RBC1 as a function of Δx_1 with $\Delta\beta_0 = 0, 2\pi/3$ and $5\pi/6$ are shown in figure 6.15(a). $Ca = 2.0$ and $\lambda = 1.0$ in all cases. We see that the shape of curves, as well as the maximum values, depend on the angle difference $\Delta\beta_0$. In figure 6.15(b), the peak value of τ_1 during the interaction with various $\Delta\beta_0$ are shown. The values become the maximum when $\Delta\beta_0 = 2\pi/3$ and become the minimum $\Delta\beta_0 = 5\pi/6$ and its difference between the maximum and minimum value is about 16%.

We also investigate the membrane tension with $\theta_0 = 0$. Distributions of τ_1 during the interaction are shown in figure 6.16(a). In the case of $\theta_0 = 0$, the RBCs show

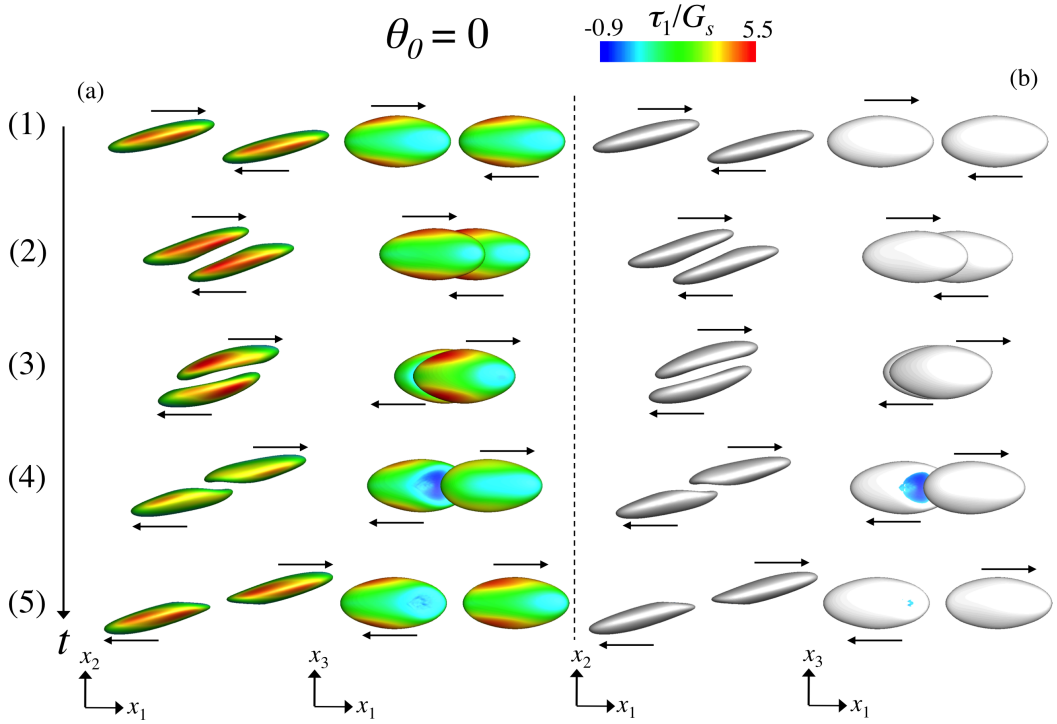

Fig. 6.16 (a)Distributions of τ_1 during the interaction with $\theta_0 = 0$. (b)Distributions of negative τ_1 during the interaction. $Ca = 2.0$, $\lambda = 1.0$ and the initial positions are the same as figure 6.13 for both cases.

the pure tank-treading motion and τ_1 distributions are no longer oscillated. The high values of τ_1 always appear at the side of the RBC when far from the interaction. Besides, we observe that τ_1 becomes always high at the side of the RBC during the interaction as shown in figure 6.16(a). This tendency is qualitatively different from the $\theta_0 = \pi/2$ cases as shown in figure 6.13 and figure 6.14. Moreover, the maximum value of τ_1 become higher than that of $\theta_0 = \pi/2$ cases.

We also observe that the negative principal tension τ_1 during the pairwise interaction, even in the case of only positive values appeared in the solitary case, as shown in figure 6.16(b). The negative tension often cause of the numerical instabilities, then the computations of the pairwise interaction more suffer from the numerical instabilities.

From these results we conclude that the membrane tension during the hydrodynamic interaction between the two RBCs are strongly dependent on the angle and orientation of the RBCs, then we must consider its orientation for the membrane tension within

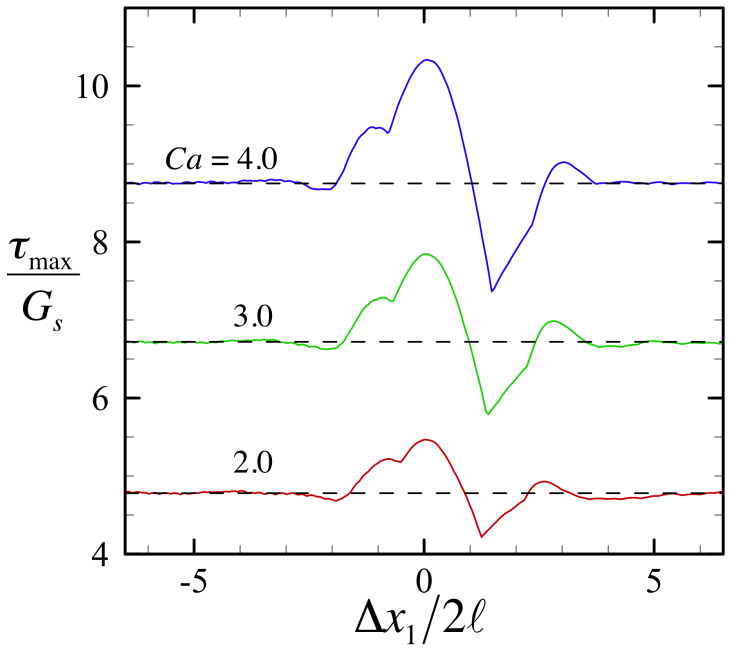

Fig. 6.17 Maximum principal membrane tension of the RBC1 during the interaction $\tau_{\max}$ with $Ca = 2.0, 3.0$ and 4.0 . The viscosity ratio is unity and the initial positions are the same as figure 6.13 in all cases. The broken lines in the figure represent the maximum tension in the solitary cases.

the hydrodynamic interaction. For the simplicity of discussions, we only consider $\theta_0 = 0$ to investigate the membrane tension. In this case, $\Delta\beta_0$ can be omitted because the membrane properties are symmetry towards the flow direction. As shown in the chapter 5, the angle θ is converged to 0 in high Ca regime when the RBC has no interaction with other cells. The membrane tension with $\theta_0 = 0$ may be reliable in high Ca regime. Then we investigate the membrane tension with $\theta_0 = 0$ in high Ca regime, hereafter.

The maximum principal tension of the RBC1 during the interaction $\tau_{\max}$ with $Ca = 2.0, 3.0$ and 4.0 are shown in figure 6.17. The viscosity ratio is unity and the initial positions are the same as figure 6.13 in all cases. The broken lines in the figure represent the maximum tension in the solitary cases. When the RBCs are in crossing regime (e.g. figure 6.16(3)), the curves have a peak value in all Ca cases. In this regime, high pressure of the outer fluid is observed as shown in figure 6.4, which may

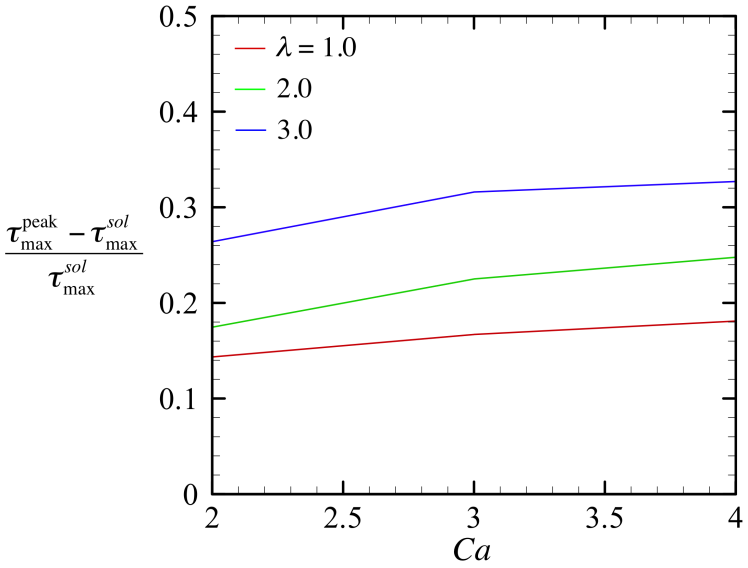

Fig. 6.18 Increment of the maximum tension from the solitary case with various Ca and λ conditions

cause of the high values of the maximum tension. In separating regime (e.g. figure 6.16(4)), the values are smaller than the values of the solitary cases in whole range of Ca. In this regime, the negative tensions appear on the membrane as shown in figure 6.16(b) and the shape is strongly asymmetry. This asymmetric shape likely cause of the smaller tension than that of the symmetric shape of the single RBC in shear flow.

For more detailed analysis of the maximum principal tension during the pairwise interaction, the increment of the maximum tension from the solitary case are shown in figure 6.18. The increment ratio is defined as $\left(\tau_{max}^{\text{peak}} - \tau_{max}^{sol}\right)/\tau_{max}^{sol}$, where τ_{max}^{peak} is the peak value of the maximum principal tension during the interaction and τ_{max}^{sol} is the maximum principal tension in the solitary cases. From figure 6.18, we see that the effect of Ca on the increment of the principal tension is moderate comparing with λ effect. The maximum displacement towards the x_2-direction decreases as λ increases (cf. figure 6.6), yields highly interaction between the two RBCs with higher λ.

The maximum value of the increment ratio is at most about 30% in whole range of λ and Ca. Even in the case of high λ condition (the highest value is $\lambda = 3.0$ in this study), the RBCs do not contact each other during the interaction and they

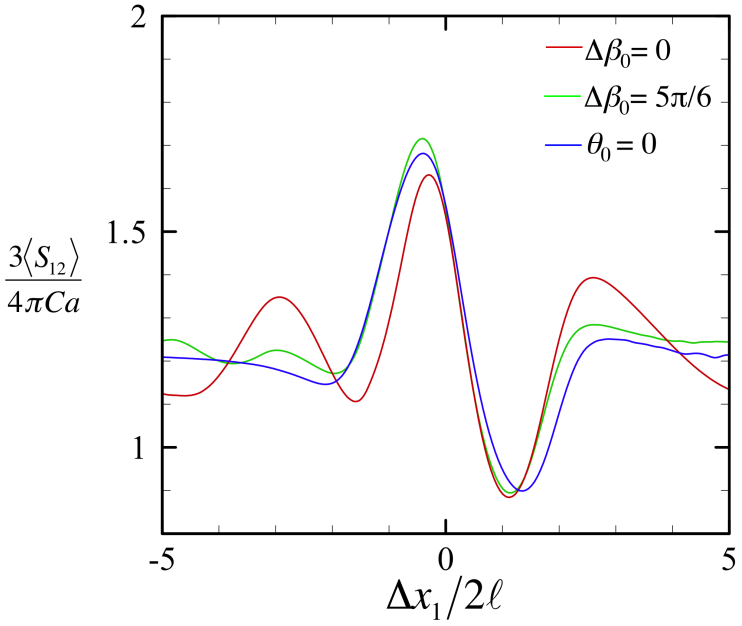

Fig. 6.19 Shear stress component of the stresslet with various orientation. The initial positions are $\Delta x_1 = -10$, $\Delta x_2 = 0.25$ and $\Delta x_3 = 0$, respectively. The capillary number is 2.0 and the viscosity ratio is 1.0 in all cases.

can easily pass each other. Then, the effect of the interaction on the membrane tension becomes moderate. Our numerical results of the membrane tension during the pairwise interaction can be viewed as a first approximation of the cell-cell interaction in a dilute suspension. They can be used for better understanding of the membrane tension in a dilute suspension of the RBCs.

6.4.2 Stresslet

Finally, we discuss the stresslet of the RBCs during the pairwise interaction to investigate the effect of ϕ^2 order term of the particle stress tensor of the semi-dilute suspension. First, we investigate the effects of the orientation on the stresslet. The shear stress component $\langle S_{12}\rangle$ with various orientations are shown in figure 6.19. The bracket representation is the ensemble average of the stresslet. The initial positions are $\Delta x_1 = -10$, $\Delta x_2 = 0.25$ and $\Delta x_3 = 0$, respectively. The capillary number is 2.0 and the viscosity ratio is 1.0 in all cases. As the same for the membrane tension,

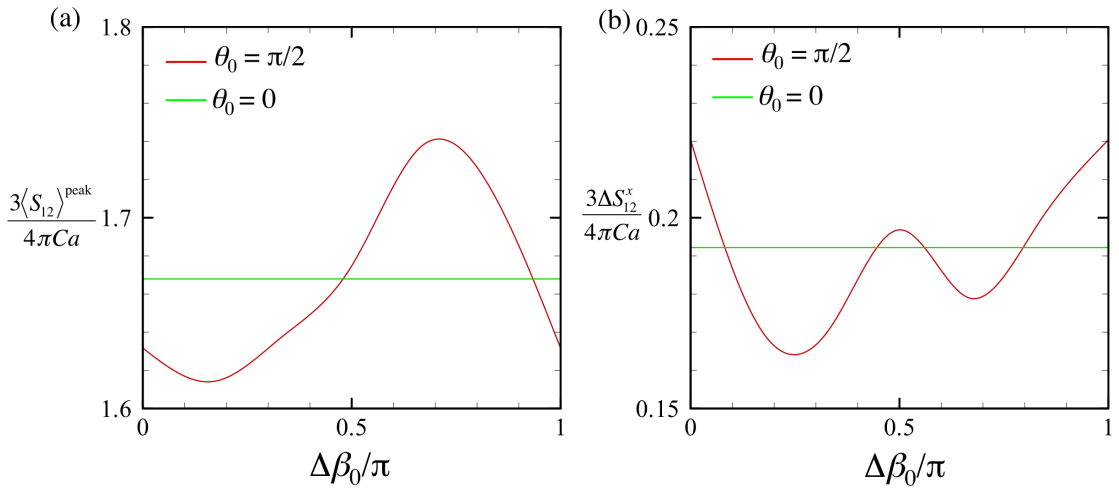

Fig. 6.20 (a) The peak value of S_{12} and (b) integrated ΔS_{12} towards the x_1-direction as a function of $\Delta\beta_0$. The numerical conditions are the same as figure 6.19. Definition of ΔS_{12}^x is described in (6.12).

the curves are dependent on both θ_0 and the angle difference $\Delta\beta_0$. To investigate the effect of θ_0 and $\Delta\beta_0$ in quantitatively, the peak value of the stresslet $\langle S_{12}\rangle$ as a function of $\Delta\beta_0$ are shown in figure 6.20(a). The difference between the maximum value (at $\theta_0 = \pi/2, \Delta\beta_0 = 2\pi/3$ in the figure) and the minimum value (at $\theta_0 = \pi/2, \Delta\beta_0 = \pi/3$ in the figure) reaches about 7% To investigate the effects of the interaction in a given initial position x_2^0 and x_3^0, we define the following integral equation:

$$\Delta\underline{\underline{S}}^x = \int \left(\langle \underline{\underline{S}} \rangle - \underline{\underline{S}}^{sol} \right) dx_1^0. \tag{6.12}$$

The above equation is equivalent to the effect of the one-time hydrodynamic interaction of the RBCs on the stresslet. When the RBCs far from each other, the integrand function can be negligible. In this study, the interval of the integration with respect to x_1 is defined as $[-7, 7]$, which is sufficiently long that results obtained in this chapter are unaffected qualitatively by the selection of integration interval. ΔS_{12}^x with various $\Delta\beta_0$ are shown in figure 6.20(b). The values of ΔS_{12}^x depend on $\Delta\beta_0$ and its variation reaches almost 20% in the parameter range $\Delta\beta_0 \in [0, \pi]$. From these results, we conclude that the stresslet during the interaction depend on the orientation and the phase of the swinging motion of the RBC and we must take into account of them

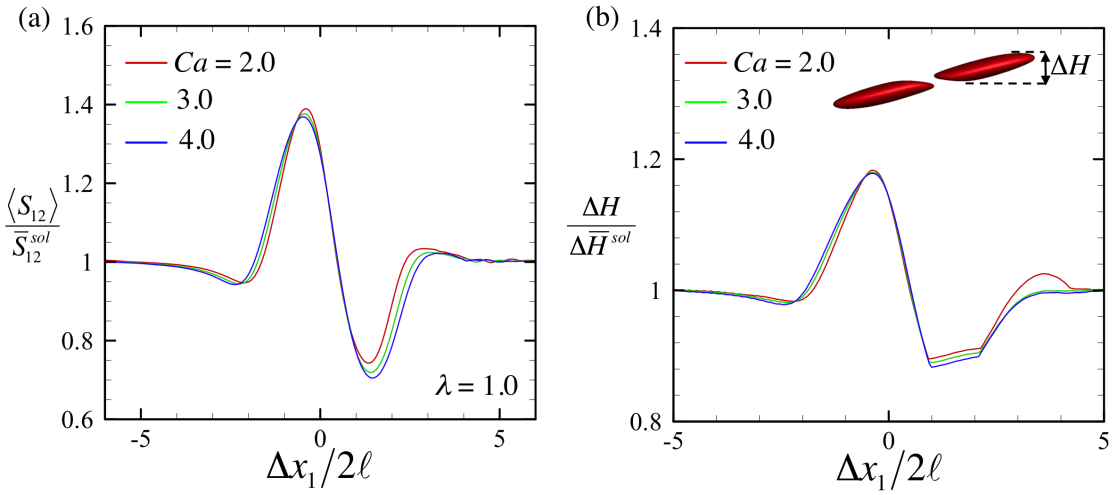

Fig. 6.21 (a) Ensemble average S_{12}, which is normalized by the stresslet of the solitary cases with $Ca = 2.0, 3.0$ and 4.0. (b)Hight of the RBC1 during the interaction. The viscosity ratio is unity in all cases.

to investigate the stresslet in the pairwise interaction. Hereafter, θ_0 is fixed to 0 for the simplicity of the discussions.

Next, we investigate the effect of Ca on the stresslet of the RBCs. The ensemble average S_{12} with $Ca = 2.0, 3.0$ and 4.0 are shown in figure 6.21(a). The values are normalized by the stresslet of the solitary case S_{12}^{sol}. The viscosity ratio is unity in all cases. In crossing regime, $\langle S_{12} \rangle$ become higher than S_{12}^{sol}. In separating regime, on the other hand, $\langle S_{12} \rangle$ become smaller than S_{12}^{sol}, in all cases.

To investigate $\langle S_{12} \rangle$ more in detail, the hight of the RBC1 ΔH during the interaction are shown in figure 6.21(b). In crossing regime, the RBCs shape become concave shape to overcome the other cell, as shown in figure 6.16(3). As a result, ΔH become larger than the solitary cases. In separating regime, on the other hand, the shape of the RBCs are strongly asymmetry with respect to its mass centre and the backward membrane become almost flatten, as shown in figure 6.16(4). Then, the hight becomes smaller than the symmetric shape, i.e. the solitary case. The average values of $\langle S_{12} \rangle / S_{12}^{sol}$ during the interaction are no longer 1.0. This result is important to discuss the stresslet of the ϕ^2-term, because the integrand is not zero and the term does exist.

We next investigate the effect of λ on the stresslet of the RBCs. $\langle S_{12} \rangle$ with $\lambda =$

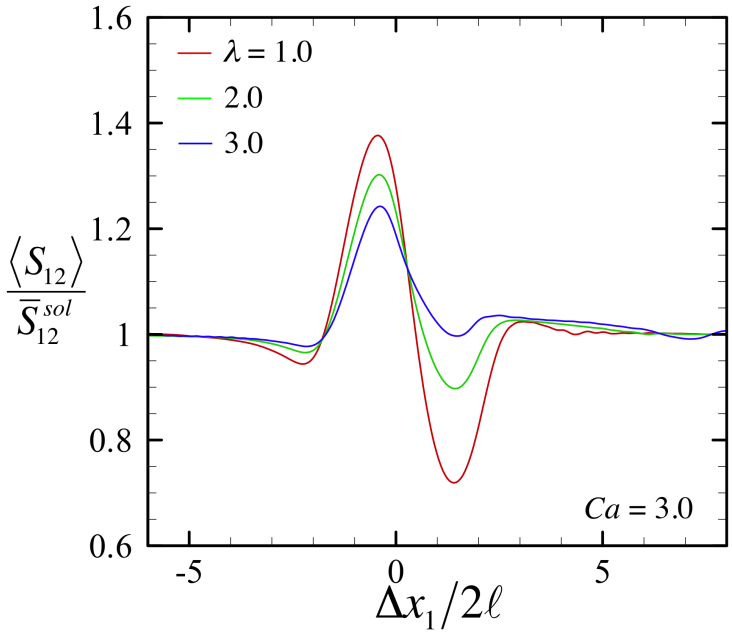

Fig. 6.22 $\langle S_{12} \rangle$ with $\lambda = 1.0, 2.0$ and 3.0. In all cases, $Ca = 3.0$.

1.0, 2.0 and 3.0 are shown in figure 6.22. In all cases, $Ca = 3.0$. The maximum values of $\langle S_{12} \rangle$ become small as λ increases, but the minimum values become larger with higher λ, then the curve is strongly asymmetric with higher λ. In the case of non-identical viscosity ratio, the stresslet is determined by not only the membrane load $\underline{q}$ but also the membrane velocity $\underline{v}$. In high λ case, the inner viscous effect becomes significant and the response to the pairwise interaction becomes slowly. Such a slow response of the membrane deformation with higher λ likely cases the strong asymmetric curve of $\langle S_{12} \rangle$, which produces the large value of the ϕ^2 order term of the particle stress tensor. The effect of λ is then important on the stresslet of the RBCs during the pairwise interaction.

Not only the shear viscosity term but the diagonal components are also important for the suspension rheology. The component of $\langle S_{11} \rangle$ and $\langle S_{33} \rangle$ are shown in figure 6.23(a) and (b), respectively. In the case of $\lambda = 1$, the curve of $\langle S_{11} \rangle$ has a moderate peak in crossing regime but a significant least value in separating regime. Then, the average value of $\langle S_{11} \rangle / S_{11}^{sol}$ with $\lambda = 1$ becomes less than 1.0. This result suggests

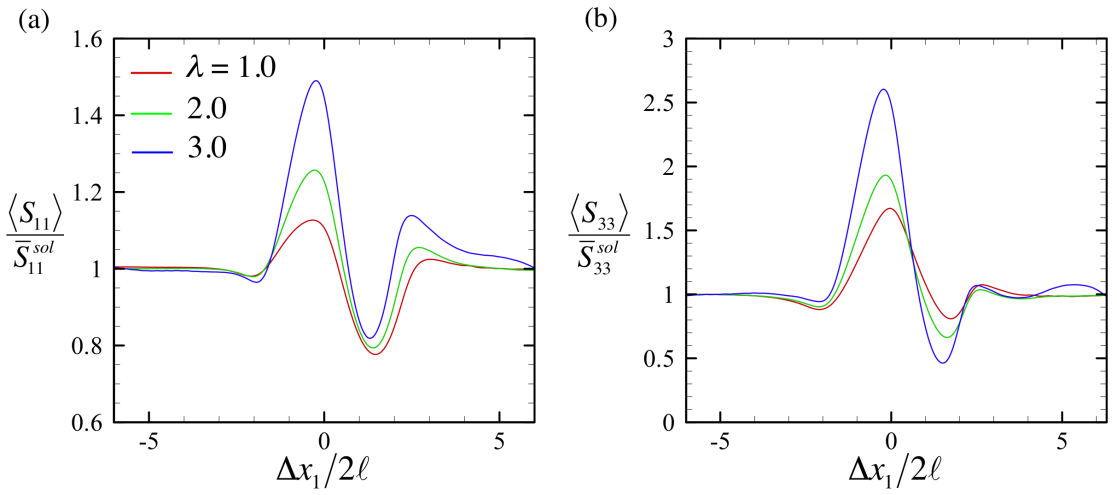

Fig. 6.23 Diagonal component of the stresslet (a) $\langle S_{11} \rangle$ and (b) $\langle S_{33} \rangle$ with $\lambda = 1.0, 2.0$ and 3.0. In all cases, $Ca = 3.0$.

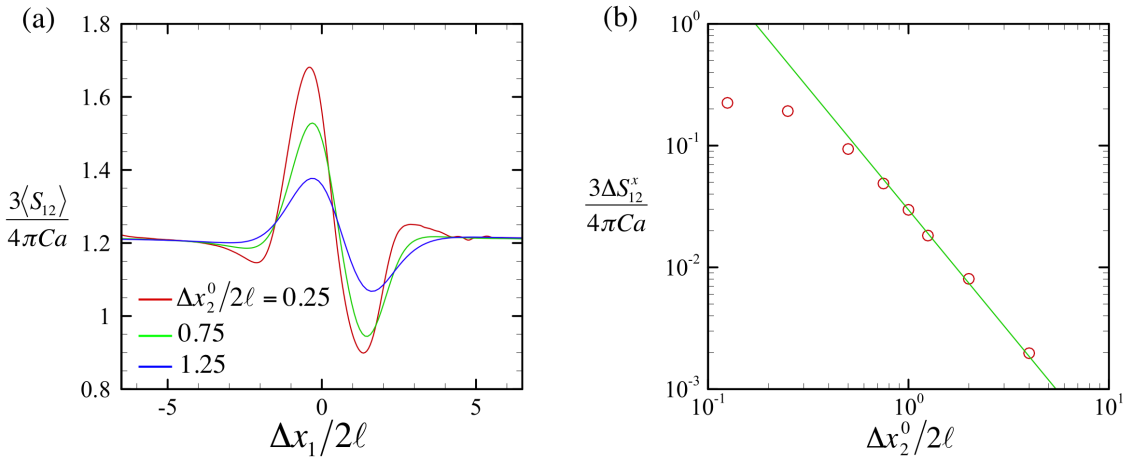

Fig. 6.24 Effects of the initial positions of the RBCs. (a) Shear stress component of the stresslet with $\Delta x_2^0 = 0.25, 0.75$ and 1.25. (b)ΔS_{12}^x as a function of Δx_2^0 in log-log scale.

that the ϕ^2-term becomes small or even becomes negative due to the interaction in small λ cases. In higher λ cases, on the other hand, the average values of $\langle S_{11} \rangle / S_{11}^{sol}$ are higher than 1.0. The increment ratio of $\langle S_{33} \rangle$ is dependent on the λ but the curves do not qualitatively change with λ.

To seek the ϕ^2 order term of the particle stress tensor, we investigate effects of

the initial position on the stresslet and the results are shown in figure 6.24(a). The viscosity ratio is unity and capillary number is 2.0. In all cases, $\Delta x_3^0 = 0$. As we expected, the distance between the two RBCs becomes more large and the interaction becomes more weak. To investigate the effect of Δx_2^0 in more quantitatively, ΔS_{12}^x as a function of Δx_2^0 in log-log scale are plotted in figure 6.24(b). The numerical results are represented by red circles. In far-field interaction ($\Delta x_2^0/2\ell \geq 1$), the results linearly decrease with respect to Δx_2^0. The green line in the figure indicates the linear fitting of the results and its slope is -2, which is relevant to that ΔS_{12}^x has the order r^{-2} in $\Delta x_2^0/2\ell \geq 1$ regime. This result suggests that $\langle S_{12} \rangle - S_{12}^{sol}$ decreases as r^{-3} and the infinite integral of the ϕ^2 order term diverges as fast as $\ln r$. To perform the integral of the ϕ^2-term, Batchelor et al. (1972) recalculated the ensemble average before reducing it to an average over the separation of spheres as:

$$\int_0^\infty \left(\langle \underline{\underline{S}}(\underline{r}) \rangle - \underline{\underline{S}}^{sol} - \frac{20\pi\mu\ell^3}{3} (\underline{\underline{e}}(\underline{r}) - \underline{\underline{E}}) \right) dV, \tag{6.13}$$

where $\underline{\underline{e}}$ is the rate of strain at position $\underline{r}$ and $\underline{\underline{E}}$ is the bulk average rate of strain. However, this method cannot be applied, because equation (6.7) is not satisfied in the case of the RBCs. In this thesis, we only consider in near field interaction for the ϕ^2-term.

To investigate the effect of ϕ^2-term, we use cross-flow trajectories as shown in figure 6.10. Then, the domain truncation r_c is defined as 2.0 and we define a quasi-ϕ^2-term of the particle stress tensor $\underline{\underline{f}}$ as follow:

$$\underline{\underline{f}} = \frac{9}{8\pi^2 Ca} \int_0^{r_c} \int_0^{\frac{\pi}{2}} \Delta \underline{\underline{S}}^x r dr d\psi. \tag{6.14}$$

The above integral is calculated by Gaussian numerical integration with bi-linear element. The number of Gauss integral point in each element is 25. In the case of $x_2^0 = 0$, we assume no interaction and the integrand becomes 0. The results of f_{12} and first and second normal stress difference $N_1' = f_{11} - f_{22}$ and $N_2' = f_{22} - f_{33}$ are shown in figures 6.25(a) and (b), respectively. f_{12} becomes positive in all cases, which is equivalent to that the effective shear viscosity increases due to the hydrodynamic interaction of the RBCs. The typical values of f_{12} are about 10 times smaller than the typical values of ϕ-term, which is shown in figure 5.24. In the case of a rigid

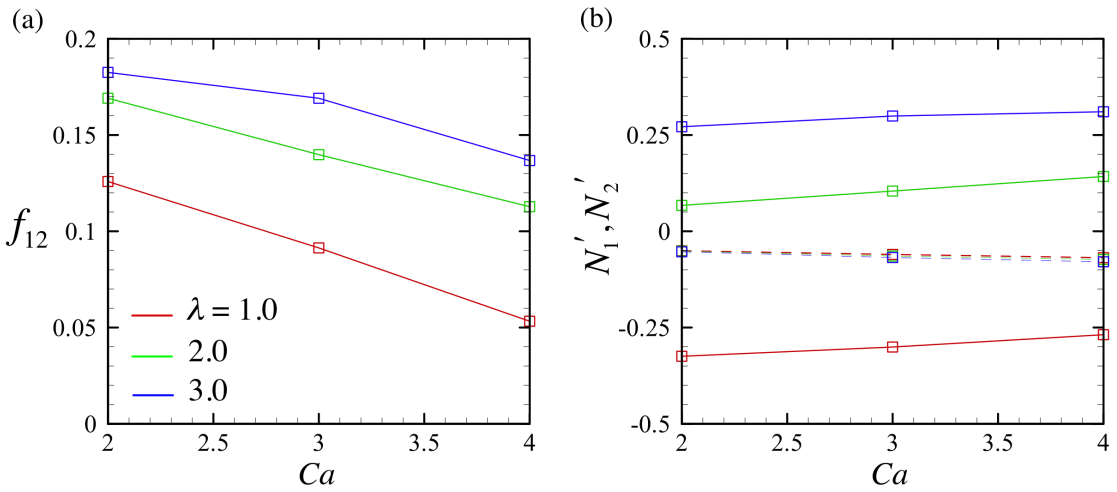

Fig. 6.25 Quasi-ϕ^2-term of the particle stress tensor. (a) Shear viscosity f_{12} and (b) normal stress difference N_1' (solid line) and N_2' (broken line).

spherical particle, the ϕ-term and ϕ^2-term of effective viscosity have the same order; $\mu* = \mu(1+2.5\phi+7.6\phi^2)$ [12]. In the case of deformable RBCs, the cells can easily pass away each other and the effects of the interaction on the shear viscosity do not become significant comparing with the rigid body cases. The second normal stress difference N_2' are always negative but its values are also about 10 times smaller than the ϕ order term. The first normal stress difference N_1' are, on the other hand, qualitatively dependent on λ and the value becomes negative in the case of $\lambda = 1$. This is because the average $\langle S_{11}\rangle/S_{11}$ is smaller than 1.0 with identical viscosity, as shown in figure 6.23(a).

We finally discuss the truncation error of the ϕ^2-term. In the case of deformable capsule, it is impossible to look for the exact ϕ^2-term, however, that of rigid spherical particle is now available. The scaling of ϕ^2-term is the same among rigid particles, drops and capsules, thus the scaling estimation of rigid particle will give us a useful information. To calculate equation (6.13) of rigid spherical particles, Batchelor et al. [12] divided the integration range into 3 regime:

$$2 \leq \xi \leq 2.0025, \quad 2.005 \leq \xi \leq 3.0, \quad 3.0 \leq \xi \leq \infty,$$

where $\xi = r/\ell$ is the normalized distance of the mass centre of two identical particles.

In the first and third regime, the integration can be calculated analytically but in the second regime it was calculated numerically in the paper. In our numerical simulation, the domain truncation r_c is 2.0, which is equivalent to $\xi = 4.0$ in the system. In the third regime, the integration can be written as $\frac{15}{2}\int_3^\infty \xi^{-4} d\xi$ [12]. The value of full integration is equivalent to 0.0926 and the value with the truncation ($\xi = 4.0$) is equal to 0.0536. The difference between the two cases becomes 42% but the total value of the ϕ^2-term becomes 7.6 (full integration) and 7.3 (with truncation), respectively, and the difference between the two is less than 4%. From this result the integral range used in our numerical simulation may be large enough to calculate the ϕ^2-term. However, the above estimation is conducted with the convergent form of the integrand and more precise discussions may be needed.

6.5 Conclusions

In this chapter, we investigate the hydrodynamic interaction between the two RBCs in shear flow and discuss the shear-induced self-diffusion coefficient and the stresslet of the RBCs. An RBC is modeled as a capsule with a hyper-elastic membrane and the SK law with $C = 10$ is employed for the membrane to express the aarea incompressibility of the RBC membrane. The finite element method is used to solve the membrane mechanics. Due to the small scale of the RBC, we also assume that flow is a Stokesian, i.e. inertia free, and the flow is solved by the boundary element method.

Because of the deformability of the RBCs, the trajectories were no longer symmetric and displacement $\underline{\delta x}$ was produced in the (x_2, x_3)-plane. The trajectories changed significantly with λ but changed moderately with Ca. This result suggests that the trajectories during the hydrodynamic interaction between the two RBCs are dominant to λ but moderate to Ca. It is also found that the angle difference $\Delta\beta_0$ and the orientation θ_0 do not significantly affect on the displacement $\underline{\delta x}$. Then, the trajectories of the RBC during the hydrodynamic interaction are independent of the angle and orientation of the RBCs.

To calculate the self-diffusion coefficient of the RBCs, we used the G_1 trajectories and displacement $\underline{\delta x}$ with various initial potions in the (x_2, x_3)-plane. In far-field interaction, we used a asymptotic form of the integrand and analytically calculated. In

near-field interaction, we used a Gaussian numerical integration scheme with bi-linear element and computed it numerically. $\mathscr{D}_{22}$ was always larger than $\mathscr{D}_{33}$, because the displacement δx_2 was always larger than the displacement δx_3. These results suggest that diffusivity of the RBCs in a smi-dilute suspension under shear flow is no longer isotropic and we must consider the behaviour of RBCs in fluid flow individually to determine the self-diffusivities of RBCs. The self-diffusion of the RBCs were similar with that of the drops but the values were quantitatively different. The RBC membrane has elastic resistance but the drops has only surface tension. This qualitative difference of the interface likely cases the quantitative difference of diffusivity. We also observed that the self-diffusivities of the RBCs are a strong function of the viscosity ratio, whereas it is moderate with Ca. Then, we conclude that the self-diffusion of the RBCs during the pairwise interaction is dominant significantly to λ and moderate to Ca.

The membrane tension during the pairwise interaction quantitatively and qualitatively depended on the angle difference $\Delta\beta_0$ and the orientation θ_0. From this result, we conclude that the orientation of RBC during the interaction must be concerned for the membrane tension. The increment of the principal tension from the solitary case strongly depended on λ but moderately on Ca. This is because the trajectories strongly depend on λ but moderately on Ca. The maximum value of the increment ratio was at most about 30% in whole range of λ and Ca. Even in the case of high λ condition (the highest value is $\lambda = 3.0$ in this study), the RBCs did not contact each other during the interaction and they could easily pass each other. Then, the effect of the pairwise interaction on the membrane tension became moderate.

Finally, we discussed the stresslet of the RBCs during the pairwise interaction and its impact on the ϕ^2 order term of the particle stress tensor. As the same for the membrane tension, the stresslet were also dependent on both the orientation and angle difference of the RBC. We again conclude that the orientation of RBCs must be taken into account to investigate the rheology of the pairwise interaction. To investigate the effect of the pairwise interaction on the particle stress tensor, we define the quasi-ϕ^2-term $\underline{\underline{f}}$. f_{12} were always positive with various λ and Ca, which is relevant to the effective shear viscosity increase quadratically. The typical values

of f_{12} were about 10 times smaller than the typical values of ϕ-term. In the case of deformable RBCs, the cells can easily pass away each other and the effects of the interaction on the shear viscosity do not become significant. The first normal stress difference N_1' became negative in the case of $\lambda = 1$. This is because the average $\langle S_{11} \rangle / S_{11}$ is smaller than 1.0 in the identical viscosity case. This result suggests that the elasticity of the suspension is reduced by the hydrodynamic interaction of RBCs in the case of $\lambda = 1$.

From these results we conclude that the stresslet and the self-diffusivities during the pairwise interaction is affected significantly by λ but moderately by Ca and the RBC can escape the strong interaction thanks to the elasticity of the membrane. Our numerical results of the pairwise interaction can be viewed as a first approximation of the cell-cell interaction in a dilute suspension. They can be used for better understanding of the complicated mechanics of a suspension of the RBCs.

Chapter 7

Conclusions

The aim of this study is development of macroscopic or continuum models of populations of multiple RBCs in fluid flow. In this thesis, we discussed the mechanical modeling of the RBC membrane by comparing discrete spring network models and continuum based constitutive laws and investigated the kinematics and the rheology of an RBC in shear flow. Finally, we investigated the pairwise interaction of RBCs and discussed the self-diffusion and rheological properties of a suspension of RBCs in semi-dilute regime. Summaries and conclusions conducted in this thesis can be written as follows:

In chapter 2, the governing equations of RBCs deforming under viscous flow were presented. An RBC was modeled as a capsule with a hyper-elastic membrane. Due to the small size of the RBCs, flow of the internal and external liquids were described by a boundary integral equation of the Stokes flow. For mathematical descriptions of the membrane mechanics, we used the shell theory of the large elastic deformation.

In chapter 3, we described the numerical methods for the capsule dynamics in viscous flow. For the membrane mechanics of a capsule, a finite element method was used. To solve the boundary integral equation of the flow field, a boundary element method was employed. For validations of the numerical scheme of the finite element-boundary element (FE-BE) coupling method, we investigated the membrane load and capsule deformation under inflation and shear flow condition. The results were

compared with former analytical and numerical studies and we confirmed that good agreement with our numerical results and the former analytical and numerical studies. To accelerate computation speed, GPGPU was applied to the FE-BE coupling method using CUDA. We succeeded about 230 times acceleration of the computation speed comparing with CPU computation.

In chapter 4, we compared the mechanical properties of a membrane modeled with continuum constitutive laws and a discrete spring network under various conditions: uniaxial and isotropic deformations of a 2D membrane, inflation of a capsule and deformation of an initially spherical capsule in a simple shear flow. The results have shown that the mechanical properties of spring networks are strongly dependent on the mesh configuration.

In the small deformation limit, the mechanical properties of the spring network model may be predicted analytically. It is found that, the spring network model has anisotropic mechanical properties in general. However isotropic meshes have mechanical properties that converge towards those of an isotropic material. To express isotropic elasticity using a spring network model, the mesh must therefore be isotropic and sufficiently fine, relative to the variation of the stress field. Moreover, in the small deformation limit, we observe that the behaviour of the spring network with a fine square cross mesh is similar to NH and SK $C = 1$, ($E_s = 3.0G_s$, $\nu_s = 1/2$), by adjusting $k/G_s = 2.0$. Square cross-centre and regular-triangle meshes are similar to SK $C = 1/2$ ($E_s = 8/3G_s$, $\nu_s = 1/3$), by adjusting $k/G_s = 2.0$ and $k/G_s = 4/\sqrt{3}$, respectively. These correlations are important, because one can determine the spring constant by performing conventional mechanical experiments.

In large deformation, the stress-strain relationship under isotropic elongation shows a strain-softening behaviour for all mesh types, and it is difficult to express the area-incompressible property. For a capsule in a simple shear flow, we also confirm that a spring network cannot express the $D_{12}^{\infty} - Ca$ correlation of a capsule with an area-incompressible membrane. Thus, to express a biological cell membrane, we need to choose a membrane model that can express the local area incompressibility, such as the SK law, instead of a spring network model.

In chapter 5, we investigated the kinematics and rheology of a single RBC in creeping shear flow and the results were applied to rheological properties of a dilute suspension of RBCs in shear flow.

In very low Ca regime, the RBC showed quasi-rigid like tumbling motion. In high Ca regime, the RBC showed swinging motion. These results were consistent with former experimental observations and numerical computations of an RBC in shear flow. We also observed quasi-circular profiles of the RBC in the shear plane, and we defined such a motion as tumbling-swinging transition.

When the revolution axis of a spheroidal capsule was not initially located in the shear plane, the capsule showed reorientation phenomena. Steady orientation of the capsule depended on the strength and unsteadiness in the background flow. Given that the transition can be controlled by adjusting the background flow strength as well as the unsteadiness in the background flow direction, the results obtained here can be utilized for particle-alignment techniques in engineering applications, such as counting non-spherical particles by light scattering, making anisotropic materials, etc.

The large deformation of the RBC was suppressed by a strain-hardening property of the SK law. We also observed that the length in the x_3-axis L_3 decrease as L_1 increase to preserve the surface area of the membrane. Deformation of the RBC is strongly depend on the membrane model, thus we again conclude that we need to choose a suitable membrane model to express the mechanical properties of biological membrane. The deformation also tended to be suppressed when the viscous effect inside the capsule becomes large, i.e. high λ condition. These results suggest that not only the shear rate but the viscosity ratio of the internal and external liquids dominate the deformation of the RBC in shear flow.

Distributions of the principal tensions change periodically together with the shape oscillation and the maximum tensions appeared on the side of the deformed RBC when $\theta_0 = \pi/2$, whereas the high isotropic tension only appeared at the top/bottom of the deformed RBC. The maximum principal tension should be correlated to the membrane rupture, and the isotropic tension should be correlated to the regulation of the mechano-transduction of the RBC, these regions are then important to understand

the mechanisms of the hemolysis and the mechano-transduction of the RBCs. We also investigated the maximum and average tensions, $\max(\tau_{\max})$, $\max(\tau^p_{\max})$ and τ^p and $\bar{\tau}^p$, and these tensions increase monotonically with Ca even though the deformation is suppressed in high Ca regime. These findings on the membrane tension would be useful for better understanding of the mechanisms of the hemolysis and the mechano-transduction of RBCs.

In dilute regime, the effective shear viscosity converged to 2.5 in the case of $\theta_0 = \pi/2$ and 4.3 in the case of $\theta_0 = 0$, respectively with very low Ca number. We saw that the shear-thinning behaviour of the effective shear viscosity, which is consistent with former experimental observations of the RBC suspension. Surprisingly, the effective shear viscosity of the suspension became small with higher λ, because the hight of the deformed RBC became small with higher λ. Which is relevant to that a suspension with inner-viscous capsules has efficient fluidity in dilute regime. The diagonal components of the stresslet were no longer isotropic, then the first normal stress different N_1 became positive, whereas the second normal stress difference N_2 became negative, respectively. These results indicate that the visco-elastic properties of the RBC suspension does exist and the elasticity effects of the suspension become large with smaller λ and larger Ca due to the shear-thinning behaviour. These findings presented here form a fundamental basis for the knowledge of complicated suspension mechanics of capsules and biological cells.

In chapter 6, we investigated the hydrodynamic interaction between the two RBCs in shear flow and discussed the shear-induced self-diffusion coefficient and the stresslet of the RBCs for the ϕ^2 order term.

Due to the deformability of the RBCs, the trajectories were no longer symmetric and displacement $\underline{\delta x}$ was produced in the (x_2, x_3)-plane. The trajectories changed significantly with λ but changed moderately with Ca. This result suggests that the trajectories during the hydrodynamic interaction between the two RBCs are dominant to λ but moderate to Ca. It is also found that the angle difference $\Delta\beta_0$ and the orientation θ_0 do not significantly affect on the displacement $\underline{\delta x}$. Then, the trajectories of the RBC during the hydrodynamic interaction are independent of the angle and

orientation of the RBCs.

To calculate the self-diffusion coefficient of the RBCs, we used the G_1 trajectories and displacement $\underline{\delta x}$ with various initial potions in the (x_2, x_3)-plane. In far-field interaction, we used a asymptotic form of the integrand and analytically calculated. In near-field interaction, we used a Gaussian numerical integration scheme with bi-linear element and computed it numerically. We saw that $\mathscr{D}_{22}$ was always larger than $\mathscr{D}_{33}$. This is because the displacement δx_2 was always larger than the displacement δx_3. These results suggest that diffusivity of the RBCs in a smi-dilute suspension under shear flow is no longer isotropic and we must consider the behaviour of RBCs in fluid flow individually to determine the self-diffusivities of RBCs. The tendencies of self-diffusion between the RBC and drops were similar but quantitatively different. The typical inter-space between the drops in crossing regime were much smaller than the RBC cases, yields strong interaction of two drops This result suggests that the RBCs can escape the strong interaction due to the elasticity of the membrane. We also observed that the self-diffusivities of the RBCs were a strong function of the viscosity ratio, whereas it was moderate on Ca. Then, we conclude that the self-diffusion of the RBCs during the pairwise interaction is dominant significantly to λ and moderate to Ca.

The membrane tension during the pairwise interaction quantitatively and qualitatively depended on the angle difference $\Delta\beta_0$ and the orientation θ_0. From this result, we conclude that the orientation of RBC during the interaction must be concerned for the membrane tension. The increment of the principal tension from the solitary case strongly depended on λ but moderately on Ca. This is because the trajectories strongly depend on λ but moderately on Ca. The maximum value of the increment ratio was at most about 30% in whole range of λ and Ca, because RBCs can easily pass away each other.

Finally, we discussed the stresslet of the RBCs during the pairwise interaction and its impact on the ϕ^2 order term of the particle stress tensor. As the same for the membrane tension, the stresslet were also dependent on both the orientation and angle difference of the RBC. We again conclude that the orientation of RBCs must be taken into account to investigate the rheology of the pairwise interaction. To

investigate the effect of the pairwise interaction on the particle stress tensor, we define the quasi-ϕ^2-term $\underline{\underline{f}}$. f_{12} were always positive with various λ and Ca, which suggests that the effective shear viscosity increase quadratically. The typical values of f_{12} were about 10 times smaller than the typical values of ϕ-term. In the case of deformable RBCs, the cells can easily pass away each other and the effects of the interaction on the shear viscosity do not become significant. The first normal stress difference N_1' became negative in the case of $\lambda = 1$. This is because the average $\langle S_{11} \rangle / S_{11}$ is smaller than 1.0 in the identical viscosity case.

From these results we conclude that the stresslet and the self-diffusivities during the pairwise interaction is affected significantly by λ but moderately by Ca and the RBC can escape the strong interaction thanks to the elasticity of the membrane. Our numerical results of the pairwise interaction can be viewed as a first approximation of the cell-cell interaction in a dilute suspension. They can be used for better understanding of the complicated mechanics of a suspension of the RBCs.

In this thesis, we discussed the rheological properties of dilute suspension of RBCs and self-diffusion and rheology of a suspension of RBCs in semi-dilute regime. Suspensions of small capsules in fluid are common in nature and results obtained from in this thesis will form a fundamental basis for the knowledge of complicated suspension mechanics of capsules and biological cells. Blood is flowing through 10^{-6} to 10^{-2} meter order in blood vessels and multi-scale physics are in there. For consecutive understanding of physiology and several pathology of blood flow, it is now desirable for a mechanical model which can be applied to arbitrary scale physics. Development of the macroscopic continuum model of RBC suspension from the microscopic cellular behaviour of RBCs is one of the biggest scientific challenge in bioengineering field. Author believes that our numerical study can provide the fundamentals for the breakthrough to the multi-scale physics problems of blood flow by constructing more dense suspension continuum model in near future.

Bibliography

[1] Abkarian M., Faivre M. and Viallat A., Swinging of red blood cells under shear flow, Phys. Rev. Lett. 98 (2007) 188302.

[2] Acrivos A., Batchelor G. K., Hinch E. J., Koch D. L. and Murai R., Longitudinal shear-induced diffusion of spheres in a dilute suspension, J. Fluid Mech. 240 (1992) 651–657.

[3] Alkhamis T. M., Beissinger R. L. and Chediak J. R., Artificial surface effect on red blood cells and platelets in laminar shear flow, Blood 75 (1990) 1568–1575.

[4] Bagchi P., Mesoscale Simulation of Blood Flow in Small Vessels, Biophys. J. 92 (2007) 1857–1877.

[5] Bagchi P. and Kalluri P. M., Dynamics of nonspherical capsules in shear flow, Phys. Rev. E 80 (2009) 016307.

[6] Barthès-Biesel D., Motion of a spherical microcapsule freely suspended in a linear shear flow, J. Fluid Mech. 100 (1980) 831–853.

[7] Barthès-Biesel D. and Rallison J. M., The time-dependent deformation of a capsule freely suspended in a linear shear flow, J. Fluid Mech. 113 (1981) 251–267.

[8] Barthès-Biesel D., Diaz A. and Dhenin E., Effect of constitutive laws for two-dimensional membranes on flow induced capsule deformation, J. Fluid Mech. 460 (2002) 211–222.

[9] Barthès-Biesel D., Walter J. and Salsac A.-V., Computational hydrodynamics of capsules and biological cells, chap. in Flow-induced deformation of artificial capsules, Taylor & Francis (2010) 35–70.

[10] Batchelor G. K., The stress system in a suspension of force-free particles, J. Fluid Mech. 41 (1970) 545–570.

[11] Batchelor G. K. and Green J. T., The hydrodynamic interaction of two small freely-moving spheres in a linear flow filed, J. Fluid Mech. 56 (1972) 375–400.

[12] Batchelor G. K. and Green J. T., The determination of the bulk stress in a suspension of spherical particles to order c^2, J. Fluid Mech. 56 (1972) 401–427.

[13] Batchelor G. K., The effect of Brownian motion on the bulk stress in a suspension of spherical particles, J. Fluid Mech. 83 (1977) 97–117.

[14] Carin M., Barthès-Biesel D., Edwards-Lévy F., Postel C. and Andrei D., Compression of biocompatible liquid-filled HSA-alginate capsules: determination of the membrane mechanical properties, Biotechnol. Bioeng. 82 (2003) 207–212.

[15] Chang K. S. and Olbricht W. L., Experimental studies of the deformation and breakup of a synthetic capsule in steady and unsteady simple shear flow, J. Fluid Mech. 250 (1993) 609–633.

[16] Chien S., Sung L. A., Lee M. M.L. and Skalak R., Red cell elasticity as determined by flow channel technique, Biorheology 29 (1992) 467–478.

[17] Cokelet G. R. and Meiselman H. J., Rheological Compaison of Hemoglobin Solutions and Erythrocyte Suspensions, Science 11 (1968) 275–277.

[18] Dao, M., Lim C. T., and Suresh S. Mechanics of the human red blood cell deformed by optical tweezers. J. Mech. Phys. Solids. (2003) 51 2259–2280.

[19] Deschamps J., Kantsler V., and Steinberg V. Phase diagram of single vesicle dynamical states in shear flow, Phys. Rev. Lett. 102 (2009) 118105

[20] Diaz A., Pelekasis N. and Batrhès-Biesel D., Transient response of a capsule subjected to varying flow conditions: effect of internal fluid viscosity and membrane elasticity, Phys. Fluids 12 (2000) 948–957.

[21] Diaz A., and Batrhès-Biesel D., Entrance of a bioartificial capsule in a pore, CMES 3:3 (2002) 321–338.

[22] Doddi S. K., and Bagchi P., Lateral migration of a capsule in a plane Poiseuille flow in a channel, Int. J. Multiphase Flow, 34 (2008) 966–986.

[23] Doddi S. K., and Bagchi P., Three-dimensional computational modeling of multiple deformable cells flowing in microvessels, Phys. Rev. E, 79 (2009) 046318.

[24] Dodson III W. R., and Dimitrakopoulos P., Dynamics of strain-hardening and strain-softening capsules in strong planar extensional flows via an interfacial spectral boundary element algorithm for elastic membranes, J. Fluid Mech., 641 (2009) 263–296.

[25] Eggleton C. D. and Popel A. S., Large deformation of red blood cell ghosts in a simple shear flow, Phys. Fluids 10 (1998) 1834–1845.

[26] Einstein A., A new determination of molecular dimensions, Annln. Phys. 19 (1906) 289.

[27] Evans E. A. and Fung Y. C., Improved measurements of the erythrocyte geometry, Microvasc. Res. 4 (1972) 335–347.

[28] Evans E. A., A new material concept for the red cell membrane, Biophys. J. 13 (1973) 926–940.

[29] Fischer T. M., Stohr-Liesen M. and Schmid-Schonbein H., The red cell as a fluid droplet: tank tread-like motion of the human erythrocyte membrane in shear flow, Science 202 (1978) 894-896.

[30] Freund J. B. and Orescanin M. M., Cellular flow in a small blood vessel, J. Fluid Mech. 671 (2011) 466-490.

[31] Foessel E., Walter J., Salsac A.-V. and Barthès-Biesel D., Influence of internal viscosity on the deformation of a spherical capsule in a simple shear flow, J. Fluid Mech. 672 (2011) 472-486.

[32] Fung Y. C., and Tong P., Theory of the sphering of red blood cells, Biophys. J. 8 (1968) 175–198.

[33] Goldsmith H. L. and Marlow J., Flow behaviour of erythrocytes :1. rotation and deformation in dilute suspensions, Proc. R. Soc. Lod. B. 182 (1972) 351–384.

[34] Goldsmith H. L., Bell D. N., Braovac S., Steinberg A. and Mclntosh F., Physical and chemical effects of red cells in the shear-induced aggregation of human platelets, Biophys. J. 69 (1995) 1584–1595.

[35] Green A. E. and Adkins J. E., Large elastic deformations, Second edition, Clarendon Press, Oxford, 1970.

[36] Hansen J. C., Skalak R., Chien S. and Hoger A., An elastic network model based on the structure of the red blood cell membrane skeleton, Biophys. J. 70 (1996) 146–166.

[37] Hobbie E. K. and Fry D. J., Nonequilibrium Phase Diagram of Sticky Nanotube Suspensions, Phys. Rev. Lett. 97 (2006) 036101.

[38] Ishikawa T., Simmonds M. P. and Pedley T. J., Hydrodynamic interaction of two

swimming model micro-organisms, J. Fluid Mech. 568 (2006) 119–160.

[39] Ishikawa T., and Yamaguchi T., Shear-induced fluid-tracer diffusion in a semidilute suspension of spheres, Phys. Rev. E 77 (2008) 041402.

[40] Iso Y., Cohen C., Koch D. L., Orientation in simple shear flow of semi-dilute fiber suspensions 2. Highly elastic fluids, J. Non-Newtonian Fluid Mech. 62 (1996) 135–153.

[41] Jeffery G. B., The motion of ellipsoidal particles immersed in a viscous fluid, Proc. R. Soc. Lond. A. 102 (1922) 161–179.

[42] Kaya T. and Koser H., Characterization of Hydrodynamic Surface Interactions of Escherichia coli Cell Bodies in Shear Flow, Phys. Rev. Lett. 1 (1982) 27–47.

[43] Keller S. and Skalak R., Motion of a tank-treading ellipsoidal particle in a shear flow, J. Fluid Mech. 103 (2009) 138103.

[44] Kessler S., Finken R. and Seifert U., Swinging and tumbling of elastic capsules in shear flow, J. Fluid Mech. 605 (2008) 207–226.

[45] Kwak S. and Pozrikidis C., Effect of the membrane bending stiffness on the axisymmetric deformation of capsules in uniaxial extensional flow, Phys. Fluids 13 (2001) 1234–1242.

[46] Lac E., Barthès-Biesel D., Pelekasis N. A. and Tsamopoulos J., Spherical capsules in three-dimensional unbounded Stokes flows; effect of the membrane constitutive law and onset of buckling, J. Fluid Mech. 516 (2004) 303–334.

[47] Lac E., Morel A. and Barthès-Biesel D., Hydrodynamic interaction between two identical capsules in simple shear flow, J. Fluid Mech. 573 (2007) 149–169.

[48] Le D. V., and Tan Z., Large deformation of liquid capsules enclosed by thin shells immersed in the fluid, J. Comput. Phys. 229 (2010) 4097–4116.

[49] Lefebvre Y., and Barthès-Biesel D., Motion of a capsule in a cylindrical tube: effect of membrane prestress, J. Fluid Mech. 589 (2007) 157–181.

[50] Levertt L. B., Hellums J. D., Alfrey C. P. and Lynch E. C., Red blood cell damage by shear stress, Biophys. J. 12 (1972) 257–273.

[51] Li J., Dao M., Lim C. T., and Suresh. S., Spectrin-level modeling of the cytoskeleton and optical tweezers stretching of the erythrocyte, Biophys. J. 88 (2005) 3707–3719.

[52] Li J., Lykotrafitis G., Dao M., and Suresh. S., Cytoskeletal dynamics of human erythrocyte, Proc. Natl. Acad. Sci. USA 104 (2007) 4937–4942.

[53] Li X. and Sarkar K., Front tracking simulation of deformation and buckling instability of a liquid capsule enclosed by an elastic membrane, J. Comput. Phys. 227 (2008) 4998–5018.

[54] Lima R., Ishikawa T., Imai Y., Takeda M., Wada S. and Yamaguchi T., Radial dispersion of red blood cells in blood flowing through glass capillaries: the role of hematocrit and geometry, J. Biomech. 41 (2008) 2188–2196.

[55] Liu F., Burgess J., Mizukami H., and Ostafin A., Sample preparation and imaging of erythrocyte cytoskeleton with the atomic force microscopy, Cell Biochem. Biophys. 38 (2003) 251–270.

[56] Liu S. C., Derick L. H., Agre P., and Palek J., Alteration of the erythrocyte-membrane skeletal ultrastructure in hereditary spherocytosis, hereditary elliptocytosis, hereditary pyropoikilocytosis, Blood 76 (1990) 198–205.

[57] Loewenberg M., and Hinch E. J., Collision of two deformable drops in shear flow, J. Fluid Mech. 338 (1997) 299–315.

[58] Lowenberg M., and Hinch E. J., Numerical simulation of a concentrated emulsion in shear flow, J. Fluid Mech. 321 (1996) 395–419.

[59] Matsumoto Y., Thesis for master's degree, Tohoku Unversity, 2010

[60] Marcelli G., Parker K. H., and Winlove C. P., Thermal Fluctuations of Red Blood Cell Membrane via a Constant-Area Particle-Dynamics Model, Biophys. J. 89 (2005) 2473–2480.

[61] Maryam S., Ishikawa T., Matsuki N., Abdekhodie M. J., Imai Y. and Yamaguchi T., Fluid particle diffusion through high-hematocrit blood flow within a capillary tube, J. Biomech. 44 (2011) 170–175.

[62] Mody N. A., Lomakin O., Doggett T. A. and Thomas G. , Mechanics of Transient Platelet Adhesion to von Willebrand Factor under Flow, Biophys. J. 88 (2005) 1432–1443.

[63] Igens-Mullol. J. and Schwartz D. K., Shear-induced molecular precession in a hexatic Langmuir monolayer, Nature 410 (2001) 348.

[64] Navot Y., Elastic Membranes in Viscous Shear Flow, Phys. Fluid 10 (1998) 1819–

1833.

[65] Noguchi H., Swinging and synchronized rotaions of red blood cells in simple shear flow, Phys. Rev. E 80 (2009) 021902.

[66] Pan T. W. and Wang T., Dynamical simulation of red blood cell rheology in microvessels, Int. J. Numer. Anal. Model 6 (2009) 455–473.

[67] Peng Z., Asaro R, J., and Zhu Q., Multiscale modeling of erythrocytes in Stokes flow, J. Fluid Mech. 686 (2011) 299–337.

[68] Pozrikidis C., Boundary Integral and Singularity Methods for Linearized Viscous Flow, Cambridge Univ. Press, 1992.

[69] Pozrikidis C., Modeling and simulation of capsules and biological cells, Chapman & Hall/CRC, 2003.

[70] Pozrikidis C., Numerical simulation of the flow-induced deformation of red blood cells, Ann. Biomed. Eng, 31 (2003) 1194–1205.

[71] Pozrikidis C., Resting shape and spontaneous membrane curvature of red blood cells, Math. Med. Biol., 22 (2005) 34–52.

[72] Pries A. R., Neuhaus D., and Gaehtgens P., Blood viscosity in tube flow: dependence on diameter and hematocrit, Am, J. Phsiol., Heart Circ. Physiol., 263 (1992) H1770–H1778.

[73] Ramanujan S. and Pozrikidis C., Deformation of liquid capsules enclosed by elastic membranes in simple shear flow; large deformations and the effect of fluid viscosities, J. Fluid Mech. 361 (1998) 117–143.

[74] Secomb T. W., Skalak R., A two-dimensional model for capillary flow of an asymmetric cell, Microvasc. Res. 24 (1982) 194–203.

[75] Secomb T. W., Interaction between bending and tension forces in bilayer membranes, Biophys. J. 54 (1988) 743–746.

[76] Schäfer A., Wiesmann F., Neubauer S., Eigenthaler M., Bauersachs J and Channon K. M., Rapid regulation of platelet activation in vivo by nitric oxide, Circulation 109 (2004) 1819–1822.

[77] Schenk O. and Gärtner K., Solving unsymmetric sparse systems of linear equations with PARDISO, Future Generation Computer Systems 20 (2004) 475–487.

[78] Skalak R., Tozeren A., Zarda R. P. and Chien S., Strain energy function of red

blood cell membranes, Biophys. J. 13 (1973) 245–264.

[79] Skotheim J. M. and Secomb T. W., Red blood cells and other nonspherical capsules in shear flow: oscillatory dynamics and the tank-treading-to-tumbling transition, Phys. Rev. Lett. 98 (2007) 078301.

[80] Sprague R. S., Ellsworth M. L., Stephenson A. H. and Lonigro A. J., ATP: the red blood cell link to NO and local control of the pulmonary circulation, Am. J. Physiol. 271 (1996) H2717–H2722.

[81] Sprague R. S., Ellsworth M. L., Stephenson A. H., Kleinhenz M. E. and Lonigro A. J., Deformation-induced ATP release from red blood cells requires CFTR activity, Am. J. Physiol. 275 (1998) H1726–H1732.

[82] Sui Y., Chew Y. T., Cheng Y. P. and Low H.T, Dynamic motion of red blood cells in simple shear flow, Phys. Fluids 20 (2008) 112106.

[83] Sui Y., Chew Y. T., Roy P. and Low H. T., A hybrid method to study flow-induced deformation of three-dimensional capsules, J. Comput. Phys. 227 (2008) 6351–6371.

[84] Tsubota K., Wada S. and Yamaguchi T., Simulation study on effects of hematocrit on blood flow properties using particle method, J. Biomech. Sci. Eng. 1 (2006) 159–170.

[85] Tsubota K., Wada S., Elastic force of red blood cell membrane during tank-treading motion: Consideration of the membrane's natural state, Int. J. Mech. Sci. 52 (2010) 356-364.

[86] Walter A., Rehage H., and Leonhard H., Shear induced deformation of microcapsules: shape oscillations and membrane folding, Colloids and Surfaces A 183-185 (2001) 123-132.

[87] Walter J., Salsac A.-V., Barthès-Biesel D. and Tallec P. L., Coupling of finite element and boundary integral methods for a capsule in a Stokes flow, Int. J. Numer. Meth. Engng. 83 (2010) 829-850.

[88] Walter J., Salsac A.-V. and Barthès-Biesel D., Ellipsoidal capsules in simple shear flow: prolate versus oblate initial shape, J. Fluid Mech. 676 (2011), 318-347.

[89] Wan J., Ristenpart W. D. and Stone H. A., Dynamics of shear-induced ATP release from red blood cells, Proc. Natl. Acad. Sci. U.S.A. 105 (2008) 16432–16437.

[90] Wang T., Pan T. W., Xing Z. W. and Glowinski R., Numerical simulation of rheology of red blood cell rouleaux in microchannels, Phys. Rev. E 79 (2009) 04196.

[91] Waugh R. and Evans E. A., Thermoelectricity of red blood cell membrane, Biophys. J. 26 (1979) 115–132.

[92] Wiggins P. and Phillips R., Membrane-Protein Interactions in Mechanosensitive Channels, Biophys. J. 88 (2005) 880–992.

[93] Yoshimura K., Usukura J. and Sokabe M., Gating-associated conformational changes in the mechanosensitive channel MscL, Proc. Natl. Acad. Sci. U.S.A. 105 (2008) 4033–4038.

[94] Yu Z., Phan-Thien N. and Tanner R. I., Rotation of a spheroid in a Couette flow at moderate Reynolds numbers, Phys. Rev. E 76 (2007) 026310.

[95] Zhao H., Isfahani A. H. G., Olson L. K., and Freund J. B., A spectral boundary integral method for flowing blood cells, J. Comput. Phys. 229 (2010) 3726–3744.

[96] Zhao H. and Shaqfeh E. S. G., Shear-induced platelet margination in a microchannel, Phys. Rev. E 83 (2011) 061924.

Publication lists

Refereed journals

1. Omori T., Ishikawa T., Barthès-Biesel D., Salsac A.-V., Walter J., Imai Y. and Yamaguchi T., Comparison between spring network models and continuum constitutive laws: Application to the large deformation of a capsule in shear flow, Phys. Rev. E 83 (2011) 041918.
2. Omori T., Ishikawa T., Imai Y. and Yamaguchi T., Reorientation of a non-spherical capsule in creeping shear flow, Phys. Rev. Lett. *under review.*
3. Omori T., Ishikawa T., Barthès-Biesel D., Salsac A.-V., Imai Y. and Yamaguchi T., Membrane tension on a red blood cell in simple shear flow, Ann. Biomed. Eng. *to be submitted.*

Book

1. Lima R., Nakamura M., Omori T., Ishikawa T. and Yamaguchi T., Microscale flow dynamics of red blood cells in microchannels: An experomental and numerical analysis, Springer, 2009.

International conferences

1. Omori T., Ishikawa T., Barthès-Biesel D., Salsac A.-V., Imai Y. and Yamaguchi T., Effect of membrane modeling on the capsule deformation: comparison between a spring network and continuum models, 6th World Congress of Biomechanics, 2010 Aug., Singapore, Book of abstract: page 470.
2. Omori T., Ishikawa T., Barthès-Biesel D., Salsac A.-V., Imai Y. and Yamaguchi

T., Impact of membrane modeling in analysing deformation of a capsule: comparison between a spring network model and constitutive laws, ECCM, 2010 May, France, Paris, Abstract CD-ROM.

3. Omori T., Ishikawa T., Barthès-Biesel D., Salsac A.-V., Imai Y. and Yamaguchi T., Impact of membrane modeling on the deformation analysis of a capsule, 3rd East-Asian Pacific Student Workshop on Nano-Biomedical Engineering, 2009 Dec., Singapore, Book of abstract: pp.122-123.
4. Omori T., Ishikawa T., Barthès-Biesel D., Imai Y. and Yamaguchi T., Effect of the memberane bending stiffeness on the deformation of a red blood cell, 4th Asian Pacific Conference on Biomechanics, 2009 Apr., University of Canterbury, New Zealand, Book of abstract: pp.196-197.
5. Omori T., Ishikawa T., Barthès-Biesel D., Imai Y. and Yamaguchi T., Modeling of the membrane bending rigidity for calculating red blood cell deformation, 15th International Conference on Finite Elements in Flow Problems, 2009 Apr., 中央大学, 東京, Book of abstract: page 41.
6. Omori T., Ishikawa T., Barthès-Biesel D., Imai Y. and Yamaguchi T., Behavior of a red blood cell in a simple shear flow simulated by a boundary element method, GPBE/NUS-Tohoku Graduate Student Conference in Bioengineering , 2008 Dec., Singapore, Book of abstract: 99-100.
7. Omori T., Ishikawa T., Barthès-Biesel D., Imai Y. and Yamaguchi T., Behavior of a red blood cell in a simple shear flow simulated by a boundary element method, Bioengineering 08, 2008 Sep., Imperial Colledge, London, Book of abstract: page 135.
8. Omori T., Wada S., Tsubota K. and Yamaguchi T., Multi-scale simulation of blood flow with the dynamical behavior of elastic red blood cells, 5th World Congress of Biomechanics, 2006 Aug., Germany, Munich, Journal of Biomechanics Vol.39, S649.

Domestic conferences

1. 大森俊宏, 石川拓司, Barthès-Biesel D., 今井陽介, 山口隆美, せん断流れ中の赤血球変形挙動の境界要素法解析, 第 21 回バイオエンジニアリング講演会, 2009 年 1 月, 札幌コンベンションセンター, 講演論文集: Vol. 8, No. 53, pp. 85-87.
2. 大森俊宏, 石川拓司, Barthès-Biesel D., 今井陽介, 山口隆美, 境界要素法による定ずり流れ中での赤血球の変形挙動解析, 第 19 回バイオフロンティア講演会, 2008 年 9 月, 首都大学東京, 講演論文集: Vol. 8, No. 30, pp. 47-48.
3. 大森俊宏, 和田成生, 坪田健一, 山口隆美, 2 次元赤血球流動モデルを用いた血流のマルチスケールシミュレーション, 第 11 回計算工学講演会, 2008 年 6 月, 大阪大学, 講演論文集: Vol. 11, No. 1, pp. 303-304.